DEVELOPMENT OF A PARTICLE SOURCE MODEL FOR A SYNERGY LINEAR ACCELERATOR TO BE USED IN MONTE CARLO RADIATION DOSE CALCULATIONS FOR CANCER THERAPY

BY

DÉTE VAN EEDEN

Thesis submitted in fulfilment of the requirements for the M.Med.Sc (Medical Physics) degree in the Faculty of Health Sciences, at the University of the Free State

May 2014

Study Leader: Dr. FCP du Plessis

TABLE OF CONTENTS

Glossary

CAX	central axis
CT	computed tomography
cm	centimeter
DNA	Deoxyribonucleic acid
dpi	dots per inch
dmax	depth of dose maximum
EGS	electron gamma shower
ECUT	electron energy cut-off
eff_{depth}	effective depth
FVA	fokus tot veld afstand
GHz	gigahertz
cGy	centigray
GeV	gigaelectronvolt
GUI	graphical user interface
ICRU	International Commission on Radiation Units and Measurements
IMRT	intensity-modulated radiation therapy
IDL	Interactive Data Language

ISF	inverse square factor
keV	kiloelectron volt
kg	kilogram
kV	kilovolt
kVp	peak kilovoltage
Lb	pound
MC	Monte Carlo
MeV	mega electron volts
MV	megavolt
MLC	multileaf collimator
MU	monitor unit
mm	millimeter
OF	output factor
PEGS	pre-processor code for electron gamma shower
PCUT	photon energy cut-off
PDD	percentage depth dose
PSD	phase-space data
PRESTA	parameter reduced electron-step transport algorithm
RGB	Red-Green-Blue

SLAC	Stanford Linear Accelerator Center
SSD	source-surface distance
TIFF	tagged Image file format
TMR	tissue maximum ratio
TPS	treatment planning system
UK	United Kingdom
VEF	virtual energy fluence
VMAT	volumetric modulated arc therapy

1. CHAPTER 1: INTRODUCTION

1.1 Cancer detection

According to a world leading medical journal, The Lancet, there will be a 78% increase in cancer cases by 2030 in South Africa alone. In the UK more than 1 in 3 people will develop some form of cancer during their lifetime. In 2010 one person died every four minutes in the UK, adding up to 430 people per day [1]. It is no wonder that cancer has a reputation as a deadly disease.

This malignant disease is caused by a group of cells that divides and grows uncontrollably and when spread throughout the body can cause damage to vital organs. Cancer can be treated with different modalities such as radiation therapy, surgery, chemotherapy or a combination of more than one. Treatment with radiation can be done using collimated high energy x-rays directed at the tumour volume. This kills cancer cells and causes shrinkage of the tumour. Exploratory surgery is performed to aid in the diagnosis of cancer. Tumour resection can be performed to remove the tumour or part of it to relieve the symptoms it causes. Chemotherapy is classified as a systemic treatment and the drugs travel throughout the body to reach cancer cells wherever they are.

A radiation oncologist specializes in the diagnosis and treatment of cancer [2]. Once a patient is diagnosed with cancer the location and extent of the disease must be determined with great care. Diagnosis can be confirmed with histopathological examinations of tissue samples and a recognised staging classification. Imaging modalities such as CT can be used to stage the tumour which is a description of the extent to which the cancer has spread. The following factors are taken into account during the staging process: The size of the tumour, the depth of penetration, the invasion of adjacent organs and if it has metastasized to any

lymph nodes or distant organs. The staging of the tumour will determine which treatment protocol to be followed. Radical treatment may be possible where the intention is to cure the patient from the malignant disease. For more advanced cancers, palliative treatment is used to alleviate cancer symptoms, such as pain.

1.2 Radiation Therapy Planning

Radiation therapy can be divided into two groups: brachytherapy and teletherapy. In brachytherapy the source of radiation is a radionuclide e.g. Iridium-192 that is transported into the target volume via a catheter, applicator or needles. These treatments can be classified as intracavitary, intraluminal or interstitial [3]. Teletherapy entails treating the patient over a distance with high energy x-rays or electrons emanating from radiation machines such as Co-60 units, orthovoltage units and linear accelerators [4].

Before treatment can start, the patient is scanned on a CT scanner to obtain an anatomical model represented as a set of transverse images. The images are then transferred to a treatment planning system (TPS) where contouring of the structure volumes and the tumour (target) radiation distribution are planned. Different volumes are determined for the treatment of the malignant disease as described in the ICRU Report 50 (1993). The planning target volume consists of the gross visible malignant growth, a margin that includes any sub-clinical malignant disease and an additional margin for set-up uncertainties. Structure volumes aid in the treatment planning process and can be used to compare treatment outcomes as described in the ICRU Reports 50 and 62. In general, radiation treatment usually consists of a configuration of beams from different angles and with different apertures. The aim of radiation therapy is to deliver a prescribed dose to the tumour volume and at the same time spare the surrounding normal tissue and organs at risk.

Daily treatment is given with a fraction of the prescribed dose until the total dose is reached. The dose is calculated on a treatment planning system (TPS) and then transferred to the linear accelerator where the patient is treated.

1.3 Dose calculation algorithms

Some dose calculation methods are explained by Adnesjö and Aspradakis [5] and include the requirements, formalisms and algorithms for photon beam dose modelling in external beam radiotherapy. There are several modern algorithms used for treatment planning e.g. dose kernel convolution and superposition. Kernels or dose spread arrays *(*Mackie *et al* [6]*)* can be convolved with the relative primary fluence interacting in a phantom to obtain 3D dose distributions. The convolution method is sometimes referred to as the superposition method when the kernels used in the convolution method are scaled to consider the density of the medium. This is useful when inhomogeneities are found in the medium in which the dose is calculated.

Monte Carlo simulations are still the most accurate method of dose calculation since it uses first principles and can accurately mimic particle interactions taking place in the exposed matter. With the recent development in computer power Monte Carlo methods is now implemented into clinical treatment planning systems such as Monaco, Hyperion and Peregrine [7-9].

1.4 Biological damage by ionizing radiation

When radiation interacts with matter, energy is transferred to the absorbing material. This can lead to ionisations and excitations of atoms in the material. These radiation interactions can lead to the production of free radicals which can alter the chemical composition of nearby cells that ultimately leads to biological damage. This is an indirect effect of radiation. DNA

consists of a well-known double helix structure that controls all the functions of the cell. It is thus the critical target for biological damage from ionizing radiation through direct and indirect effects [10].

Free radicals are chemically active and can cause cell death through ionizing radiation interactions leading to their formation. It can alter the cell cycle and may cause carcinogenic mutations. The radiation beam must therefore be conformed closely around the tumour to limit radiation effects to the surrounding normal tissue.

1.5 Proton and neutron therapy

Other particles such as neutrons and protons can also be used for cancer irradiation depending on the tumour type and location, but are much more expensive to produce. Protons are produced in cyclotrons and the well-known Bragg-peak results in favourable depth-dose properties [11].

Neutrons are produced when protons hit a suitable target (lithium) and are used for irradiation of salivary gland tumours as well as cancer of the bones, joints, soft tissues (sarcomas), radio-resistant tumours (melanomas), renal cell and thyroid cancers. It is used when surgery is not an option for tumour resection.

1.6 Linear accelerators

Until the 1950's, most of the radiation therapy was carried out with kilovoltage units in the range of 300 kVp. Co-60 gained popularity in the 1950's and 1960's for high energy treatments. The development of medical linear accelerators soon followed and is the most widely used to date for modern radiation therapy [4]. In a linear accelerator the electron gun injects electrons into the waveguide where they are accelerated to high energies by high-frequency micro waves. These electrons are focused by the bending magnets and will then

strike a transmission bremsstrahlung target and produce high energy x-rays that are collimated and used for deep-seated tumour irradiation. Electrons alone can be used for the treatment of superficial lesions to spare distal organs at risk.

Dose distribution characteristics of radiation beams can be acquired with water tank scans. These scans provide useful information regarding the fluence distribution and energy spectrum of the radiation beam. This information can then be used to construct source models used in Monte Carlo simulations or in more complex analytical dose calculation algorithms.

1.7 Source models for Monte Carlo

One of the difficulties with the clinical implementation of Monte Carlo (MC) dose calculation is the characterization of the radiation source within a universal source model. Several approaches have been made by various authors in previous publications [12-14].

One of the approaches by Jiang *et al* [15] is to characterize the beam analytically by using conventional measured data. A more recent approach is a virtual energy fluence (VEF) model based on measured dose distributions as described by Fippel *et al* [16]. This model characterizes components inside the treatment head such as the target, primary collimator and flattening filter and is a measurement-driven approach. Probably the most common method is to perform full MC simulations of the radiation transport through the treatment head, generating phase-space data (PSD) [14, 17-21].

The source model that is investigated in this study is a photon point source. Beam particle fluence is modelled using suitable equations. The source is developed with the aid of an in-house code with a graphical user interface (GUI) that allows for fluence adjustments in order to replicate clinical beam data. It will be discussed in detail later in the dissertation.

1.8 What makes MC dose calculations so attractive?

The EGS (Electron Gamma Shower) code system was introduced in 1978 and was referred to as EGS3 as described by the SLAC-210 documentation. A new enhanced version (EGS4) has been developed by the Stanford Linear Accelerator Center (SLAC) which introduced an extension on the lower-energy limits for particle transport. In 2000 a new EGS4 version called EGSnrc was introduced with some significant changes that solved problems encountered in EGS4 [22]. The EGSnrc code can accurately calculate dose by simulating the transport of particles through any kind of material.

The MC simulation method is based on using random numbers to solve mathematical problems that will not be possible otherwise. This method is known to be most accurate to describe energy deposition since it is a realistic reflection of the physical processes involved. It can be used to simulate a linear accelerator and all radiation interaction events taking place inside the treatment head.

If we have an accurate source model representation of the head, then particles are "created" by the source and can then be transported according to MC methods that will be discussed in the next chapter.

A source model of our linear accelerator can make it possible to calculate and verify complex treatment modalities in the future such as intensity modulated radiation therapy (IMRT) and volumetric modulated arc therapy (VMAT) [23]. The uses of these techniques are increasing and the amount of quality assurance associated with it is substantial. This study will focus on static fields for forward and conformal therapies only

1.9 Aim

The aim of this study is to develop a particle source model for an Elekta Synergy linear accelerator of 6 MV and to verify its accuracy for radiation dose calculations with film and

ionization chamber measurements using suitable phantoms. The validity of the source model data will be determined by comparing it with benchmarked water tank data and a passing criterion of 2% / 2 mm.

1.10 Bibliography

1. UK CR. All cancers combined Key Facts [Internet]. 2014 [cited 2014 Mar 24]. Available from: http://www.cancerresearchuk.org/cancerinfo/cancerstats/keyfacts/Allcancerscombined/

2. Kutcher GJ, Coia L, Gillin M, Hanson WF, Leibel S, Morton RJ, et al. Comprehensive QA for radiation oncology: Report of AAPM Radiation Therapy Committee Task Group 40. Med Phys. 1994 Apr 1;21(4):581–618.

3. Adeel A. Handbook of Radiotherapy Physics - Theory and Practice - Taylor & Francis (2007) [Internet]. [cited 2014 Apr 29]. Available from: http://www.academia.edu/2430074/Handbook_of_Radiotherapy_Physics_-_Theory_and_Practice_-_Taylor_and_Francis_2007_

4. Podgorsak EB. Radiation Oncology Physics: A Handbook for Teachers and Students. Vienna, Austria: International Atomic Energy Agency; 2005. p. 657.

5. Ahnesjö A, Aspradakis MM. Dose calculations for external photon beams in radiotherapy. Phys Med Biol. 1999 Nov 1;44(11):R99–R155.

6. Mackie TR, Scrimger JW, Battista JJ. A convolution method of calculating dose for 15-MV x rays. Med Phys. 1985 Mar 1;12(2):188–96.

7. Boudreau C, Heath E, Seuntjens J, Ballivy O, Parker W. IMRT head and neck treatment planning with a commercially available Monte Carlo based planning system. Phys Med Biol. 2005 Mar 7;50(5):879.

8. Li J, Doemer A, Cao J, Podder T, Harrison A, Yu Y, et al. SU-FF-T-125: Commissioning of Monaco Monte Carlo IMRT Treatment Planning System. Med Phys. 2009 Jul 9;36(6):2548–2548.

9. Chetty IJ, Curran B, Cygler JE, DeMarco JJ, Ezzell G, Faddegon BA, et al. Report of the AAPM Task Group No. 105: Issues associated with clinical implementation of Monte Carlo-based photon and electron external beam treatment planning. Med Phys. 2007 Nov 27;34(12):4818–53.

10. Hall EJ. RADIOBIOLOGY FOR THE RADIOLOGIST. Fifth edition. Columbia University, New York: Lippincott Williams & Wilkins; 2000.

11. Paganetti H. Proton Therapy Physics (Series in Medical Physics and Biomedical Engineering). 1st ed. CRC Press, Taylor & Francis Group; 2011.

12. Verhaegen F, Seuntjens J. Monte Carlo modelling of external radiotherapy photon beams. Phys Med Biol. 2003 Nov 7;48(21):R107–R164.

13. Fix MK, Keall PJ, Dawson K, Siebers JV. Monte Carlo source model for photon beam radiotherapy: photon source characteristics. Med Phys. 2004;31(11):3106–21.

14. Ma CM, Faddegon BA, Rogers DWO, Mackie TR. Accurate characterization of Monte Carlo calculated electron beams for radiotherapy. Med Phys. 1997 Mar 1;24(3):401–16.

15. Jiang SB, Boyer AL, Ma C-MC. Modeling the extrafocal radiation and monitor chamber backscatter for photon beam dose calculation. Med Phys. 2001 Jan 1;28(1):55–66.

16. Fippel M, Haryanto F, Dohm O, Nusslin F, Kriesen S. A virtual photon energy fluence model for Monte Carlo dose calculation. Med Phys. 2003;30(3):301–11.

17. DeMarco JJ, Solberg TD, Smathers JB. A CT-based Monte Carlo simulation tool for dosimetry planning and analysis. Med Phys. 1998 Jan 1;25(1):1–11.

18. Lawrence Livemore National Laboratory's PEREGRINE Project. Proc 12th Int Conf on the Use of Computers in Radiation Therapy. Salt Lake City, UT: Medical Physics Publishing, Madison, Wisconsin; p. 19–22.

19. Kuster G, Bortfield T, Schlegel W. Monte Carlo simulations of radiation beams from radiotherapy units and beam limitimg devices using the program GEANT. Proc 12th ICCR Salt Lake City USA. 1997;

20. Lovelock DMJ, Chui CS, Mohan R. A Monte Carlo model of photon beams used in radiation therapy. Med Phys. 1995 Sep 1;22(9):1387–94.

21. Mohan R, Chui C, Lidofsky L. Energy and angular distributions of photons from medical linear accelerators. Med Phys. 1985 Sep 1;12(5):592–7.

22. Bielajew AF, Hirayama H, Nelson WR, Rogers DWO. History, overview and recent improvemnets of EGS4. 1994 Jun. Report No.: SLAC-PUB-6499.

23. Otto K. Volumetric modulated arc therapy: IMRT in a single gantry arc. Med Phys. 2007 Dec 26;35(1):310–7.

2. CHAPTER 2: THEORY

2.1 Introduction

The Monte Carlo method uses random numbers for statistical simulations of natural stochastic occurrences. By simulating microscopic interactions, it can find a solution to a macroscopic system [1].

The idea to use Monte Carlo methods for stochastic sampling was first introduced by Ulam [2] while playing solitaire. This method later found its way into the detrimental world when used by Ulam and von Neumann for their work related to thermonuclear weapons. In 1947 the Monte Carlo method was suggested for radiation transport calculations [3, 4] and the study of shower production followed soon in 1952 by Wilson [5]. The first paper where "Monte Carlo" was associated with stochastic sampling was published in 1949 by Ulam and Metropolis [6]. The Monte Carlo method was named after the capital city of Monaco, famous for its casinos and gambling.

There is a great amount of reviews on the use of Monte Carlo in the field of medical physics, especially radiotherapy and dosimetry [7-12]. The Monte Carlo method for radiation transport was used in linear accelerator modelling as soon as 1983 and is still used today by various authors [13-16].

2.1.1 Accuracy of Monte Carlo simulations

From benchmarking studies it is evident that Monte Carlo is the most accurate dose calculation code that meets the accuracy demand of radiotherapy. It is no wonder that is it considered to be the golden standard for dose calculations.

This method is very realistic and is applied to simulate dose deposition through the transport of particles [8, 11, 16-21]. The demand for accurate dose calculations has increased dramatically with modern treatment techniques such as intensity-modulated radiation therapy (IMRT) [22]. The accuracy of Monte Carlo is demonstrated even further when used for the modelling of Gamma Knife and Stereotactic units which enquires a high degree of precision [23-32].

Volumetric Arc Therapy (VMAT) was proposed by Otto [33] in 2008 to decrease the treatment time produced by IMRT and to improve the efficiency of treatments. Monte Carlo dose calculations have been shown to be accurate for VMAT and are utilized in the Monaco® treatment planning system.

Monte Carlo holds the ability to accurately simulate radiation dose in tissue inhomogeneities, such as the lung, and irregular surfaces [34-36]. With the development of innovative new techniques and more powerful computers, Monte Carlo can now be used for clinical treatment planning [37,38].

2.1.2 The Monte Carlo method for radiation beam transport modelling

Several interactions occur as high energy photons and electrons are passing through matter. Electrons can be slowed down which results in the creation of bremsstrahlung photons or can set secondary electrons free. Photons can produce positron-electron pairs and also set secondary electrons free. Due to the complexity of charged particle interactions it is difficult to model their transport in detail although the physics are well known. The way to solve this problem will be discussed in the following sections.

2.2 Photon Interactions

As a photon passes through matter it can undergo various interactions e.g. photoelectric absorption, Compton scatter, pair production and triplet production. It will produce secondary particles such as electrons or scattered photons. These secondary electrons will deposit their energy in the vicinity of the interaction site whereas scattered photons may travel a distance before interacting.

2.2.1 Photoelectric absorption

In a photoelectric absorption event the photon passes through matter and interacts with a nearby atom. This process occurs if the energy of the photon is equal or not much greater that the ionisation energy of the atoms in the medium. The photon transfers all of its energy to the atomic electron and no longer exists. The photoelectron is then ejected from the atom leaving a vacancy in one of the shells [39]. An electron from a higher energy level (shell) will then fill this vacancy and emits characteristic radiation. The photoelectron will continue onwards through the medium, interacting with other atoms until all its energy is exhausted and a nearby atom captures it [40].

2.2.2 Compton scattering

Compton scatter takes place between an incoming photon and a free electron. The electron recoils from the collision and is ejected from the atom. This Compton recoil electron will once again continue its path through the medium, interacting with other atoms, until it comes to rest. The photon lost some of its energy to the electron and will continue with a change of direction and reduced energy [41].

2.2.3 Pair and triplet production

This absorption can occur when the incoming photon energy is more than the 1.02 MeV energy threshold required for pair production. As the photon travels through the medium and moves close to the nucleus of an atom it experiences strong electric forces (Figure 2-1 a). These forces are the result of the positive charge of the protons inside the nucleus. The photon undergoes a transformation into a positron and electron pair converting some of the photon energy into mass ($2M_eC^2$). The remaining energy is shared as kinetic energy between the pair.

Photon transformation can also occur in the electric field of an atomic electron instead of the nucleus (Figure 2-1 b). The atomic electron is also ejected from the atomic shell. The result of this interaction is two electrons and a positron, hence the name triplet production. The threshold energy for triplet production is 2.04 MeV [42]. Triplet production gets increasingly less important than pair production with increasing atomic number.

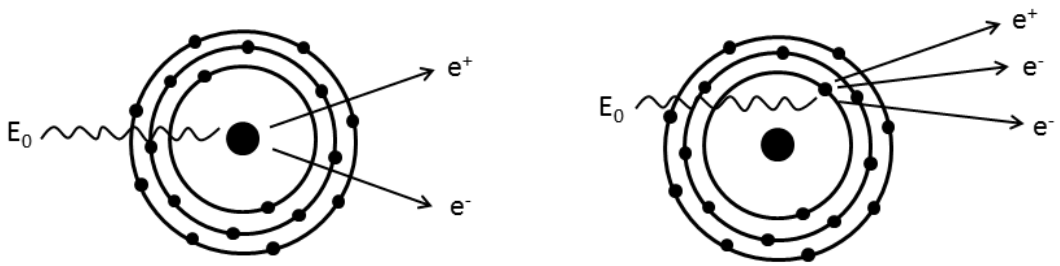

a b

Figure 2-1: a) Pair production where the incoming photon experiences strong forces from the nucleus. b) Triplet production where the incoming photon interacts with the electric field of an atomic electron.

2.3 The relative importance of photon interactions

Photoelectric absorption depends strongly on atomic number and is the main interaction process for photons at low energies e.g. that used in diagnostic radiology. The atomic

number dependence for photoelectric events causes soft tissue (Z = 7) to transmit a greater fraction of the beam compared to bone (Z =14). For a CT scan with mean energy of 60 keV the photoelectric effect will therefore be more pronounced in bone than in soft tissue leading to desirable contrast between the two materials. Photoelectric absorption is unlikely to occur at photon energies above 100-200 keV in water but can occur for photon energies of up to 1 MeV for lead [43].

When it comes to radiation therapy, Compton scatter is the main process for photon-tissue interactions. Compton scatter is independent of atomic number and more dependent on the electron density of the material. In tissue, pair production dominates at energies higher than 25 MeV and can occur at high energy photon beam treatments [44].

As seen in Figure 2-2, Compton scatter and pair production will dominant at higher energies used in radiation therapy. The contrast between soft tissue and bone will be less pronounced in the megavoltage range compared to the contrast in kV imaging where photoelectric absorption dominants. Therefore the use of kV imaging for patient positioning at linear accelerators is becoming more pronounced.

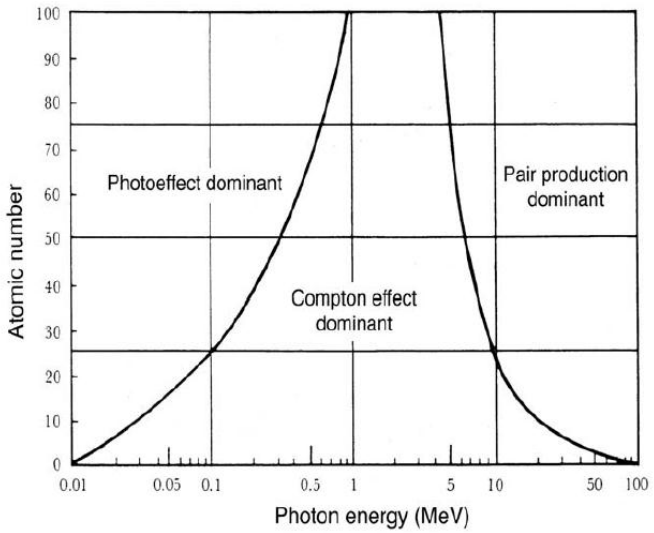

Figure 2-2: The domination of the different interactions as a function of atomic number and photon energy (MeV) [45].

2.4 Electron transport

As a fast electron passes through matter and it slows down it undergoes hundreds and thousands of interactions along the way. This nature of electron interactions causes difficulty to incorporate it into Monte Carlo simulations. It is possible to sample some of the sparser interactions like large energy-loss events with large scattering angles as well as hard bremsstrahlung emission and positron annihilation.

Low-energy Möller scattering and atomic excitations are considered to be soft collisions and to do event-by-event simulations will need long computing times that is not always possible or practical. This problem was overcome in 1963 with the development of the condensed history technique by Berger [46].

This technique consists of compressing large numbers of electron interactions into one single step. It is like taking snapshots of the electron as it passes through matter. The total effect of all the interactions is taken into account to determine the charged particle's energy and direction at the end of the step. This approach is possible since single soft collisions only result in small changes in energy and direction [47]. When simulating electron transport, it is assumed that they lose energy in a continuous way and not discrete like photons do. These electrons will continue to lose energy until they reach a user defined energy cut-off value, ECUT. In order to properly account for electron energy deposition within a voxel, appropriate boundary crossing algorithms must be developed and used.

The PRESTA-I boundary crossing algorithm is the default algorithm used in EGSnrc. The shortcomings of PRESTA-I does not have a significant effect on most radiation transport dose calculations and is considered to be efficient. Dose over prediction of 2.5% can occur when lateral electron equilibrium does not exist or when the voxel sizes are not uniform throughout the phantom [48].

Another electron-step algorithm used in the EGS-system is PRESTA-II and is used for the transport of electrons through a medium and takes lateral and longitudinal correlations into account in a condensed history step.

2.5 PEGS4

The EGSnrc MC Code System can simulate radiation transport of electrons and photons in any mixture, compound or element. The pre-processor code for EGSnrc, PEGS4, calculates cross section data using similar data for elements 1 to 100. PEGS4 needs input for the creation of this data that includes the selection of materials and energy cut-offs and subsequently the output of data that can be used by EGS [49].

Other important quantities calculated by PEGS4 include the collision stopping power for electrons and positrons. As an electron passes through a medium it undergoes inelastic energy losses. The density of the medium is taken into account by the total mass-energy stopping power and describes the kinetic energy lost per unit path length [45].

2.6 Random numbers

Monte Carlo relies on the use of good sets of random numbers and is produced by pseudo-random number generators. It can be considered the 'heart beat' of Monte Carlo [50-52]. Through the generation of these random numbers and proper sampling from probability density functions, the true stochastic nature of particle transport can be imitated.

There are different means of producing 'true' random numbers e.g. connecting a piece of hardware like an electric motor that stops at random positions, to a computer, or by storing large arrays of random numbers that can be used. The reason for using pseudorandom numbers is the repeatability, which is essential for code debugging as stated by Bielajew [53].

The ideal pseudorandom number generator produces numbers that repeat over a large period. This string of numbers can change if the initial value is changed [54].

The linear congruential random number generator was proposed by D.H. Lehmer in 1949 [55] and is one of the most regularly applied random number generators. The n-th random number is found through

$$S_n = (a * S_n - 1 + c) \bmod 2^k \tag{2-1}$$

Where *a* is the multiplier, the integer *c* the increment, and the integer *k* is the integer word size of the computer. Monte Carlo simulations use the multiplicative linear congruential random number generator where the value of c is equal to zero [56].

The first number of the sequence (S_0) is known as the seed [57]. The EGSnrc code uses the RANLUX generator that produces sequences that are independent from one another and is ideal for doing parallel runs on multiple computers or for dividing histories between multiple cores on a computer [58].

2.7 Random sampling

The essence of a probability distribution function *P(x)* is the likelihood for this random variable to take on a given value. Random numbers are used to sample from probability distributions. These samplings include the distance travelled before an interaction takes place, the type of interaction taking place and the energy and direction of the secondary particles. These functions contain cross section coefficients generated by PEGS4 in the EGS based MC code system.

A few sampling methods will be discussed followed by a practical example.

2.7.1 The inversion method

An illustration of this method is given in Figure 2-3.

Suppose we have a probability distribution function of the variable *x*

$$\int_{-\infty}^{+\infty} f(x)dx = 1 \tag{2-2}$$

The cumulative distribution function will then be

$$F(x) = \int_{-\infty}^{x} f(y)dy \tag{2-3}$$

This function gives the probability of having a value less than *x*.

If *r* is a random number between 0 and 1, the corresponding *x* value (x_{corr}) can be calculated by using *F(x).*

$$x_{corr} = F^{-1}(r) \tag{2-4}$$

To use this sampling method *F(x)* must be invertible.

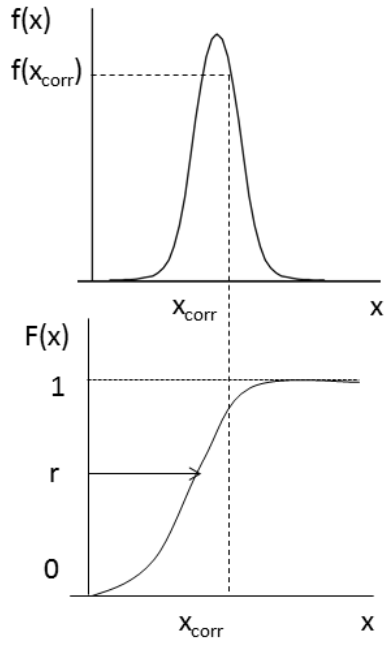

Figure 2-3: The probability distribution function (top) and the cumulative distribution function (bottom).

2.7.2 Rejection method

The rejection method is not as efficient as other methods e.g. alias sampling and the inversion method, but it works in more cases where simple inversion is not possible [53].

Suppose we have a probability distribution function of the variable *x* called *f(x)*. Figure 2-4 shows this function scaled to its maximum value.

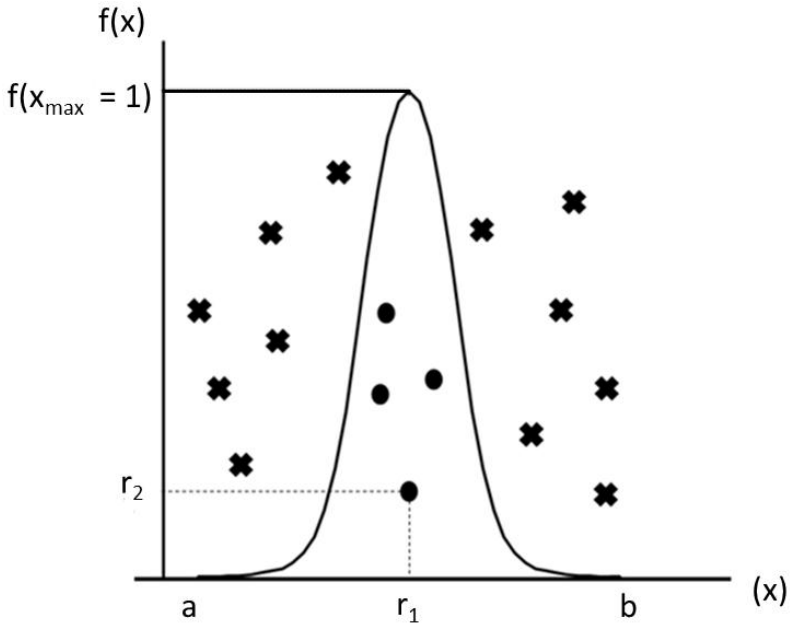

Figure 2-4: The normalized probability distribution function of the variable *x*.

A uniform position distribution inside the probability distribution function, *x*, can be sampled by using the random numbers r_1 and the following equation:

$$X = a + (r_1(b-a)) \tag{2-5}$$

Here *a*, and *b* is the definition interval of *f(x)*. If *f(x)* < a or *f(x)* > b, then *f(x)* = 0.

A second random number r_2 is then generated. If $r_2 \leq f(x_{max})$, then *x* is accepted as indicated by the dots in Figure 2-4. If r_2 falls outside of the specified region, *x* is rejected as indicated by the crosses.

It is evident that the efficiency of the sampling is quite poor and can be improved by using an alias sampling discretizing method. Sometimes *f(x)* is very complicated, and then mixed sampling methods are employed. In this method,

$$F(x) = g(x)h(x) \tag{2-6}$$

g(x) and *h(x)* can be sampled from rejection or inversion methods.

2.7.3 Alias sampling

This method was originally proposed by A.J. Walker in 1977 to sample from a one dimensional distribution [59]. This sampling method is described in detail by Keith Schwartz in his article Darts, Dice and Coins [60].

Suppose you want to sample from the following discrete distribution of, say, an energy spectrum as in Figure 2-5.

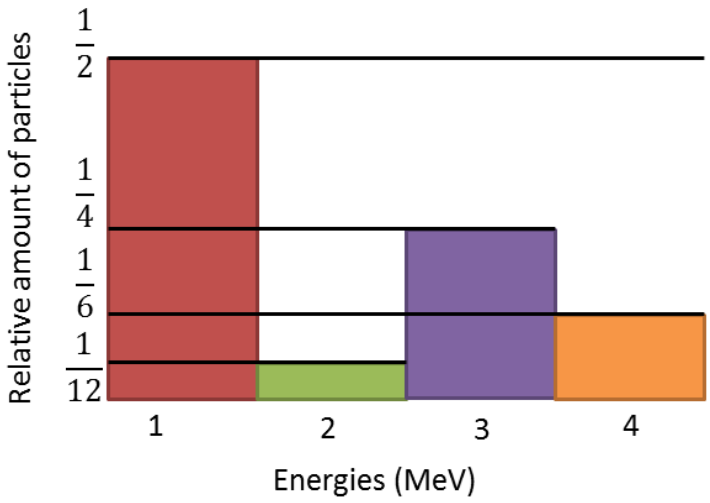

Figure 2-5: The spectrum and the total amount of particles in each energy bin.

To sample from this histogram we need to convert it into a form as shown in Figure 2-6. A random number can be drawn from 0 and 1 to find the corresponding energy bin. A

second random number is drawn to find out how high the point lies in each bin. The location of the point would then determine the energy value in the bin. This is shown in Figure 2-6.

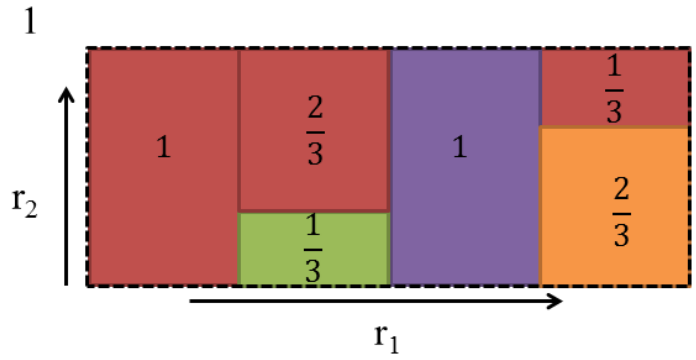

Figure 2-6: The redistribution of Figure 2-5. With the alias sampling method we now have a 100% sampling efficiency.

Note that we will have a result for every (r_1, r_2) pair sampled that is much more efficient than a sampling method such as rejection sampling.

2.8 Practical example of the simulation of photon transport

As photons travel through a material there exists a probability that they can interact with the medium. The probability that such an interaction will occur at a distance x is given by the total linear attenuation coefficient (μ). This coefficient gives an indication of how a medium can absorb photons. Lead has a large coefficient and easily attenuates a photon beam that passes through it. A small attenuation coefficient is an indication that the medium is nearly transparent to the beam and the probability of an interaction occurring per unit path length is small. The first step in the simulation will be to determine the distance to the next interaction site by the use of sampling from a suitable probability density function.

2.8.1 Distances between interactions

The mean free path length of a photon with a specific energy is defined as the average distance travelled between interactions. The mean free path length and the linear attenuation coefficient have the relationship $\lambda = \frac{1}{\mu}$ and the probability density function for interactions can be written as:

$$f(x) = \mu e^{(-\mu x)} \tag{2-7}$$

where μ is the total linear attenuation coefficient and x the distance to the interaction point.

The distance to the next interaction is obtained by the cumulative function:

$$F(x) = 1 - e^{(-\mu x)} \tag{2-8}$$

The probability of an interaction occurring increases as the particle travels a larger distance e.g. more than one mean free path. If a random number, r is chosen over a unit interval the distance to the next interaction, x is given by:

$$x = -\frac{1}{\mu}\ln(1-r) = -\frac{1}{\mu}\ln(r) \tag{2-9}$$

Next the type of interaction is selected through the use of branching ratios of interaction cross section coefficients at the current photon energy.

2.8.2 Type of interaction

The type of interaction that occurs is based on choosing a random number over the interval [0,1]. The photon will lose energy depending on the type of interaction and may be scattered to a new interaction site. This will continue until the photon energy is below the pre-set cut-off energy or it has left the material. Such a process forms part of a so-called history [58]. If all

interactions and all secondary particles are followed until they reach an energy cut-off level or has left the medium, then one history is completed.

Let us assume that there are three different types of interactions that can occur as a photon passes through a medium namely photoelectric effect, Compton scatter and pair production. The three interactions each have a cross section for occurrence. On deriving their partial fractions, and packing them into the schematic shown in Figure 2-7, allows us to choose an interaction based on the branching ratio.

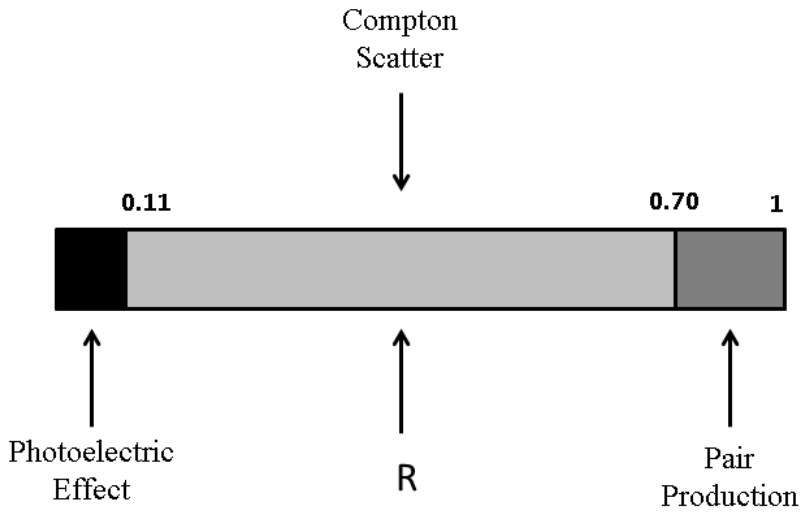

Figure 2-7: The selection of the type of interaction that will occur according to a random number *R*.

In the above example we see that Compton scatter makes up 59% of the interactions and shall be sampled 59% of the time to determine the interaction type. This branching ratio will change for a different photon energy and medium.

2.8.3 Determination of energy and direction of new particles

If the photon undergoes a Compton interaction it will result in a scattered photon and electron with a new energy and direction as shown in Figure 2-8.

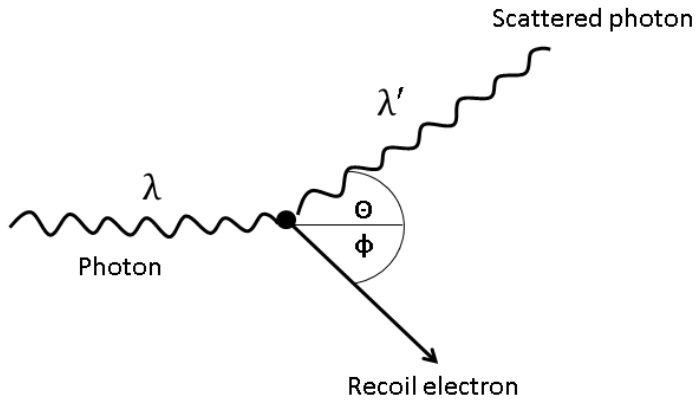

Figure 2-8: The scattered photon and recoil electron resulting from the Compton interaction.

The differential cross-section per unit solid angle for Compton scattering is given by the Klein-Nishina formula from 1929 [61].

The dynamic variables (phase space parameters) needed for simulation is held inside an array called STACK. The parameters of the initial photon are place on top of this stack and can be used in the photon transport process. As seen in Figure 2-9, a logical process is followed for the transport of photons.

The initial photon is placed on stack with a certain energy, position, direction and weight. If the photon energy falls below the user defined cut-off energy then the transport of the photon is terminated at once. This is representative of low energy photons that are completely absorbed by photoelectric absorption.

If the energy of the photon is above the user defined cut-off energy then the distance to the next interaction is sampled. If the photon has left the volume of interest then its transport is terminated and the next particle on stack is used. Otherwise the interaction type is sampled and the resultant particles' energies and directions are stored on stack for future processing. If the stack is empty during the transport process, a history is then completed and a new initial photon's parameters are placed on stack.

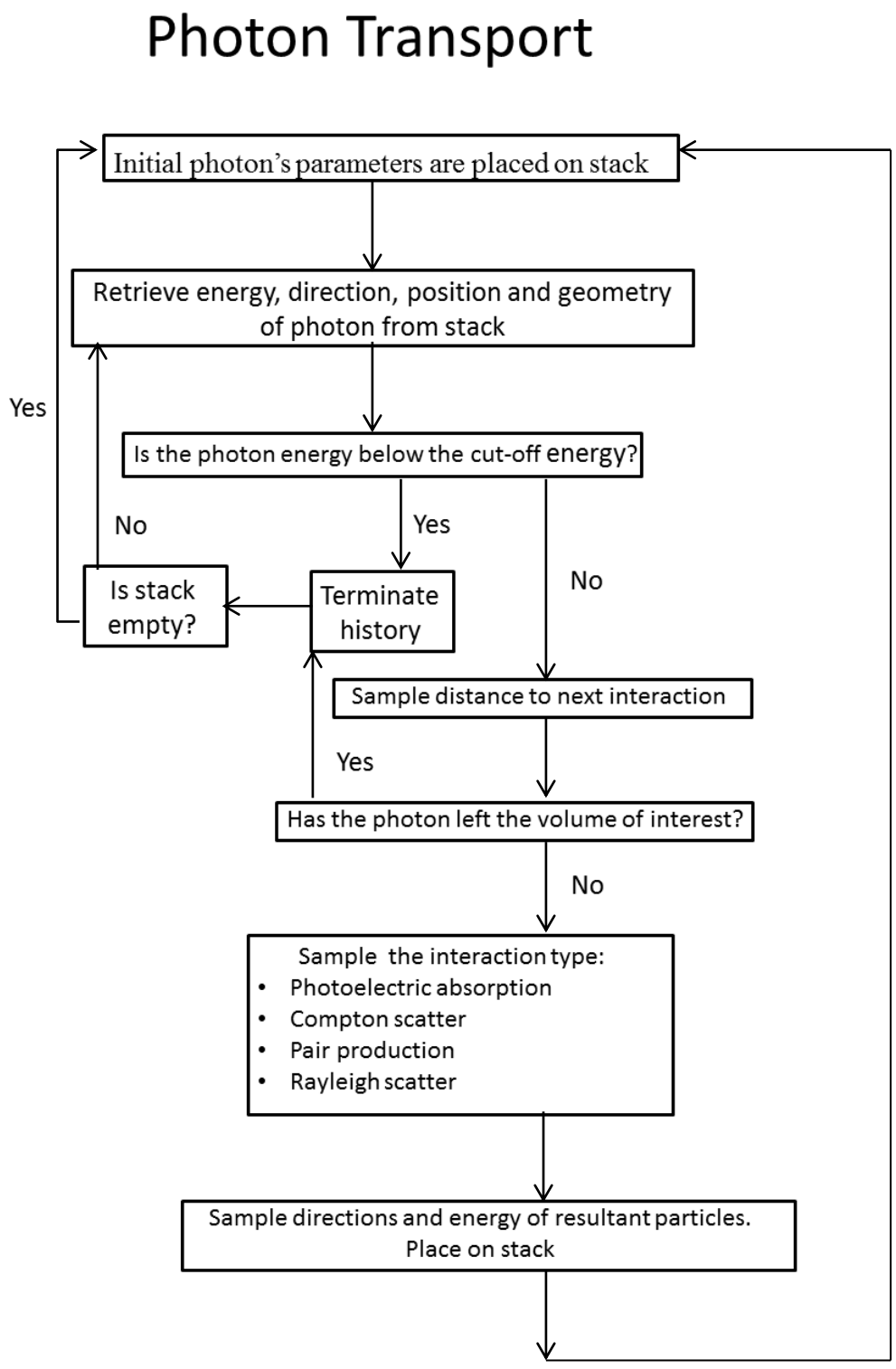

Figure 2-9: The photon transport process [62].

2.9 Monte Carlo codes used in this study

The use of Monte Carlo simulations in the field of medical physics started in 1970-1980. Nowadays there are several MC codes available for the simulation of photon transport in radiotherapy. The code used in this study are the EGSnrc based DOSXYZnrc code. There is no need for BEAMnrc since we are using a beam characterisation model and not a phase space file resulted from a full linear accelerator simulation.

Many particles are transported one by one to ensure that variance of the stochastic processes is reduced to meaningful levels. If the number of histories is large enough the information about the transport process can be obtained by averaging over the histories. A Monte Carlo simulation will always have a certain degree of inherent uncertainty due to its random nature and to eliminate it will take an unrealistic amount of histories that is not practically possible [63]. The statistical uncertainty can be reduced by increasing the amount of histories. Computation time can be reduced by using variance reduction methods.

2.10 Variance reduction techniques

To reduce the amount of variance in a simulation, the amount of samples has to increase which in turn prolongs the computational time. In general, simulations will take four times longer if the variance must be reduced by 50%. This problem can be overcome by using variance reduction techniques to do simulations more efficiently [64].

These techniques can introduce errors if used incorrectly as some approximations have to be made to quantities used in the transport. It is sometimes possible to achieve an acceptable level of uncertainty, in a reasonable amount of time, without the use of variance reduction techniques.

Some of the electron- and photon-specific reduction techniques used will be discussed briefly.

2.10.1 Interaction forcing

This technique is useful when photons have a slight chance of undergoing an interaction. This can be due to the photon leaving the volume before an interaction can occur. This wastes computing time since the photon is tracked through the geometry and in the end it doesn't result in an interaction. The interaction forcing technique forces the photon to interact by reducing the mean free path λ as in Figure 2-10 [65]. It is used to produce scattered photons or in the case of electrons it can force the formation of bremsstrahlung photons.

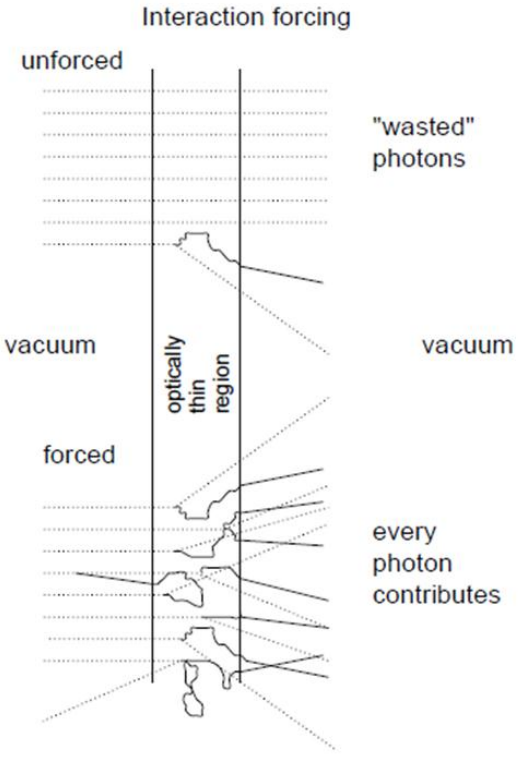

Figure 2-10: Photon interaction forcing [53]

2.10.2 Particle splitting

Particle splitting entails the splitting of photons into *N* sub-photons each with a weight $\omega' = \frac{\varpi}{N}$ where the weight of the sub-photons is ω' and ϖ is the initial weight of the photon. Figure 2-11 below shows an electron hitting the target (left) and producing a bremsstrahlung photon. When using particle splitting the bremsstrahlung photon will be split into *N* number of sub-photons, in this case 5 (right).

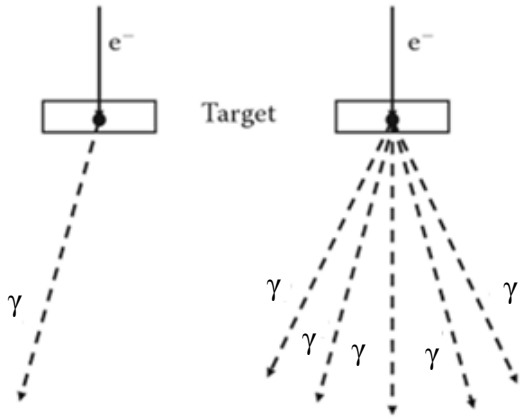

Figure 2-11: An illustration of particle splitting where an electron hits a target and produces bremsstrahlung photons. Left) Without particle splitting. Right) With particle splitting [45].

The time necessary to create five photons is saved by only creating one photon and then splitting it into 5 sub-photons.

2.10.3 Russian roulette

In Russian roulette a random number is chosen and if it is above a certain threshold value, the particle is terminated. If the random number is below a certain threshold value, the particle can continue with its path.

Particle splitting and Russian roulette techniques can be used separately or together. They are useful when calculating the dose in deep regions or far from the beam axis.

2.10.4 Range rejection

This method is used for charged particles where the energy determines the maximum range of the particle. The shortest distance from the electron's position to the boundary of the region is calculated and compared to that of the maximum range. If it is concluded that the electron will never leave the boundary then the transport of the particle is stopped. This technique is applicable when an electron has to reach a certain region or sensitive volume by going through other boundaries e.g. an ionisation chamber [64].

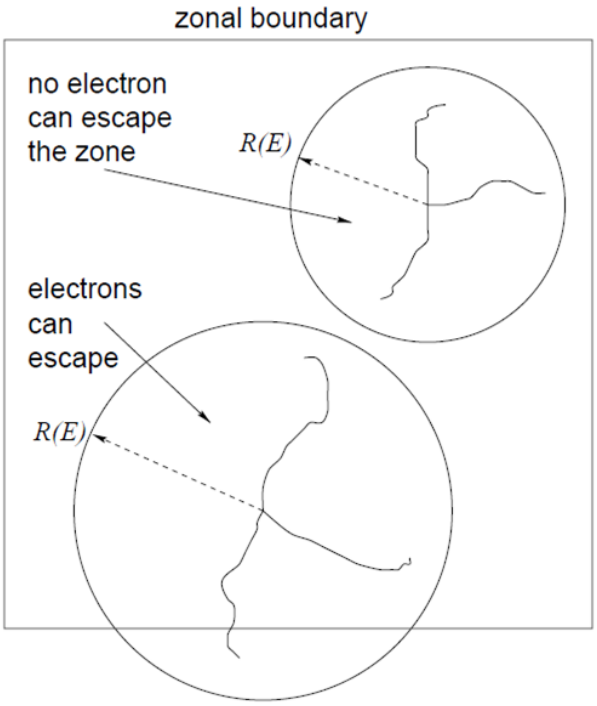

Figure 2-12: Range rejection technique used with charged particles [53].

2.11 EGSnrc

As stated by Kawrakow *et al* [58], EGSnrc is the child of many parents that made contributions to the code's development. It can simulate the transport of electron or photons in any element, compound or mixture. The PEGS4 data package (as discussed earlier)

consists of the cross section tables for elements 1 through 100 that are used by the EGSnrc code. The particles are transported in steps of random length and the kinetic energies ranges from a few tens of keV up to a few hundred GeV. Bremsstrahlung production, positron annihilation and multiple scattering are some of the physics processes that are taken into account by this code.

2.12 DOSXYZnrc

DOSXYZnrc is an EGSnrc-based Monte Carlo code and is used to determine the dose distribution in a user defined 3-dimensional phantom. The phantom consists of voxels with varying sizes, densities and materials that can be altered as required. It simulates the transport of photons and electrons in the Cartesian volume and scores the dose in each voxel.

There is a variety of beam sources that can be directed from different angles that is used in DOSXYZnrc. In this study the beam characterization model (Isource=4) is used that is incident from any direction. A polar coordinate system is set up at the isocenter with a distance, *dsource,* to the center of the source plane. The position of the origin of the plane is defined by *theta* and *phi* and the rotation of the source around its own plane is described by *phicol*.

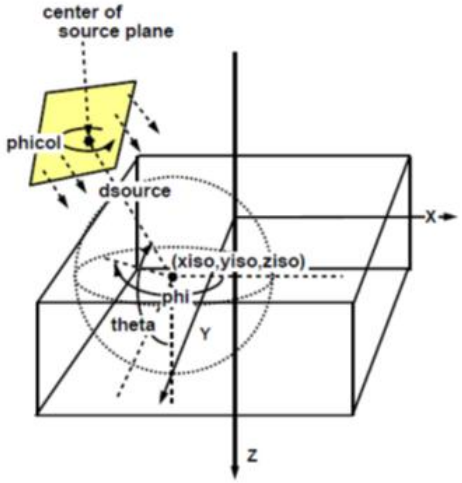

Figure 2-13: The configuration of the beam characterization model as seen in the DOSXYZnrc manual page 43.

2.13 CTCREATE

CTCREATE converts CT data into a phantom suitable for direct use by DOSXYZnrc. This enables the user to simulate particle transport inside a CT based patient model. This data can be used for dose comparisons or dose verification. The output file from CTCREATE is written into a *.egsphant file that is used by DOSXYZnrc during a simulation.

It is an ASCII file that contains information about the number and names of the media and information regarding the voxel numbers and dimensions and material density information. An example of an *.egsphant file for a CT slice of the head is shown in Figure 2-14.

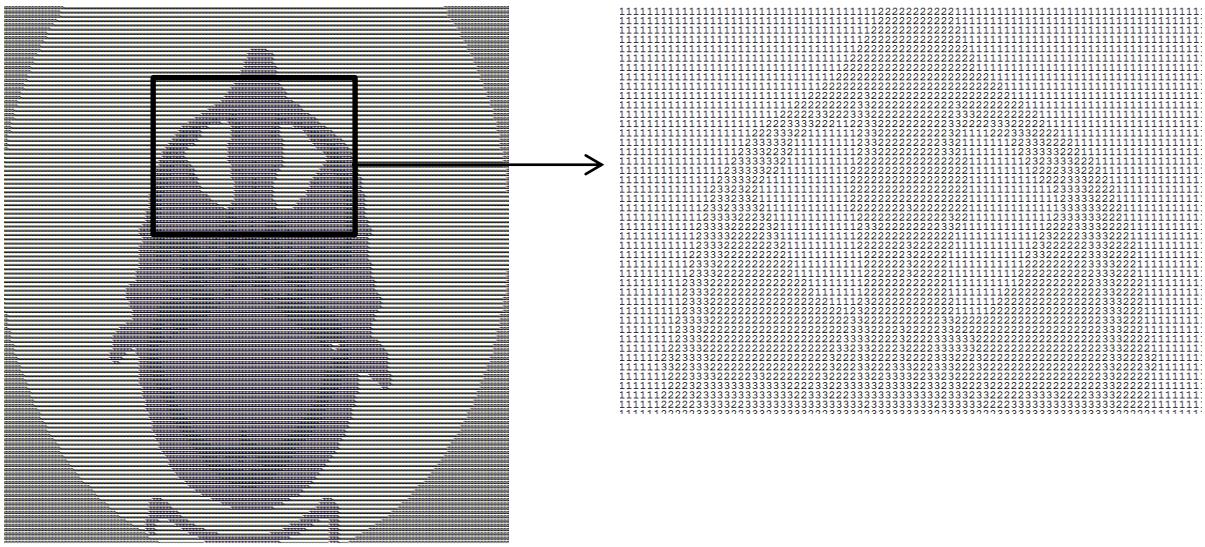

Figure 2-14: The egsphant file consisting of numbers representing the different materials present

2.14 The Source Model for the Elekta Synergy accelerator

The characteristics of a clinical photon beam can be determined by simulating the transport of particles through a model of a linac head [66-71]. In the head, the radiation beam is produced by ejecting electrons onto a bremsstrahlung target and as a result electrons and

photons exit the target. Their transport is then simulated further through the head geometry. Information like the charge, energy, weight, direction and position of each particle can be recorded in a phase space file located behind a user specified plane. Since there are millions of particle histories in a simulation, phase space files can take up large amounts of disk space. Sometimes the exact geometry of the head is unknown and an alternative is to use a source model that describes the energy and fluence distribution of the particles. Clinical radiation beams can be constructed using source models as been done by various authors [10, 72-74]. This includes creating a representation of the beam and then reconstructing the phase space data from it. The phase space data for each particle are then fed into the code for transport simulation. In a multiple-source model particles originating from different components in the linear accelerator are treated as different sub-sources. One can say that the particles in the sub-source have unique energy, spatial and angular distributions.

An accurate source model should be able to re-generate particles with the exact set of above-mentioned parameters as would be produced by the real linear accelerator from which these models are derived. Simple sources such as a single point source with a single invariant energy spectrum, yield accurate beam data over relatively small field sizes and is not general enough to use over a whole range of clinically useful field sizes [75-78]. By expanding the simple source and energy spectrum model to multiple sources and variable energy spectra the particles produced are such that dose distribution replication is within 2% / 2 mm over the useful clinical beam.

The source model used in this study consists of various components that alters the primary fluence and will be discussed in the next sections.

2.14.1 Photons

2.14.1.1 The fluence distribution alterations due to influences from different head components

2.14.1.1.a) The target fluence

The fluence from the target is modelled by a Gaussian function:

$$\phi_t = P \exp\left(\frac{-x^2}{\sigma^2}\right) \tag{2-10}$$

In Equation 2-10, P is the amplitude of the primary fluence on the beam central axis (CAX); σ represents the full width at 50% intensity and x is the radial distance from the CAX. It can be altered to change the fluence of the target as seen in Figure 2-15.

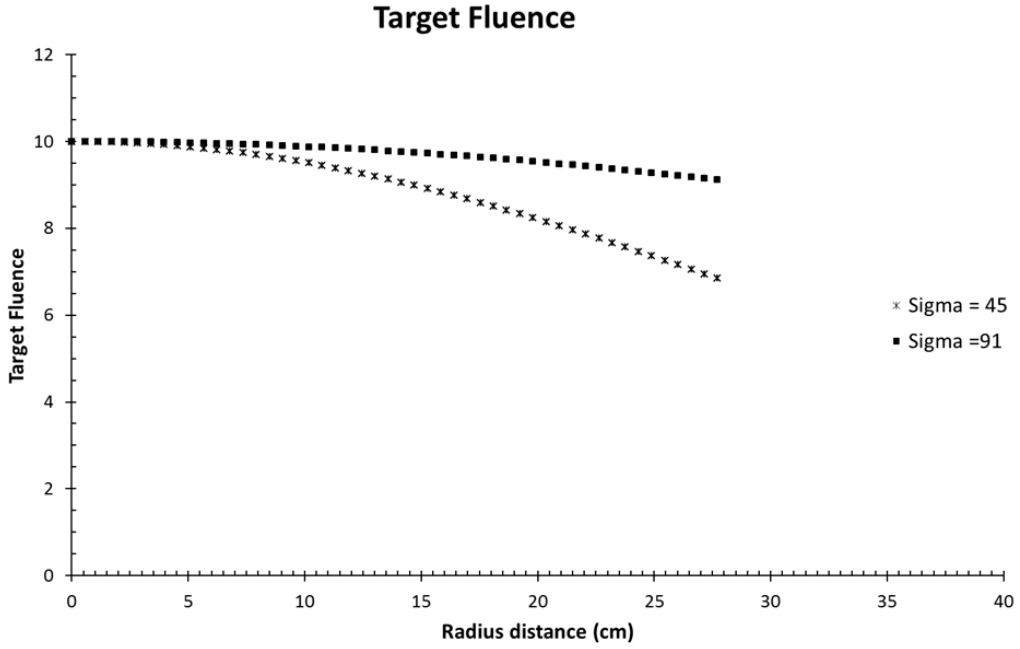

Figure 2-15: The difference seen when changing the σ value of Equation 2-10. This is the shape of the primary fluence as seen on the phase-space scoring plane.

When changing the P value of Equation 2-10 an amplitude difference occurs as shown in Figure 2-16.

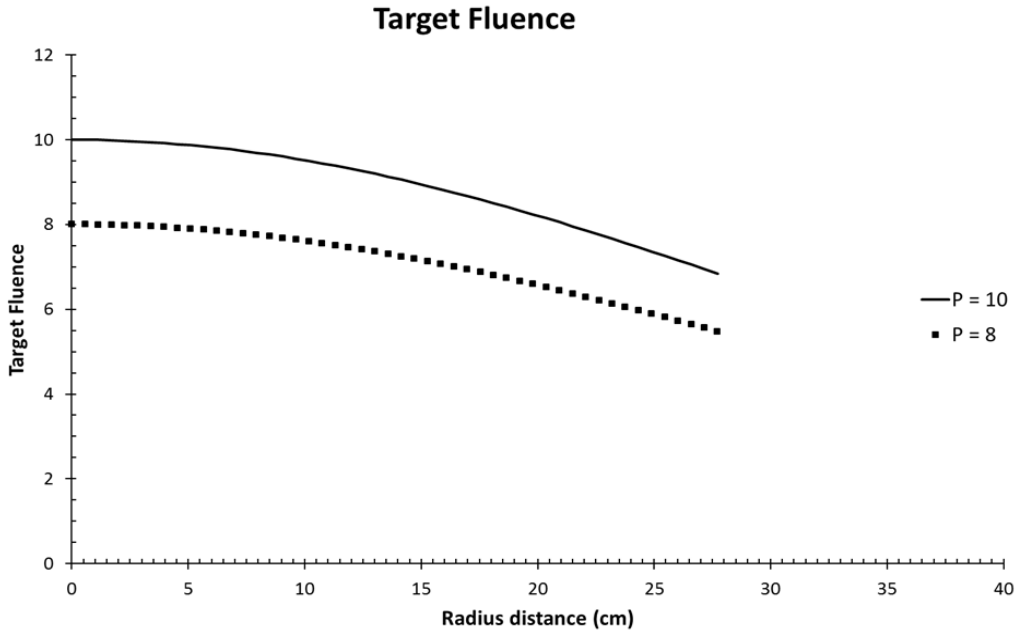

Figure 2-16: The difference in fluence seen when changing the amplitude value, *P* in Equation 2-10

2.14.1.1.b) The Primary Collimator fluence

The photon fluence from the target passes through a conical shaped primary collimator. The fluence is altered according to the method proposed by *Khan et al* in 2000 [79]. The target fluence is truncated by collimators with the use of error functions. The transmitted photons under the collimators that add to the dose outside the field edges are modelled with an exponential function. The effect of primary and transmitted fluence is shown in Equation 2-11.

$$\phi_{pc}(r) = \phi_t \, erf(X_3, \sigma) + 1[1 - erf(X_3, \sigma)] Z \exp(-\mu_1 (r - X_3)) \tag{2-11}$$

Where,

$$erf(X_3, \sigma) = \left(\sqrt{\left(1 - \exp\left(-1.245 \times \left(\left(x - X_3 \right)^2 \right) / \sigma^2 \right) \right)} \right) \tag{2-12}$$

X_3 is the outer most radial distance of the source model with a value of 27.9. x represents the lateral distance from the CAX. $[erf(X_3, \sigma)]$ represents the fluence truncation effect of the

collimators. The σ is the penumbra width of the fluence collimated by the primary collimator. The value μ_1 determines the rate of exponential reduction of the scattered primary fluence under the primary collimator as a function of x. The effect of the parameters on the fluence below the primary collimator can be seen in Figure 2-17.

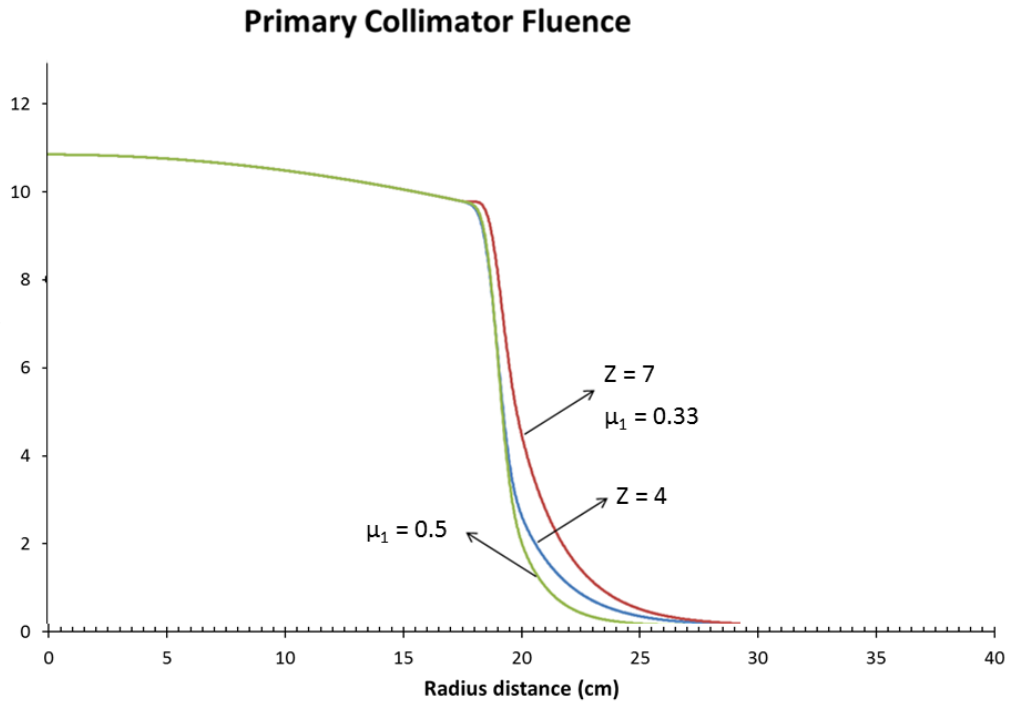

Figure 2-17: The blue curve has a Z value of 4 with and the red curve a Z value of 7. This alters the transmission underneath the collimator as well as the penumbra region. The red curve has a μ_1 value of 0.33 and the green curve a μ_1 value of 0.5. The larger value as portrait by the green curve shows a rapid exponential reduction underneath the collimator.

2.14.1.1.c) Flattening filter fluence

The flattening filter attenuates and scatters the primary fluence to ensure there is adequate beam uniformity at typical patient treatment depths (10 cm). The flattening filter is located below the primary collimator and its attenuation factor is given by Equation 2-13.

$$ff_{att}(x) = \exp(-\mu_2.t) \tag{2-13}$$

μ_2 is the effective attenuation coefficient and the flattening filter thickness (t) is approximated by a polynomial function.

$$t = 2.2302 - 0.02 * x \ - 0.011 * x^2 + 0.00029 x^3 \tag{2-14}$$

Figure 2-18 shows the fluence profile at the scoring plane after being modified by the flattening filter.

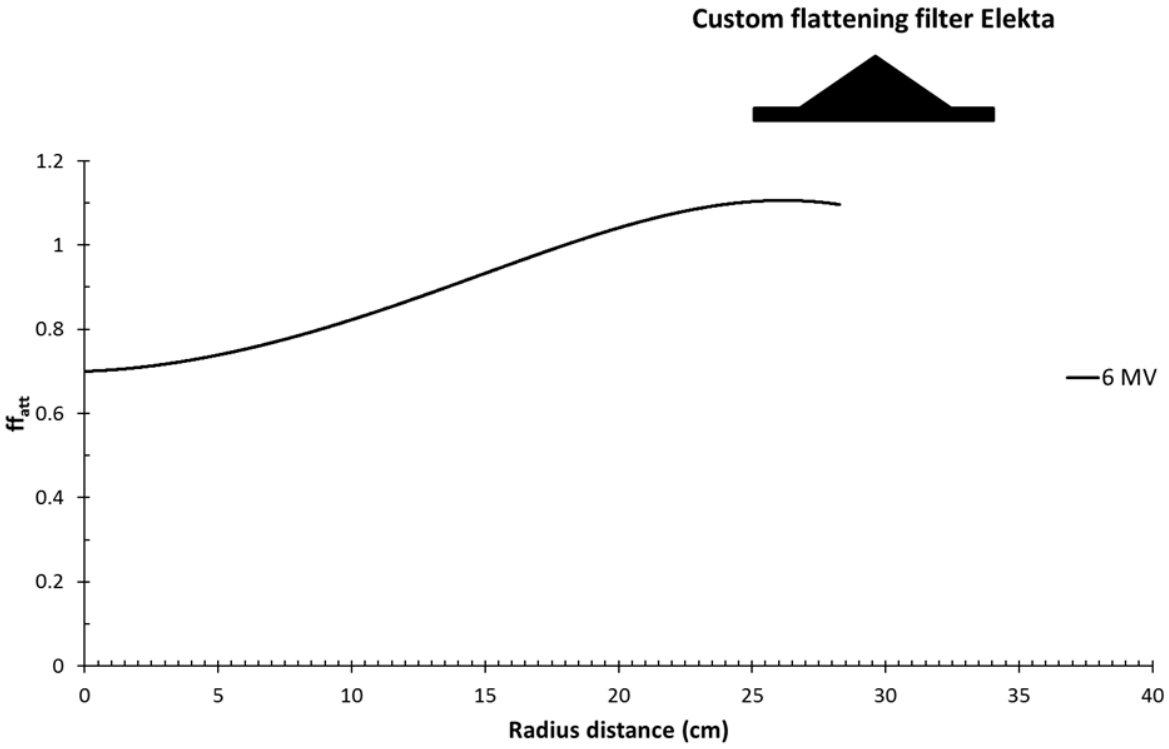

Figure 2-18: The attenuation of the flattening filter as a function of the radial distance. The custom filter design for an Elekta linear accelerator is shown as an insert.

The fluence below the flattening filter is given by:

$$\phi_{pc+ff} = \phi_{pc}(x).\, ff_{att}(x) \tag{2-15}$$

The fluence up to this point can be seen in Figure 2-19.

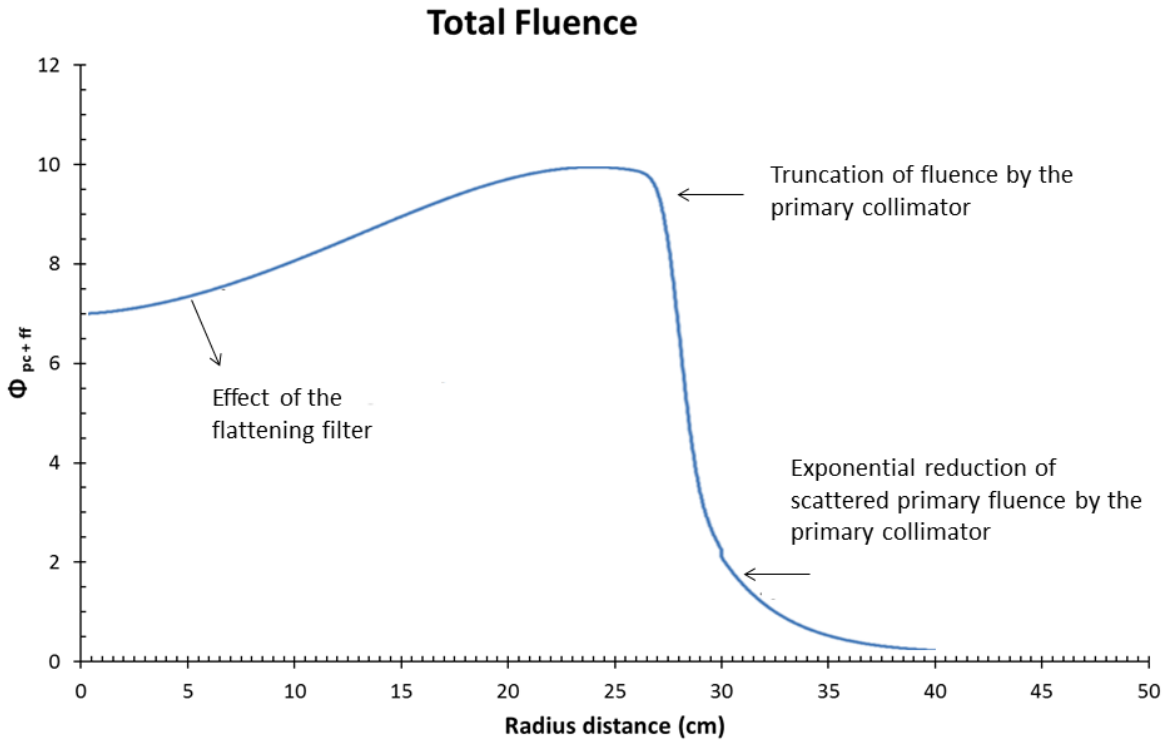

Figure 2-19: The total fluence below the flattening filter.

In the next sections the effects of the jaws and MLC's are modelled.

2.14.1.1.d) The Jaw influence on ϕ_{pc+ff}

The two pairs of opposing jaws are used to collimate and define regular fields. Error functions are used to model the beam penumbra. The effect of σ can be seen in Figure 2-20.

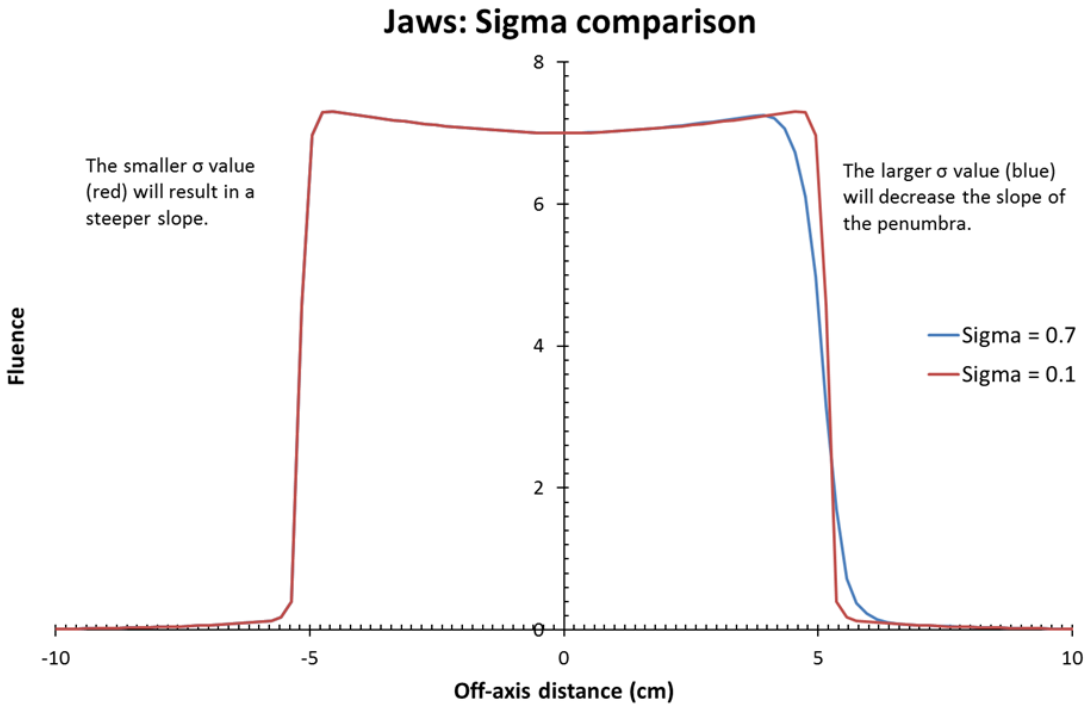

Figure 2-20: The effect of σ on the penumbra width of the field.

A small σ value will result in a penumbra with a steep gradient as indicated by the red line in Figure 2-20. By increasing the σ value a decrease in the slope of the penumbra is achieved as seen for the blue line in Figure 2-20.

The transmission through the jaws as well as the scatter outside the field is modelled by an exponential function which is the same as in the case of the primary collimator.

The jaw and MLC configuration can be seen in Figure 2-21.

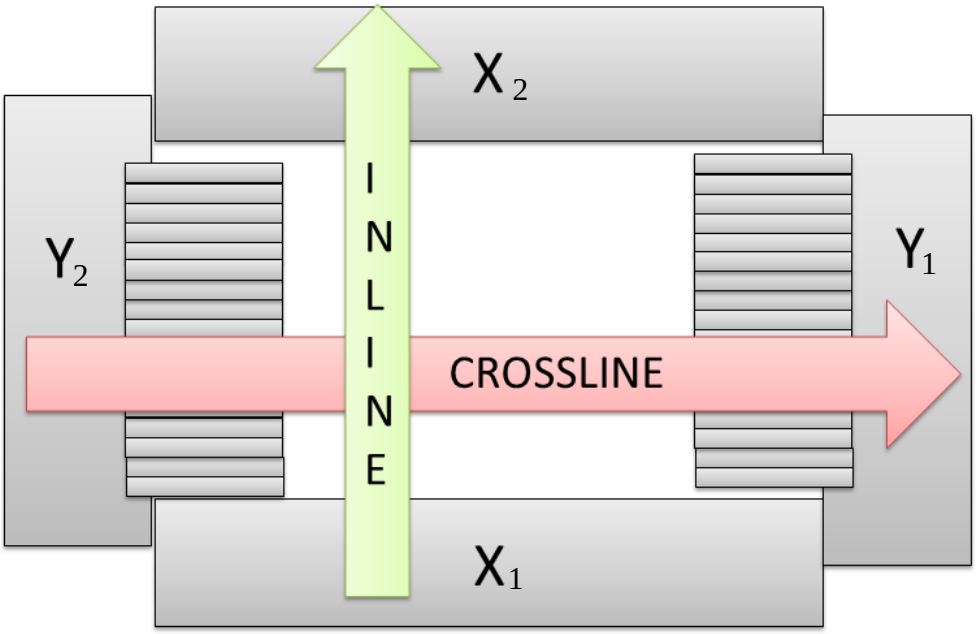

Figure 2-21: The jaw and MLC configuration of the source model

The modulation of the fluence by the X_1 jaw is modelled in the open part of the field as well as under the jaw. This is displayed graphically in Figure 2-22.

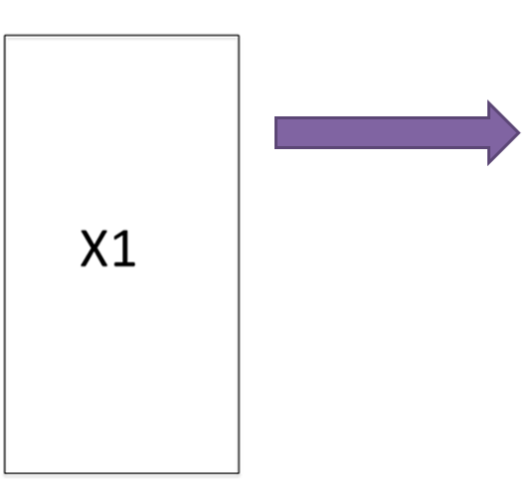

$$\text{If } x \geq X_1 \text{ then } \phi_{X_1} = 1 - erf(x_1, \sigma) \tag{2-16}$$

$$\text{If } x < X_1 \text{ then } [1 - erf(x_1, \sigma)] + T \times \exp(-\mu_{out} |x - X_1|) \tag{2-17}$$

Figure 2-22: Top) The error function used when modelling the open field with no added transmission. Bottom) The error function and transmission used when modelling the truncation effect as well as transmission and scatter under the jaw.

The variable x indicates the radial position from the CAX. The x position of the error function at its half maximum is given by x_1. The value of T in Equation 2-17 can be adjusted and represents transmission under the jaw. The value μ_{out} determines the rate of reduction of the transmitted and scattered primary photons underneath the jaw.

The following figures indicate how the different source model parameters change the fluence profile when collimated by the jaws.

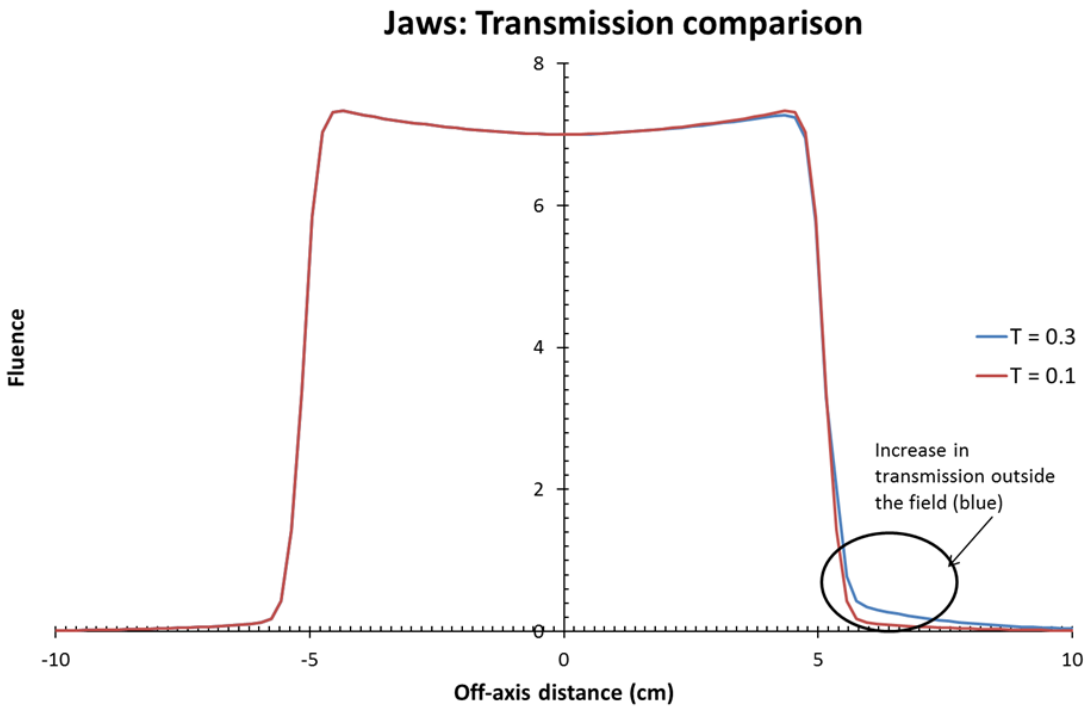

Figure 2-23: The effect of changing the value of the transmission (*T)*. The blue line has a larger T value and the increase in the transmission can be seen.

The combined effect of changing σ and the transmission can be seen below in Figure 2-24.

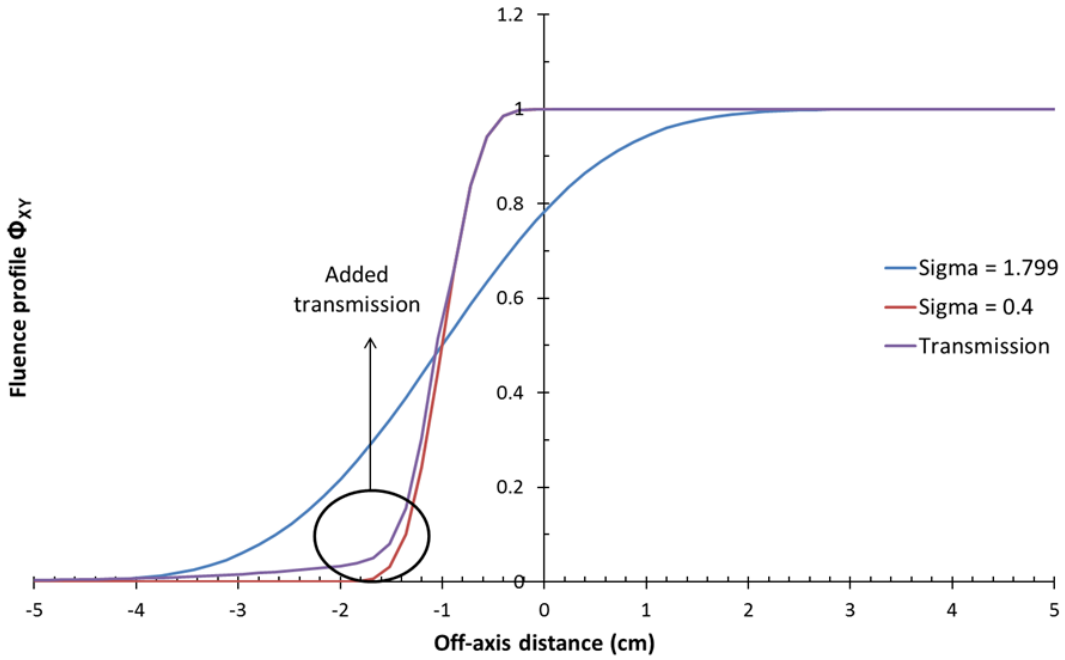

Figure 2-24: The changes in the fluence profile when altering σ and the transmission.

By changing the σ and transmission values of the fluence profile for different field sizes, an acceptable fit for the dose profiles can be obtained.

Equation 2-16 and 2-17 is applied to jaw X and can be applied to the rest of the jaws.

The total effect of the four independent jaws is given by:

$$\phi_{XY} = \phi_{X_1}\phi_{X_2}\phi_{Y_1}\phi_{Y_2} \tag{2-18}$$

2.14.1.1.e) Multi-leaf collimators

The MLC's truncate the field in die crossline direction and is modelled in a similar way as the jaws. Each leaf can be modelled individually and consists of three edges, each with their own σ and transmission value as shown in Figure 2-25.

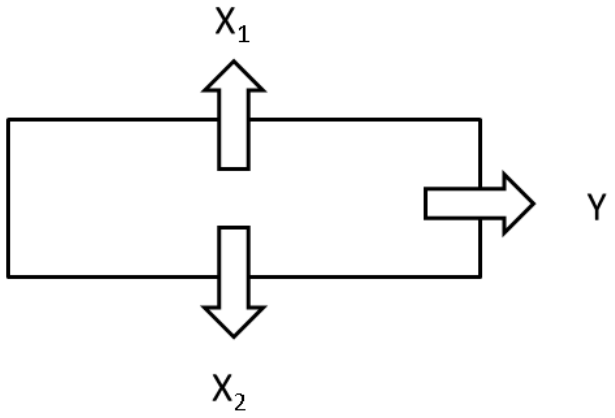

Figure 2-25: A MLC with the arrows indicating the directions in which each of the error functions are applied.

For the transmission the same principle applies as for the jaws.

For the open part of the field:

$$\phi_{mlc_{X_1}} = 1 - erf\left(mlc_{X_1}, \sigma_{xmlc}\right) \tag{2-19}$$

Underneath the MLC leaf

$$\phi_{mlc_{X_1}} = 1 - erf\left(mlc_{X_1}, \sigma_{xmlc}\right) + T \times \exp\left(-\mu_{out\_xmlc} \left| x - mlcx1 \right|\right) \tag{2-20}$$

$$\mu_{out\_xmlc} = mu_{1\_mlc} + mu_{2\_mlc} \times \exp\left(A_{mlc} \times edge_{left/right\_mlc}\right) \tag{2-21}$$

The effect of the transmission is the same as in the case of the jaws. Equations 2-19 to 2-21 are applied for the other two edges of the leaf as well.

The total effect of a single leaf is expressed as:

$$\phi_{mlc_{XY}} = 1 - \left(\phi_{mlc_{X_1}} . \phi_{mlc_{X_2}} \phi_{mlc_Y}\right)(1 - T) \tag{2-22}$$

The net total fluence that exits the linac for a specific field size is expressed as:

$$Total\phi = \phi_{pc}(r) . ff_{att}(r) . \phi_{jaws} . \phi_{MLC} \tag{2-23}$$

2.14.1.1.f) Wedged fields

A wedge can be inserted in the open field and is modelled in this study with a function that replicates the attenuation caused by it. The thickness of the wedge (d_{wedge})is modelled by Equation 2-24. Fitting parameters *C1* can be altered to model the effective thickness of the wedge on different field sizes.

$$d_{wedge} = 5.0 - 0.0401 \times (C1 - x) + 0.00011 \times (C1 - x)^2 \quad (2\text{-}24)$$

In Figure 2-26 one can see the exponential function used to alter the exit fluence to include the attenuation of the wedge. The fluence under the wedge is given by Equation 2-25.

$$\phi_{final} = \phi_{exit(x)} \times d_{\exp}(x) \quad (2\text{-}25)$$

where d_{exp} is defined by

$$d_{\exp}(x) = \exp\left(-k_1 \times d_{wedge}(x)\right) / k_2 \quad (2\text{-}26)$$

With variable constants k_1 and k_2

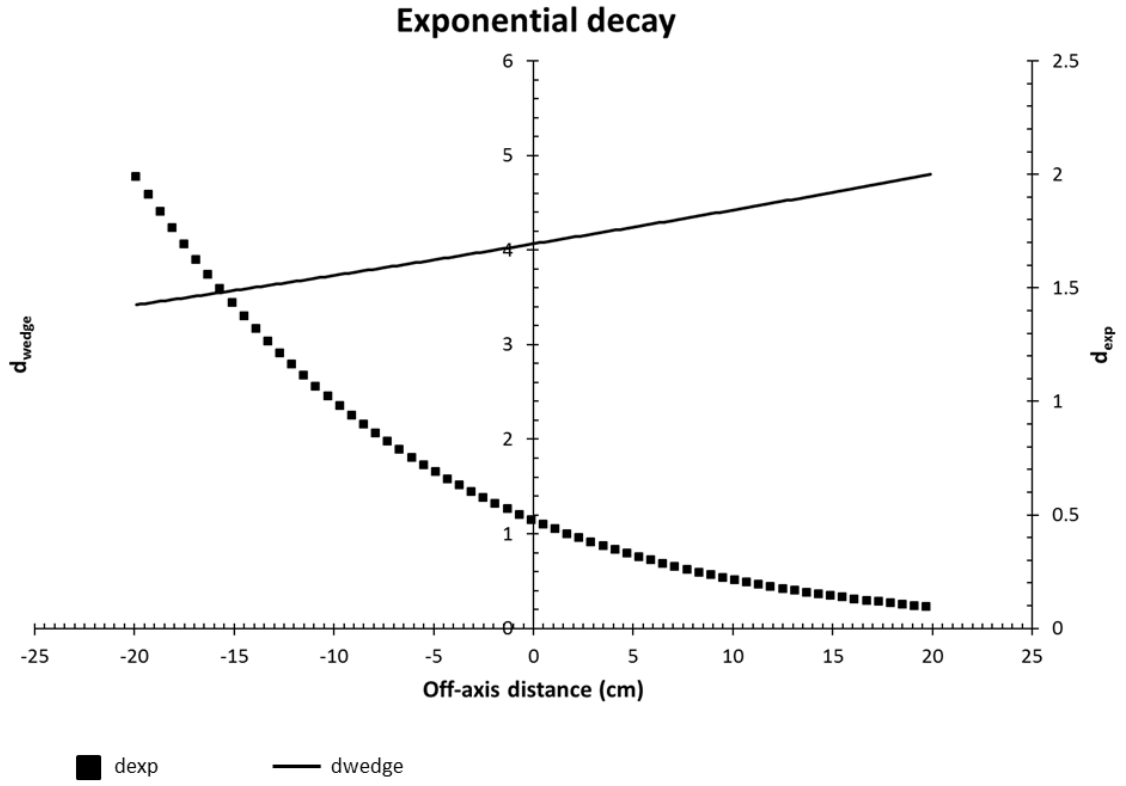

Figure 2-26: d_{wedge} over the fluence in the x-direction and the exponential function that is used for the attenuation of the fluence.

2.15 The photon energy spectra

Knowledge of the photon energy spectrum is important for accurate dose calculations with the use of a source model. Good results have been demonstrated by Desobry *et al* [80] and Baker *et al* [81, 82] as well as by Partridge *et al* [83] for reconstructing spectra from modified Schiff equations.

The modified Schiff formula [83] was used to calculate the bremsstrahlung photon distribution emanating from the target. It is a function of electron energy that will strike the target.

The photon energy distribution $\phi_p(E,r)$ is given by:

$$\phi_p(E,r)=\frac{1}{E}\left[\left(1-\frac{E}{E_0}\right).(\ln\eta(E)-1)+\alpha(r)\left(\frac{E}{E_0}\right)^2.(\ln\eta(E)-0.5)\right] \quad (2\text{-}27)$$

Where E_0 and E are the incident electron energy and the final electron energy respectively.

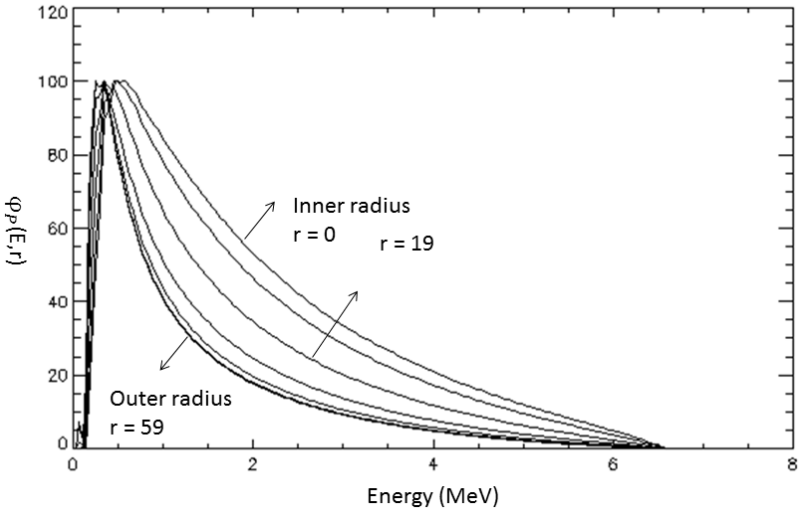

Figure 2-27: The photon energy distribution over different radii.

The value for η is obtained with the following equation:

$$\eta(E)=\frac{1}{\sqrt{\left[\frac{0.511E}{2E_0(E_0-E)}\right]^2+\left[\frac{Z_w^{1/3}}{111.0}\right]^2}} \quad (2\text{-}28)$$

The parameter Z_w represents the tungsten target with an atomic number of 74. The value of 111.0 is Schiff's constant.

The radial dependence of α in Equation 2-29 is approximated by a linear function

$$\alpha(x)=0.3566-0.0087x \quad (2\text{-}29)$$

A second term can be added to describe the exponential attenuation in the target itself

$$Target_{att} = \exp\left(-\mu_w(E).t_w\right) \tag{2-30}$$

Where μ_w is the attenuation coefficient for tungsten and t_w is a free parameter for the target thickness.

Other components such as the flattening filter will also cause significant filtration of the photon beam. These components consist of lower-Z materials such as aluminium or stainless steel. The difference in atomic number for both cases cause that different components of the energy spectrum will be altered; hence a third term is added.

$$Flattening\ \ filter_{att} = \exp\left(-\mu_{ss}(E).t_{ss}(x)\right) \tag{2-31}$$

The parameters are representative of stainless steel (ss) and x accounts for the radial dependence of the flattening filter.

The thickness profile for the flattening filter is approximated by:

$$t_{ss} = 2.5528 - 0.010221r - 0.016438r^2 + 0.00078417r^3 - 0.000010411r^4 \tag{2-32}$$

2.16 GAFCHROMIC® EBT2 film

Apart from the above source model, film measurements for MLC-fields are also used as benchmarking data to test the source model.

GAFCHROMIC® EBT2 film can be used for dosimetry in the radiotherapy environment. It is a self-developing film with an active layer of a synthetic polymer [84]. This film can measure absorbed dose up to 8 Gy. It is unaffected by interior room light but it is best to store it in a dark place when not in use.

Once exposed, this film can be read with a document scanner in the red, green and blue bands. The maximum response of the film is produced in the red component and can be extracted and used for its calibration.

This film pieces must be scanned in the same orientation to exclude orientation dependencies [85-87]. It also undergoes post-exposure polymerization and it is advisable to wait 24 hours after irradiation before it is scanned.

The following equation is usually used to convert the scanner values to density values:

$$Density = -\log(raw\_values / 65535) \tag{2-33}$$

For calibration Equation 2-34 is used [88].

$$X(D,n) = a + b/(D - c) \tag{2-34}$$

Where $X(D,n)$ is the scanner density response, D is the film dose in cGy and a,b and c are constants.

2.17 Summary

Monte Carlo is the most accurate dose calculation algorithm to date. By using this code together with a source model it is possible to acquire field profiles and dose distributions that are comparable to those obtained with a linac.

The source model consists of various parts, each representative of a beam modifying component in a linac. These components are modelled by means of mathematical equations consisting of parameters that can be altered as desired.

This complex source model is simplified by means of a user friendly GUI. This GUI makes it easy to obtain input files for different field sizes each consisting of different field defining parameters and will be described in Chapter 3. Field fluence can be displayed

graphically as well as plots e.g. energy spectrum to give a representation of the effects of the parameters.

Dose verification can be performed with high-precision GAFCHROMIC® EBT2 film to evaluate the ability of the source model to reproduce dose distributions in suitable phantoms.

2.18 Bibliography

1. Bielajew AF. Chapter 1: History of Monte Carlo [Internet]. Available from: http://www-personal.umich.edu/~bielajew/chapter1withGraphics.pdf

2. Ulam SM. Adventures of a mathematician. second edition. Berkeley: University of California Press; 1991.

3. Metropolis N. The beginning of the Monte Carlo Method. Los Alamos Sci Spec Issue. 1987;125 – 130.

4. Eckhart R. STAN ULAM, JOHN VON NEUMANN, and the MONTE CARLO METHOD. Los Alamos Sci Spec Issue. 1987;131 – 141.

5. Wilson RR. Monte Carlo Study of Shower Production. Phys Rev. 1952 May 1;86(3):261–9.

6. Metropolis N, Ulam S. The Monte Carlo Method. J Am Stat Assoc. 1949;44(247):335–41.

7. Nahum AE. The Computation of dose distributions in electron beam radiotherapy. Umeå University; 1985. 356 p.

8. Kase K, Bjärngard B, Attix F. The Dosimetry of Ionizing Radiation, Volume 3: Volume III. Academic Press; 1990.

9. D. W. O. Rogers AFB. Monte Carlo techniques of electron and photon transport for radiation dosimetry. Doimetry Ioniz Radiat. III:427 – 539.

10. Ma C-M, Jiang SB. Monte Carlo modelling of electron beams from medical accelerators. Phys Med Biol. 1999 Dec 1;44(12):R157.

11. Andreo P. Monte Carlo techniques in medical radiation physics. Phys Med Biol. 1991 Jul 1;36(7):861.

12. Rogers DWO. Fifty years of Monte Carlo simulations for medical physics. Phys Med Biol. 2006 Jul 7;51(13):R287.

13. Fippel M, Haryanto F, Dohm O, Nusslin F, Kriesen S. A virtual photon energy fluence model for Monte Carlo dose calculation. Med Phys. 2003;30(3):301–11.

14. Verhaegen F, Seuntjens J. Monte Carlo modelling of external radiotherapy photon beams. Phys Med Biol. 2003 Nov 7;48(21):R107–R164.

15. Fix MK, Keall PJ, Dawson K, Siebers JV. Monte Carlo source model for photon beam radiotherapy: photon source characteristics. Med Phys. 2004;31(11):3106–21.

16. Ma C-M, Mok E, Kapur A, Pawlicki T, Findley D, Brain S, et al. Clinical implementation of a Monte Carlo treatment planning system. Med Phys. 1999 Oct 1;26(10):2133–43.

17. Mackie TR. The OMEGA project: comparison among EGS4 electron beam simulations, 3D Fermi-Eyges calculations, and dose measurements. Proc. 11th Int. Conf. on the Use of Computers in Radiation Therapy (Manchester, UK); 1994. p. 152 – 153.

18. Mohan R. Why Monte Carlo? Proc. 11th Int. Conf. on the Use of Computers in Radiation Therapy (Salt Lake City, UT)); 1997.

19. Nahum AE. Conformal therapy needs Monte Carlo dose computation. Proc. Challenges in Conformal Radiotherapy (Nice: European Society for Therapeutic Radiology and Oncology); 1997. p. 1 – 11.

20. Shortt KR, Ross CK, Bielajew AF, Rogers DWO. Electron beam dose distributions near standard inhomogeneities. Phys Med Biol. 1986 Mar 1;31(3):235.

21. DeMarco JJ, Solberg TD, Smathers JB. A CT-based Monte Carlo simulation tool for dosimetry planning and analysis. Med Phys. 1998 Jan 1;25(1):1–11.

22. Fragoso M, Wen N, Kumar S, Liu D, Ryu S, Movsas B, et al. Dosimetric verification and clinical evaluation of a new commercially available Monte Carlo-based dose algorithm for application in stereotactic body radiation therapy (SBRT) treatment planning. Phys Med Biol. 2010 Aug 21;55(16):4445.

23. Chaves A, Lopes MC, Alves CC, Oliveira C, Peralta L, Rodrigues P, et al. Basic dosimetry of radiosurgery narrow beams using Monte Carlo simulations: A detailed study of depth of maximum dose. Med Phys. 2003 Oct 14;30(11):2904–11.

24. Cheung JYC, Yu KN, Yu CP, Ho RTK. Monte Carlo calculation of single-beam dose profiles used in a gamma knife treatment planning system. Med Phys. 1998 Sep 1;25(9):1673–5.

25. Cheung JYC, Yu KN, Ho RTK, Yu CP. Monte Carlo calculated output factors of a Leksell Gamma Knife unit. Phys Med Biol. 1999 Dec 1;44(12):N247.

26. Kubsad SS, Rockwell Mackie T, Gehring MA, Misisco DJ, Paliwal BR, Mehta MP, et al. Monte Carlo and convolution dosimetry for stereotactic radiosurgery. Int J Radiat Oncol. 1990 Oct;19(4):1027–35.

27. Mack A, Scheib SG, Major J, Gianolini S, Pazmandi G, Feist H, et al. Precision dosimetry for narrow photon beams used in radiosurgery—Determination of Gamma Knife® output factors. Med Phys. 2002 Aug 26;29(9):2080–9.

28. Sánchez-Doblado F, Andreo P, Capote R, Leal A, Perucha M, Arráns R, et al. Ionization chamber dosimetry of small photon fields: a Monte Carlo study on stopping-power ratios for radiosurgery and IMRT beams. Phys Med Biol. 2003 Jul 21;48(14):2081.

29. Moskvin V, DesRosiers C, Papiez L, Timmerman R, Randall M, DesRosiers P. Monte Carlo simulation of the Leksell Gamma Knife®: I. Source modelling and calculations in homogeneous media. Phys Med Biol. 2002 Jun 21;47(12):1995.

30. Seuntjens J, Verhaegen F. Comments on `Ionization chamber dosimetry of small photon fields: a Monte Carlo study on stopping-power ratios for radiosurgery and IMRT beams'. Phys Med Biol. 2003 Nov 7;48(21):L43.

31. Sixel KE, Faddegon BA. Calculation of x-ray spectra for radiosurgical beams. Med Phys. 1995 Oct 1;22(10):1657–61.

32. Verhaegen F, Das IJ, Palmans H. Monte Carlo dosimetry study of a 6 MV stereotactic radiosurgery unit. Phys Med Biol. 1998 Oct 1;43(10):2755.

33. Otto K. Volumetric modulated arc therapy: IMRT in a single gantry arc. Med Phys. 2007 Dec 26;35(1):310–7.

34. Fix MK, Manser P, Frei D, Volken W, Mini R, Born EJ. An efficient framework for photon Monte Carlo treatment planning. Phys Med Biol. 2007 Sep 21;52(19):N425.

35. Fix MK, Keall PJ, Siebers JV. Photon-beam subsource sensitivity to the initial electron-beam parameters. Med Phys. 2005 Mar 29;32(4):1164–75.

36. Chetty I, DeMarco JJ, Solberg TD. A virtual source model for Monte Carlo modeling of arbitrary intensity distributions. Med Phys. 2000;27(1):166–72.

37. Martinez-Rovira I, Sempau J, Prezado Y. Monte Carlo-based treatment planning system calculation engine for microbeam radiation therapy. Med Phys. 2012 May;39(5):2829–38.

38. Chetty IJ, Cygler J. MO-B-105-01: Successes and Challenges Associated with Monte Carlo Treatment Planning in the Clinic. Med Phys. 2013 Jun 1;40(6):392–392.

39. Johns HE, Cunningham JR. The Physics of Radiology. 4th ed. Charles C Thomas Pub Ltd; 1983. p. 796.

40. Adeel A. Handbook of Radiotherapy Physics - Theory and Practice - Taylor & Francis (2007) [Internet]. [cited 2014 Apr 29]. Available from: http://www.academia.edu/2430074/Handbook_of_Radiotherapy_Physics_-_Theory_and_Practice_-_Taylor_and_Francis_2007_

41. Ball J, Moore AD, Turner S. Ball and Moore's Essential Physics for Radiographers. 4th edition. Wiley-Blackwell; 2008. 424 p.

42. Beutel J. Handbook of Medical Imaging: Physics and psychophysics. SPIE Press; 2000. 976 p.

43. Hayat MA. Cancer Imaging: Instrumentation and Applications. Academic Press; 2007. 794 p.

44. Principles of Radiation Therapy | Cancer Network [Internet]. 2007 [cited 2014 Jan 10]. Available from: http://www.cancernetwork.com/articles/principles-radiation-therapy-0

45. Podgorsak EB. Radiation Oncology Physics: A Handbook for Teachers and Students. Vienna, Austria: International Atomic Energy Agency; 2005. p. 657.

46. Seco J, Verhaegen F. Monte Carlo Techniques in Radiation Therapy. CRC Press; 2013. 344 p.

47. Kawrakow I, Bielajew AF. On the condensed history technique for electron transport. Nucl Instrum Methods Phys Res Sect B Beam Interact Mater At. 1998 Jul;142(3):253–80.

48. Walters BRB, Kawrakow I. Technical note: Overprediction of dose with default PRESTA-I boundary crossing in DOSXYZnrc and BEAMnrc. Med Phys. 2007 Jan 25;34(2):647–50.

49. Duane S, Bielajew AF, Rogers DWO. Use of ICRU-37/NBS Collision Stopping Powers in the EGS4 System. 1989 Mar;

50. Knuth DE. SEMINUMERICAL ALGORITHMS: The Art of computer programming. third edition. 1997.

51. L'Ecuyer P. Random numbers for simulation. Commun ACM. 1990 Oct 1;33(10):85–97.

52. James F. A review of pseudorandom number generators. Comput Phys Commun. 1990 Oct;60(3):329–44.

53. Bielajew AF. Fundamentals of the Monte Carlo method for neutral and charged particle transport. 2000.

54. Coddington PD. Analysis of Random Number Generators Using Monte Carlo Simulation. 1993;

55. Fuller AT. The period of pseudo-random numbers generated by Lehmer's congruential method [Internet]. Cambridge University Engineering Department, Control Engineering Group, Mill Lane, Cambridge CB2 1RX; 1975. p. 173–7. Available from: http://comjnl.oxfordjournals.org/

56. Harris J. Some Notes On Multiplicative Congruential Random Number Generators With Mersenne Prime Modulus 261-1. J S C Acad Sci [Internet]. 2003 Jan 1;1(1). Available from: http://scholarcommons.sc.edu/jscas/vol1/iss1/10

57. Metcalf P, Kron T, Hoban P. The Physics of Radiotherapy X-Rays. Medical Physics Publishing, Madison, Wisconsin; 1997.

58. Kawrakow I, Mainegra-Hing E, Rogers DWO, Tessier F, Walters BRB. The EGSnrc Code System: Monte Carlo Simulation of Electron and Photon Transport. 2010. Report No.: NRCC Report PIRS-701.

59. Walker AJ. An Efficient Method for Generating Discrete Random Variables with General Distributions. ACM Trans Math Softw. 1977 Sep;3(3):253–6.

60. Schwartz K. Darts, Dice, and Coins: Sampling from a Discrete Distribution.

61. Klein O, Nishina Y. Über die Streuung von Strahlung durch freie Elektronen nach der neuen relativistischen Quantendynamik von Dirac. Z Für Phys. 1929 Nov 1;52(11-12):853–68.

62. Bielajew AF. Lecture's notes: Photon Monte Carlo simulation. Ottawa, Canada: Institute for National Measurement Standards National Research Council of Canada; Report No.: Report PIRS-0393.

63. Keall PJ, Siebers JV, Jeraj R, Mohan R. The effect of dose calculation uncertainty on the evaluation of radiotherapy plans. Med Phys. 2000 Mar 1;27(3):478–84.

64. Bielajew AF, Rogers DWO. Lecture notes: Variance Reduction Techniques. Ottawa, Canada: Institute for National Measurement Standards National Research Council of Canada; Report No.: Report PIRS - 0396.

65. Salvat F, Fernández-Varea JM, Sempau J. PENELOPE-2006: A Code System for Monte Carlo Simulation of Electron and Photon Transport.

66. Hartmann-Siantar CL. Lawrence Livemore National Laboratory's PEREGRINE Project.

67. Kuster G, Bortfield T, Schlegel W. Monte Carlo simulations of radiation beams from radiotherapy units and beam limitimg devices using the program GEANT. Proc 12th ICCR Salt Lake City USA. 1997;

68. Lovelock DMJ, Chui CS, Mohan R. A Monte Carlo model of photon beams used in radiation therapy. Med Phys. 1995 Sep 1;22(9):1387–94.

69. Ma CM, Faddegon BA, Rogers DWO, Mackie TR. Accurate characterization of Monte Carlo calculated electron beams for radiotherapy. Med Phys. 1997 Mar 1;24(3):401–16.

70. Mohan R, Chui C, Lidofsky L. Energy and angular distributions of photons from medical linear accelerators. Med Phys. 1985 Sep 1;12(5):592–7.

71. Rogers DWO. BEAM: A Monte Carlo code to simulate radiotherapy treatment units. Med Phys. 1995;22(5):503.

72. Deng J, Jiang SB, Kapur A, Li J, Pawlicki T, Ma C-M. Photon beam characterization and modelling for Monte Carlo treatment planning. Phys Med Biol. 2000 Feb 1;45(2):411–27.

73. Wittenau AES von, Jr PMB, Cox LJ. Patient-dependent beam-modifier physics in Monte Carlo photon dose calculations. Med Phys. 2000 May 1;27(5):935–47.

74. Fix MK, Stampanoni M, Manser P, Born EJ, Mini R, Rüegsegger P. A multiple source model for 6 MV photon beam dose calculations using Monte Carlo. Phys Med Biol. 2001 May 1;46(5):1407–27.

75. Scott AJD, Nahum AE, Fenwick JD. Monte Carlo modeling of small photon fields: Quantifying the impact of focal spot size on source occlusion and output factors, and exploring miniphantom design for small-field measurements. Med Phys. 2009 Jun 12;36(7):3132–44.

76. Bush K, Zavgorodni S, Beckham W. Inference of the optimal pretarget electron beam parameters in a Monte Carlo virtual linac model through simulated annealing. Med Phys. 2009 May 27;36(6):2309–19.

77. Cho W, Kielar KN, Mok E, Xing L, Park J-H, Jung W-G, et al. Multisource modeling of flattening filter free (FFF) beam and the optimization of model parameters. Med Phys. 2011 Mar 15;38(4):1931–42.

78. Sterpin E, Chen Y, Lu W, Mackie TR, Olivera GH, Vynckier S. On the relationships between electron spot size, focal spot size, and virtual source position in Monte Carlo simulations. Med Phys. 2011 Feb 24;38(3):1579–86.

79. Khan FM, Higgins PD. Field equivalence for clinical electron beams. Phys Med Biol. 2001 Jan 1;46(1):N9–N14.

80. Desobry GE, Boyer AL. Bremsstrahlung review: An analysis of the Schiff spectrum. Med Phys. 1991;18(3):497–505.

81. Desobry GE, Boyer AL. An analytic calculation of the energy fluence spectrum of a linear accelerator. Med Phys. 1994;21(12):1943–52.

82. Baker CR, Peck KK. Reconstruction of 6 MV photon spectra from measured transmission including maximum energy estimation. Phys Med Biol. 1997 Nov 1;42(11):2041–51.

83. Partridge M. Reconstruction of megavoltage photon spectra from electronic portal imager derived transmission measurements. Phys Med Biol. 2000 Oct 1;45(10):N115–N131.

84. GAFCHROMIC® EBT2 SELF-DEVELOPING FILM FOR RADIOTHERAPY DOSIMETRY [Internet]. International speciality products; 2009 Feb. Available from: http://www.fimecorp.com/docs/GAFCHROMIC%20EBT2%20Technical%20Brief%20-%20Rev.%201.pdf

85. Aldelaijan S, Mohammed H, Tomic N, Liang L-H, DeBlois F, Sarfehnia A, et al. Radiochromic film dosimetry of HDR [sup 192]Ir source radiation fields. Med Phys. 2011;38(11):6074–83.

86. Chair AN-R, Blackwell CR, Coursey BM, Gall KP, Galvin JM, McLaughlin WL, et al. Radiochromic film dosimetry: Recommendations of AAPM Radiation Therapy Committee Task Group 55. Med Phys. 1998;25(11):2093–115.

87. Butson MJ, Cheung T, Yu PKN. Scanning orientation effects on Gafchromic EBT film dosimetry. Australas Phys Eng Sci Med. 2006 Sep 1;29(3):281–4.

88. FilmQA™ Pro [Internet]. Available from: http://www.ashland.com/products/filmqa-pro-software

3. CHAPTER 3: METHODS & MATERIALS

3.1 Photon beam data acquisition in a water tank

Water tank scans of beam data were acquired to act as a benchmark against simulated MC data. The water tank measurements were taken with a Scanditronix Wellhöfer Blue Phantom scanning system as seen in Figure 3-1. The OmniPro Accept software (version 6.5) was used for the acquisition of the beam data. Two types of ionisation chambers were used with different size volumes: A 0.01 cm^3 PTW FREIBURG® Pinpoint chamber for small field sizes up to a 5 × 5 cm^2 and a CC13 PTW FREIBURG® chamber for the larger field sizes.

Field profile measurements were made for field sizes from a 1 × 1 cm^2 field to a 40 × 40 cm^2 field. Profiles in the inline- and crossline direction as well as percentage depth dose curves were measured. Wedged field profile data were acquired for a 10 × 10 cm^2, 20 × 20 cm^2 and a 30 × 40 cm^2 field. Offset profiles were acquired for 10 × 10 cm^2, 15 × 15 cm^2 and 20 × 20 cm^2 fields in both the inline and crossline directions.

All the measurements were done at a SSD of 100 cm at depths of 1.5 cm, 5 cm, 10 cm, 20 cm and 30 cm. Enough water was added to the tank to allow for adequate back scatter. Measured data were denoized with the Omni-Pro software package before it was used for comparison with the Monte Carlo data.

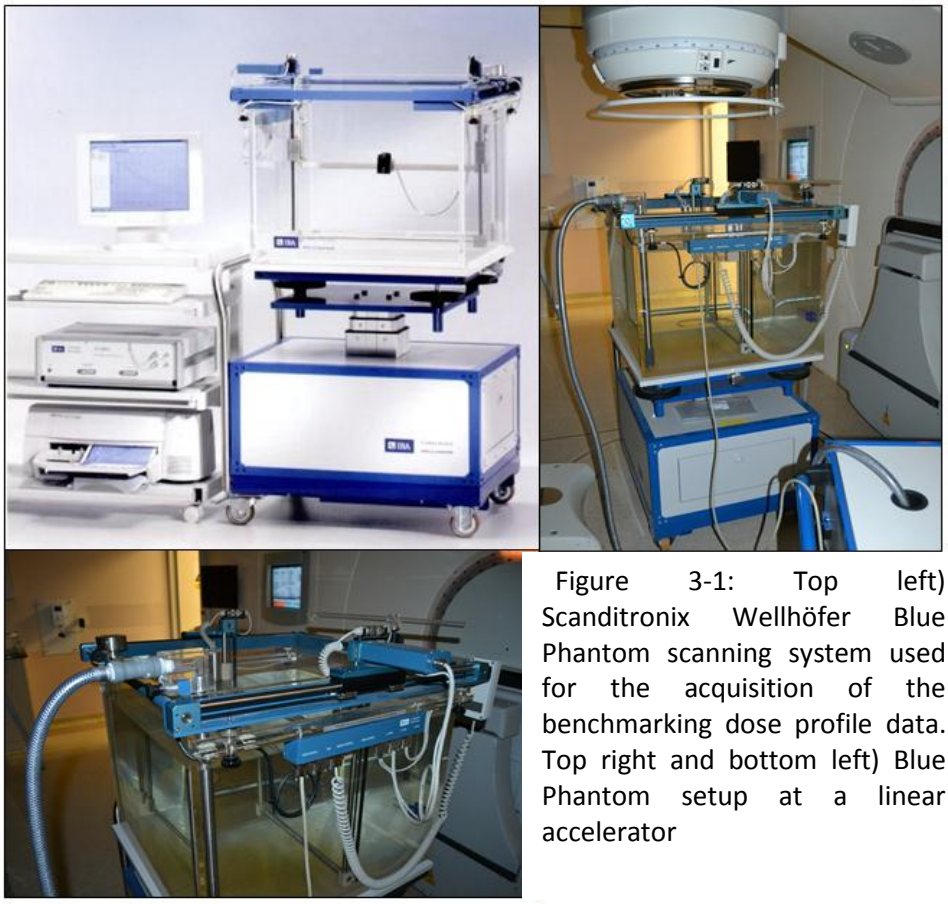

Figure 3-1: Top left) Scanditronix Wellhöfer Blue Phantom scanning system used for the acquisition of the benchmarking dose profile data. Top right and bottom left) Blue Phantom setup at a linear accelerator

3.2 Machine calibration and output measurements

The linear accelerator was calibrated to determine the absolute dose per monitor unit. For the Elekta Synergy accelerator it was defined as 100 cGy per 100 MU at a reference depth, D_{ref}. Machine output factors were measured to describe dose output with increasing field size. This data form part of the source model.

All measurements were done at a SSD of 100 cm and a depth of 10 cm for field sizes 1 × 1 cm^2, 2 × 2 cm^2, 3 × 3 cm^2, 5 × 5 cm^2, 10 × 10 cm^2, 20 × 20 cm^2 and 30 × 30 cm^2. Measurements were taken in a filled water tank.

The Pinpoint (0.16 cm^3) and the CC01 (0.01 cm^3) ionization chambers were used for the field sizes up to a 10 × 10 cm^2. The CC13 (0.13 cm^3) chamber was used for field sizes 3 × 3 cm^2 to 30 × 30 cm^2. All of the measurements were compared to one another.

3.3 Graphical User Interface

A graphical user interface (GUI) is used to adjust the parameters for the source to fit field profile data. It adjusts fluence intensities from the target to the exit plane by tweaking the fitting parameters of the equations discussed in Chapter 2. It can display 2-D plots and a 3-D map of the resulting fluence. This acts as a guide to adjust the exit fluence of the source model so that a DOSXYZnrc input file can be produced that would yield dose results that compares to water tank data. The main features of the source GUI is shown in Figure 3-2 and Figure 3-3.

Dose values from film, XiO® treatment planning system (TPS) [1] or a Monte Carlo simulation can be displayed and compared with one another. Isodose lines can be displayed and it is possible to normalise the dose values. Although this GUI has multiple functions that are undeniably useful, this study only utilizes the source model development part as shown in Figure 3-2.

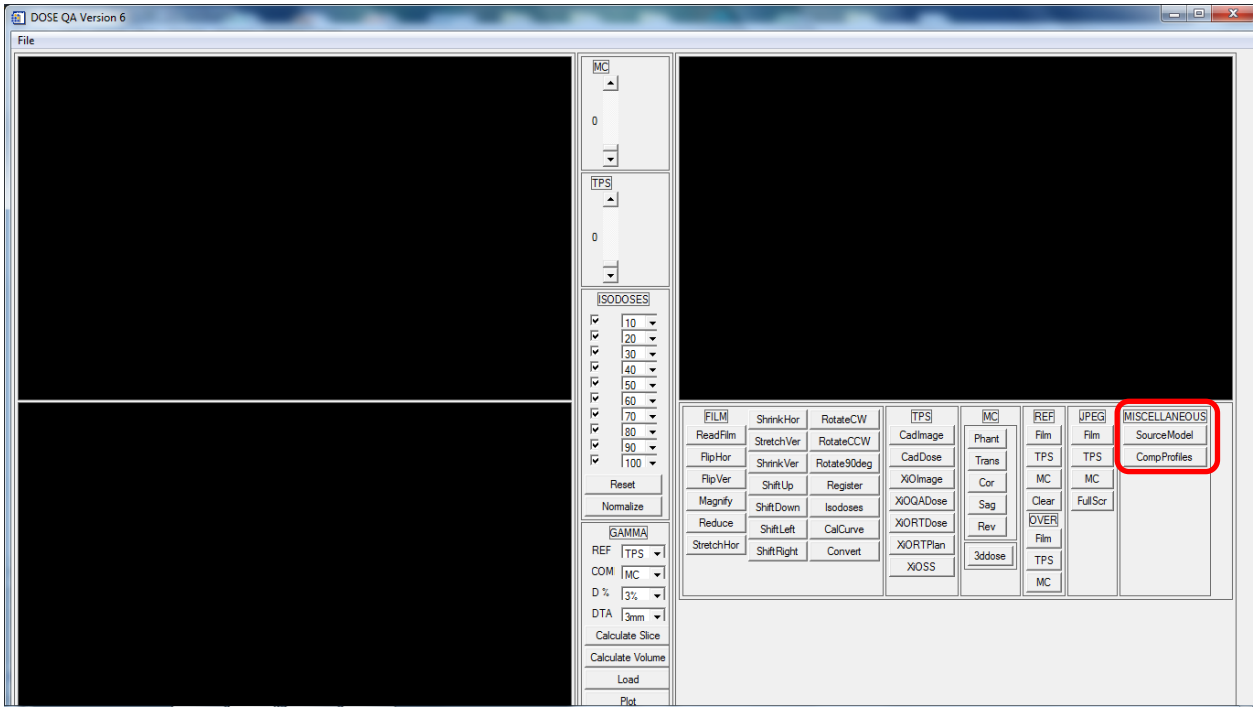

Figure 3-2: The in-house developed graphical user interface for film, treatment planning and Monte Carlo applications. The source model part is indicated with a red square.

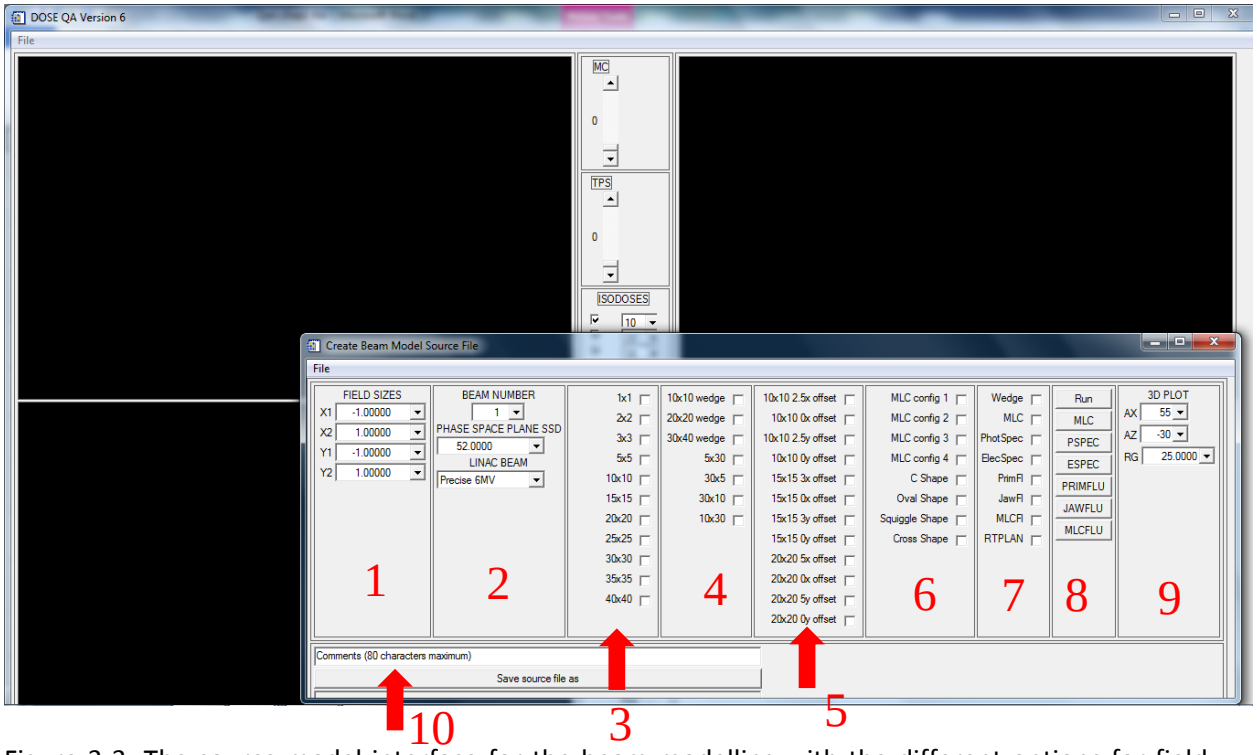

Figure 3-3: The source model interface for the beam modelling with the different options for field sizes and altering of parameters. (The columns are indicated with the red numbers)

Here follows a description of the GUI.

Column 1: Arbitrary field sizes can be chosen by adjusting the positions of the jaws. The field sizes can be set to any value that is possible on the linear accelerator.

Column 2: The 'beam number' can be used for other applications when more than one field is present in a single source file. The phase space plane SSD is the distance from the target to the plane where the source file is generated. A source model can be generated for different linacs each with their own parameters. The linac used for the generation of a source model input file can be chosen under the 'linac beam' tab e.g. Precise 15 MV.

Column 3 - 6: To make the GUI more user friendly and efficient it is possible to select a routine for each field size that already includes all the different parameter values. This is especially useful if multiple source model input files are generated. The routines include the jaw positions, MLC positions, parameter values for the fluence as well as the values for the determination of the photon energy spectrum.

Column 7: This column consists of tick boxes that will turn different features 'on' or 'off' like for instance the presence of a wedge in the field. A file can be generated without the presence of the MLC's if the user wants to use the jaw fluence only. The remainder of tick boxes are used for the display purposes of graphs and plots.

Column 8: The 'run' button will initiate the IDL program that produces the input file for DOSXYZnrc. The other buttons can be used to select the different parameters and also the positions of the different MLC's as seen below in Figure 3-4.

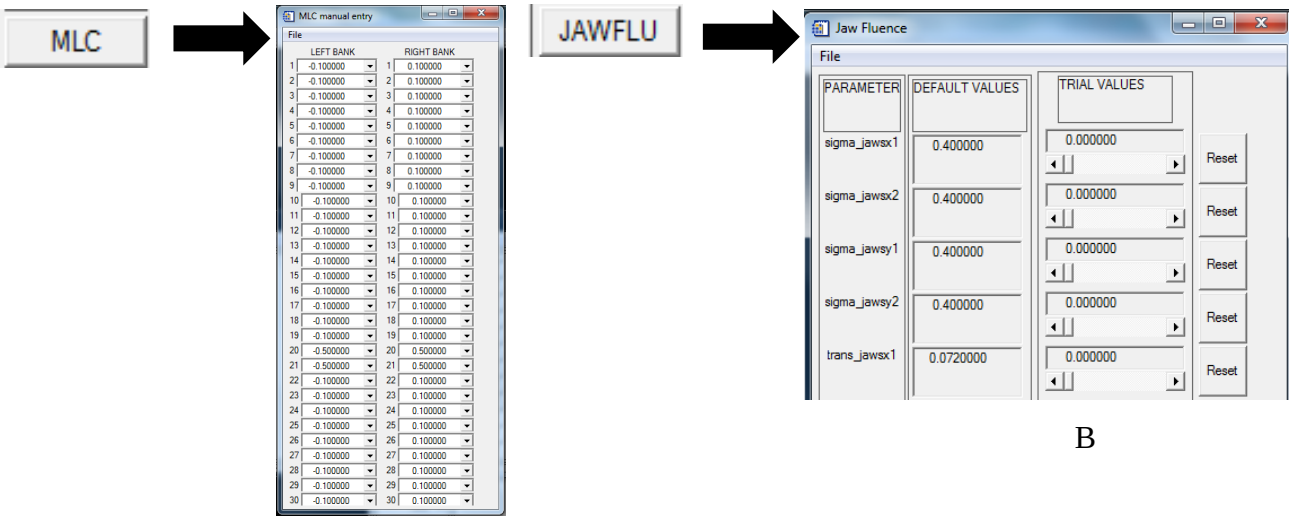

Figure 3-4: A) The manual selection of the MLC positions for the first 30 left and right MLC's respectively. B) The selection of the values for some of the parameters that determine the jaw fluence.

Column 9: 3-D plots can be rotated around the two different axes. AX rotates the plot around the x-axis and AZ rotates the plot around the z-axis. The value RG sets the maximum range of the axis.

3.4 Film calibration for in-phantom dose measurements

Film calibration must be accurate for dose comparison. Several strips of film are exposed to known radiation doses starting from zero cGy. All film pieces must be from the same Lot since variations can exists between different batches. The film is cut into equal pieces and irradiated with a 10 × 10 cm^2 field size at a specific depth in a solid water phantom.

The pieces were kept in a dark envelope after exposure to protect the film against external elements such as sunlight or humidity. An Epson Perfection V330 Photo flatbed scanner was used to read film density data. Exposed film was scanned after 24 hours to account for post irradiation growth due to polymerization. The film pieces were scanned in the same orientation to exclude orientation dependencies [23]. All the image adjustment corrections were turned off on the scanner software as shown in Figure 3-5.

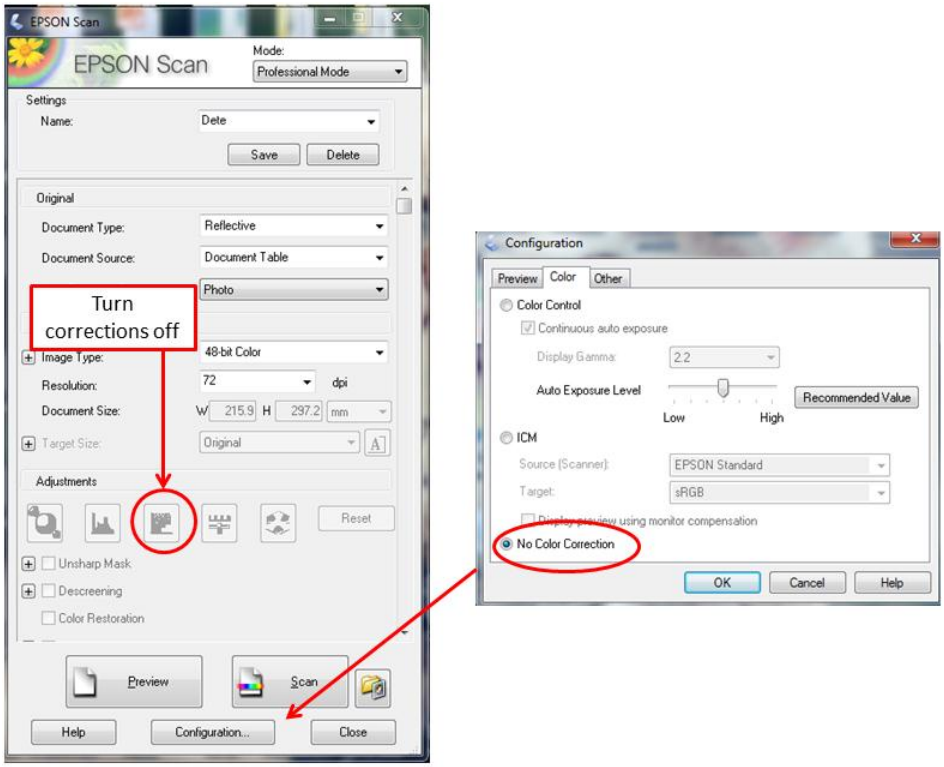

Figure 3-5: The Epson Scan interface with all the colour correction options turned off.

The resolution was set at 72 dpi in the 48-bit colour depth (RGB) mode. Data were saved in uncompressed tagged image file format TIFF. The red colour channel was used for film calibration since it is most sensitive to radiation exposure.

The pixel values of the film were read out by using the program ImageJ as shown in Figure 3-6.

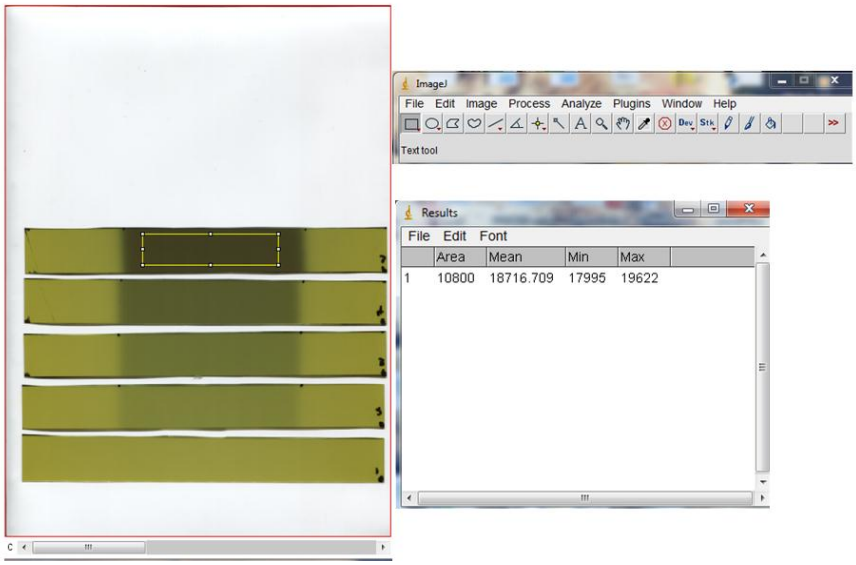

Figure 3-6: The ImageJ program was used to obtain pixel values for the red channel of the film strips.

The pixel values were converted to density values with Equation 2-33 of Chapter 2. The film pieces were calibrated with Equation 2-34 that is explained in Chapter 2.

The Excel add-in Solver was used to obtain the values for the constants *a*,*b* and *c* in Equation 2-34 of Chapter 2. Once the constants were obtained an in-house developed program in MATLAB was used to convert pixel values to dose values. The GUI was then used to display the dose values from the film and the MC simulations for dose comparisons to test the source model in clinical applications.

3.5 The beam modelling process

Photon fluence can be altered by various components as discussed in the previous chapter. Each of these components has model parameters that can be varied to ensure the model fit the linear accelerator water tank data. The first step is to get the correct primary fluence as altered by the target, flattening filter and primary collimator. The parameters of these components will stay invariant since it is not field specific but linear accelerator specific.

The largest field size, 40 × 40 cm^2, was used to determine the σ value for the target fluence. Large fields extend far beyond the CAX and "horn" effects are seen at the periphery of large field sizes. The shape of the flattening filter in the treatment head is causing this as seen in Figure 3-7. In the source model these "horns" can be eliminated by choosing the correct σ value for the target fluence. This value can be obtained by setting up a look-up table of measured vs. MC dose compared at a depth of 1 cm using the least-square value as an indicator for the best σ.

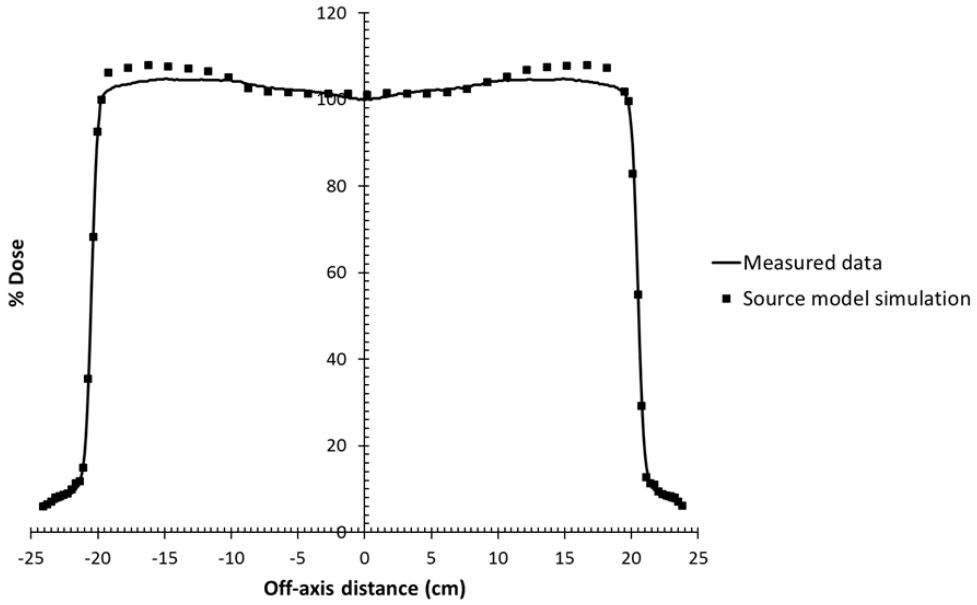

Figure 3-7: A comparison of dose profiles at 1 cm depth for a 40 × 40 cm^2 field size for an Elekta Synergy linear accelerator and simulated MC data. For this case, the dose is overestimated by the simulation and 'horns' are visible on the periphery of the field size.

In Equation 2-10 from Chapter 2, it is evident that a large σ value will cause the overestimation seen in Figure 3-7.

$$\phi_t = P\exp\left(\frac{-x^2}{\sigma^2}\right) \tag{2-10}$$

In principle the correct σ value will not influence the target fluence at smaller field sizes. With the primary fluence intact the modelling of the jaws and MLC's can begin for the different field sizes.

The σ value for the jaws varies according to the field size and is used to fit the beam penumbra for each independent jaw. By comparing the fluence obtained from the GUI with that of the water tank data at 1.5 cm depth, the correct σ value can be determined for each field size.

The effect of the MLC's on the field size differs from that of the jaws. The σ value in the y- direction (crossline) has an effect on the penumbra as seen in Figure 3-8. There is an increase in the transmission outside the field as well as at the periphery of the field.

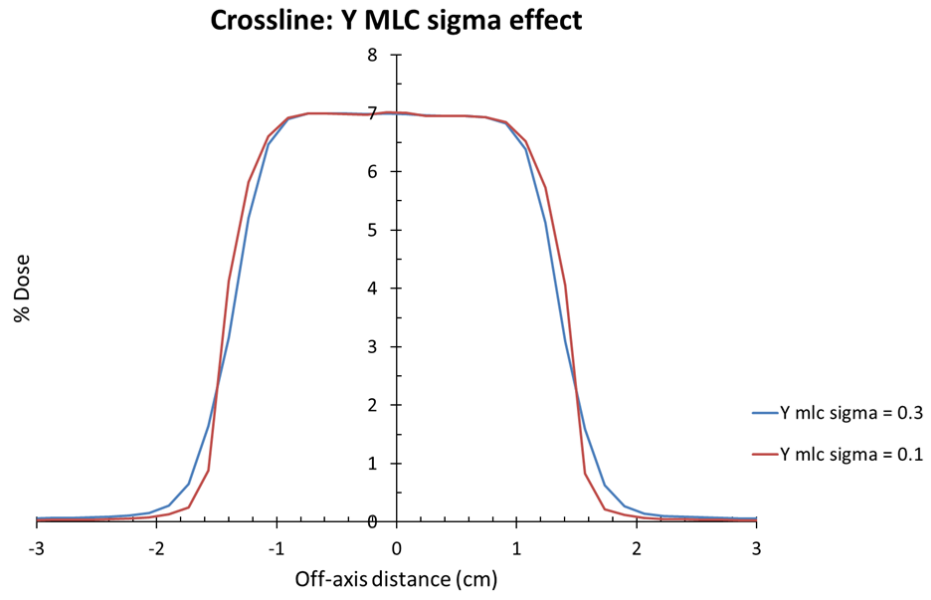

Figure 3-8: The effect of the y sigma value in the crossline direction

On the other hand, the σ value in the x- direction (inline) has a less significant effect in the crossline direction as shown in Figure 3-9. There is an increase in the transmission outside the field as well as at the periphery of the field.

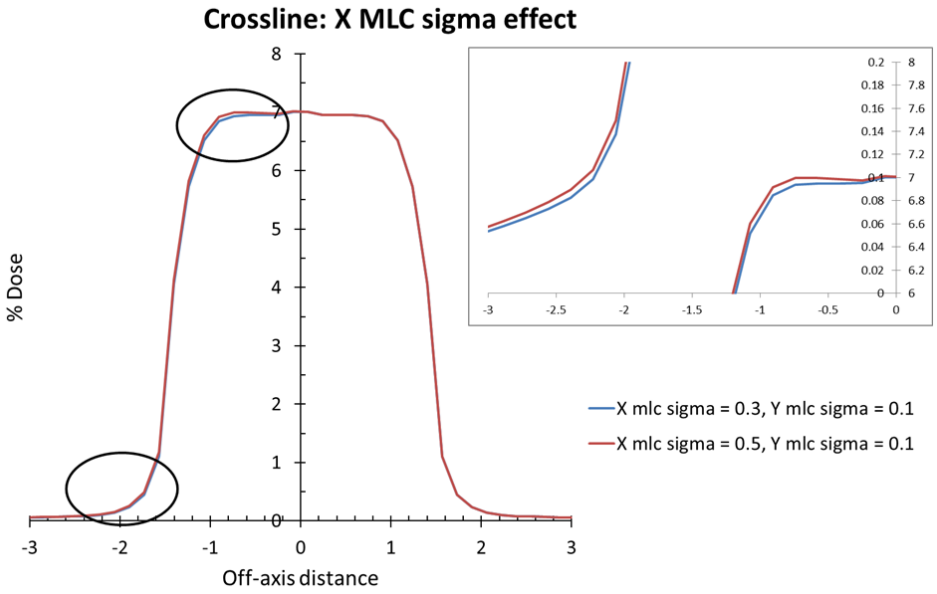

Figure 3-9: The effect of the x sigma value in the crossline direction.

The σ values for the MLC's were kept constant for the different field sizes to improve the simplicity of the source model. This means that the MLC penumbra was set at a constant value. It is evident that a small change in the σ value has an impact in both directions. The rounded leaf tips of the Synergy linac is allowing for a virtual constant leaf tip penumbra, independent of field size. The source model was tweaked to improve conformity with water tank data.

After source model parameters were decided on for a field size, the input file was created for a MC simulation on the DOSXYZnrc code. A default value for the photon energy spectrum was used for the first trial and was altered after comparison of depth dose data for MC and water tank data.

The IDL based GUI produces a source model input file for DOSXYZnrc to simulate dose distributions. This source file includes information regarding the energy spectrum and the fluence distribution as determined from parameter adjustments for the fields. Another file is produced by the GUI that includes the values of all the different parameters and can be used to keep record of each field size.

The MC simulations were run on Intel Xeon, dual quad core, 2.33 GHz processors. The amount of histories was divided between the eight cores to improve efficiency. For each simulation, different random seed numbers were used and enough histories were simulated to ensure the level of variance is below 1% in the useful part of the field.

The following transport parameters were defined for the simulations: *PCUT = 10 keV = AP* and *ECUT = 700 keV = AE*.

The *PCUT* and *ECUT* values define the global cut-off energy for photon and electron transport respectively. The *AP* and *AE* values are the low-energy threshold values for secondary bremsstrahlung photon production and knock-on electrons, respectively. All the simulations were performed in a water phantom with customized voxel sizes for adequate resolution. Smaller voxels were used in the penumbra area and larger voxels in the uniform part of large field sizes.

3.5.1 Analysis of the results

The dose distributions were analysed using the programs MCSHOW and STATDOSE [4]. MCSHOW can show dose distributions in three dimensions at different depths in a phantom. A window of MCSHOW is shown below in Figure 3-10.

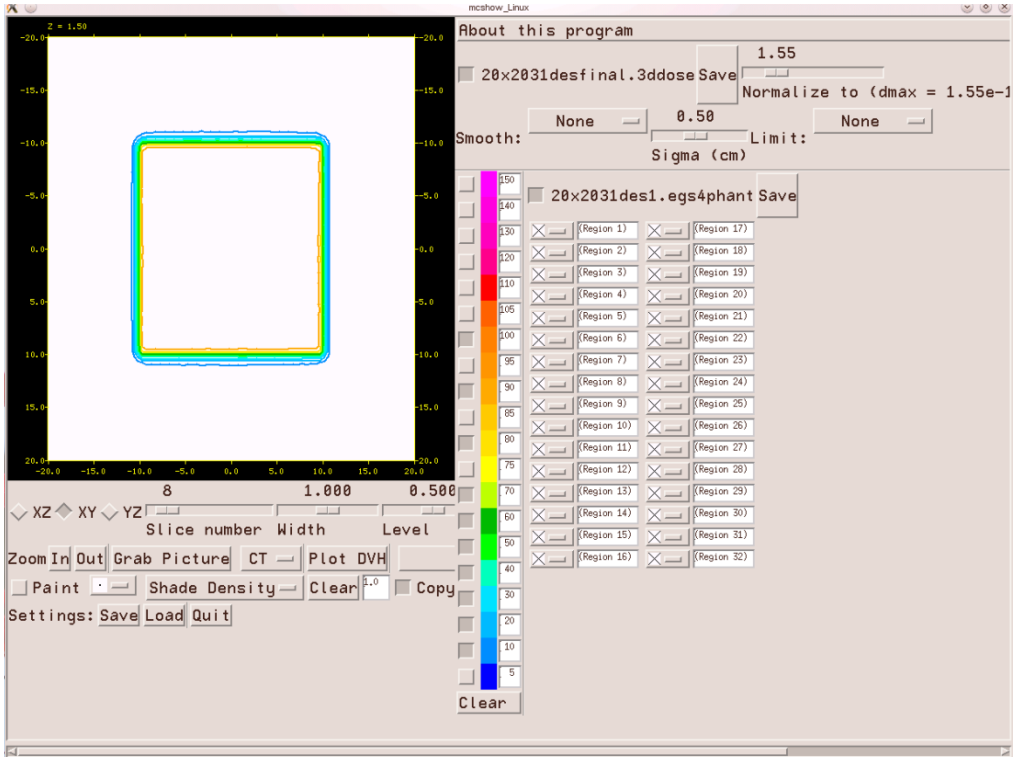

Figure 3-10: A window pane of MCSHOW

The STATDOSE code is part of the BEAM code system for MC simulation and was developed at the National Research Council of Canada [4].

It is an interactive program for 3-dimensional dose analysis and plotting 1-dimensional dose distributions. All the profiles and percentage depth dose (PDD) data were extracted for analysis with this program.

The simulated data was compared with benchmarked water tank data and analysed with a gamma criteria of 2% or 2 mm. This process of source modelling was repeated for all the field sizes until acceptable correspondence between MC and water tank data were obtained.

The gamma function was designed in IDL to perform 2-D gamma analysis of two vector pairs of data points. This evaluates the distance to agreement and the difference in dose and report the gamma index value.

3.5.2 Regular fields

Regular fields can range from a 1 × 1 cm^2 up to 40 × 40 cm^2. The jaws are equidistant from the isocenter e.g. X_1 = -5cm, X_2 = 5cm ,Y_1 = -5cm and Y_2 = 5cm for a 10 × 10 cm^2 field. A surface plot of the total fluence for a 20 × 20 cm^2 field, as displayed by the GUI, can be seen in Figure 3-11 below. Sigma and transmission values are determined for each regular field size as well as the maximum electron energy that is appropriate for the specific PDD. Figure 3-12 is an example of a MC simulation where the maximum electron energy is too low in comparison with the measured data and in Figure 3-13 the σ value for the jaws is too small.

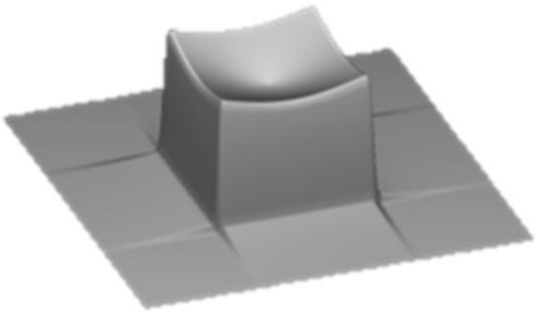

Figure 3-11: The fluence for a 20 × 20 cm^2 field. The truncation effect of the jaws as well as the transmission underneath the jaws can be seen. The effect of the flattening filter with radial distance is evident as in decreases outwards.

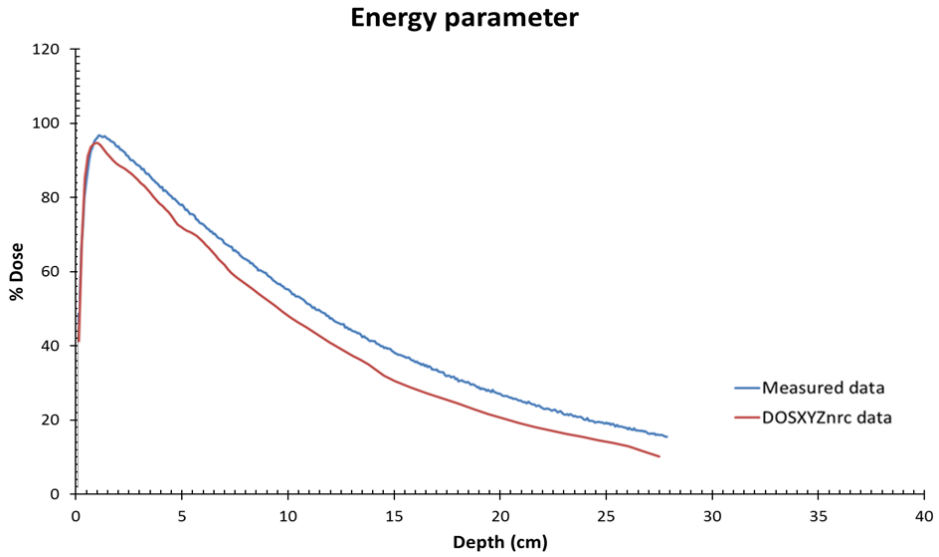

Figure 3-12: The 10 × 10 cm^2 field's PDD is not corresponding to the measured PDD. The MC simulation underestimates the dose and the source model's maximum electron energy needs to be increased.

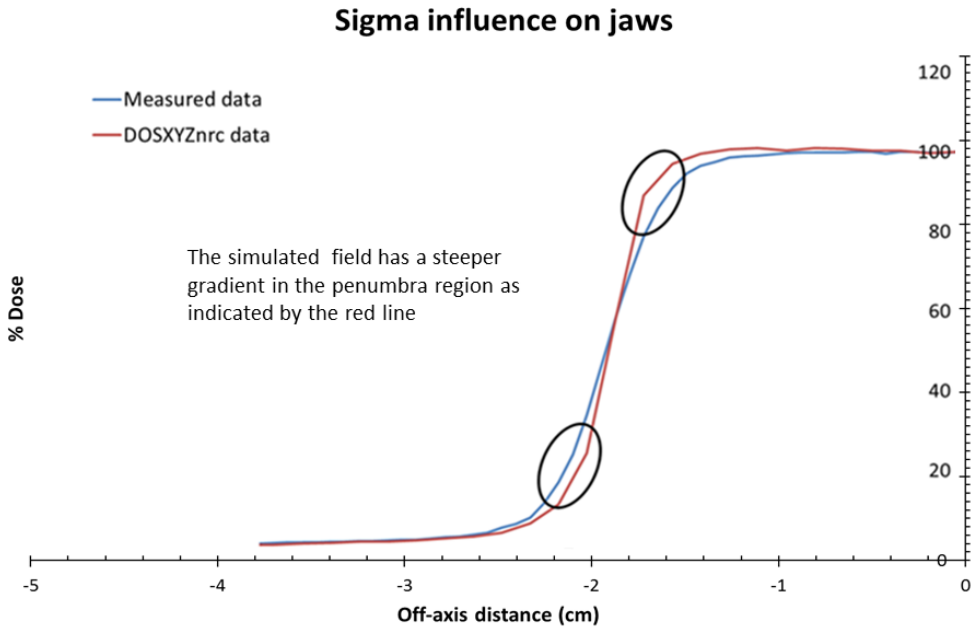

Figure 3-13: A crossline profile of a 5 × 5 cm^2 field with sigma values for the jaws that are too small. By increasing the sigma value, the slope of the penumbra will be less steep and a better fit will be achieved.

3.5.3 Off-set fields

It is possible to model a field that is not centred on the isocenter e.g. X_1 = 0 cm, X_2 = 10 cm, Y_1 = -5 cm and Y_2 = 5cm. These offset field apertures can range up to a 20 × 20 cm^2 where the field starts of with one corner on the CAX. The following fields were simulated and compared to measured data: 10 × 10 cm^2 field with a 10 cm and 2.5 cm offset, 15 × 15 cm^2 field with a 15 cm and 4.5 cm offset and a 20 × 20 cm^2 field with a 20 cm and 5 cm offset. These fields can be seen graphically in Figure 3-14 A - C. The regular field size parameter values were used for the off-set fields. It is possible that some small deviations can occur due to set-up errors during the acquisition of the water tank scans. The total fluence for an off-set field of 15; 0 x 5; 15 cm^2 is shown in Figure 3-15.

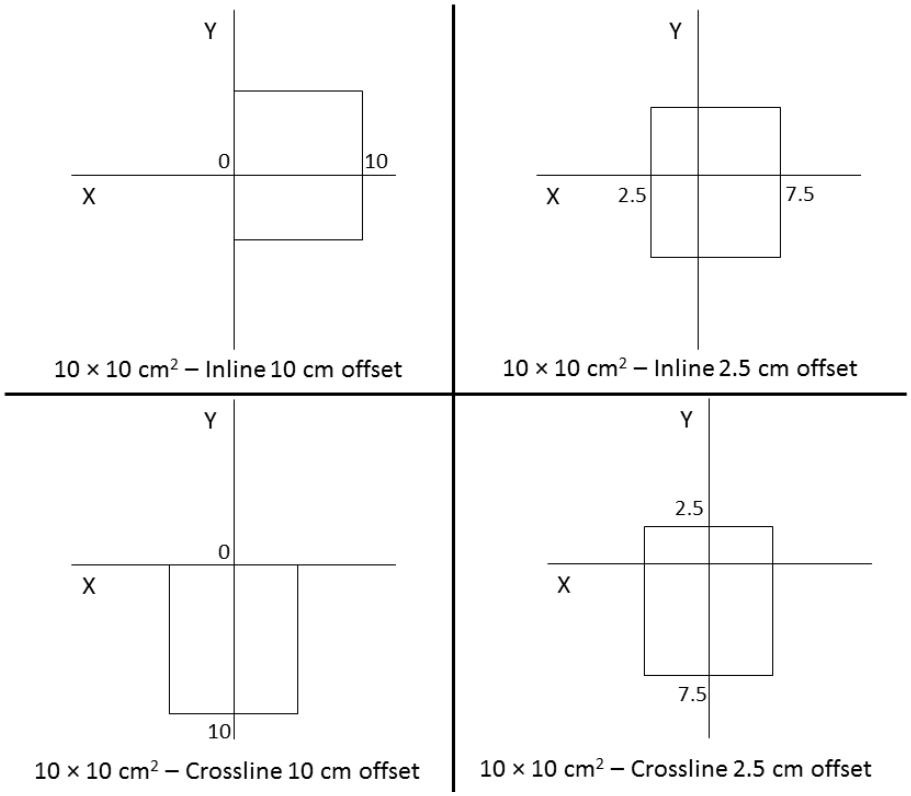
Y
0
10
X
10 × 10 cm² – Inline 10 cm offset
Y
X
2.5
7.5
10 × 10 cm² – Inline 2.5 cm offset
Y
0
X
10
10 × 10 cm² – Crossline 10 cm offset
Y
2.5
X
7.5
10 × 10 cm² – Crossline 2.5 cm offset

A

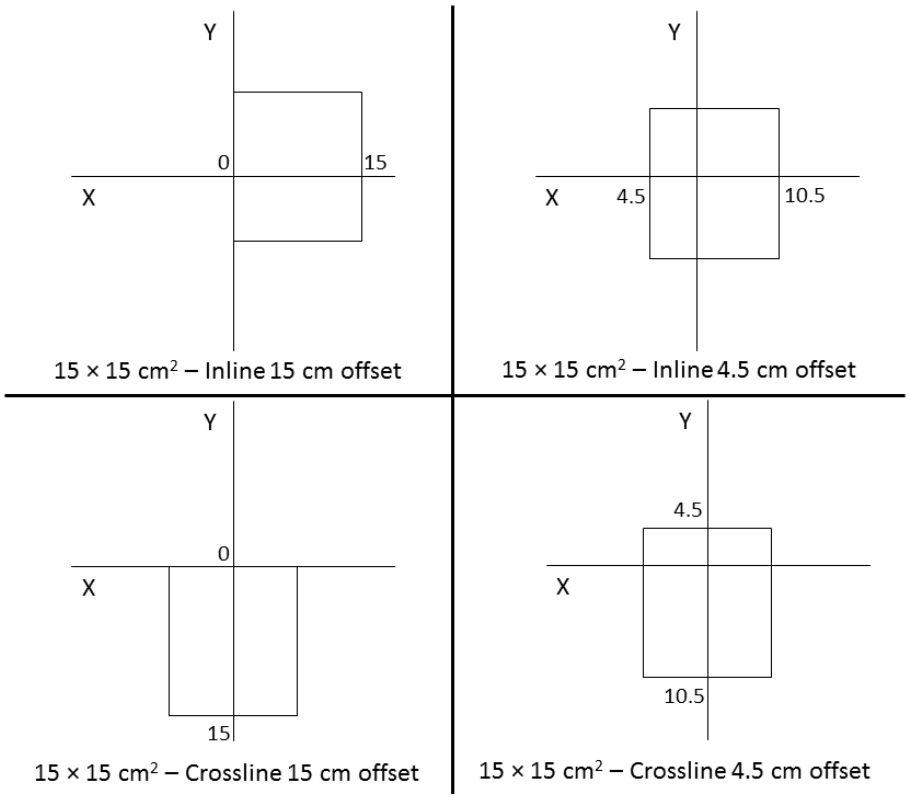
Y
0
15
X
15 × 15 cm² – Inline 15 cm offset
Y
X
4.5
10.5
15 × 15 cm² – Inline 4.5 cm offset
Y
0
X
15
15 × 15 cm² – Crossline 15 cm offset
Y
4.5
X
10.5
15 × 15 cm² – Crossline 4.5 cm offset

B

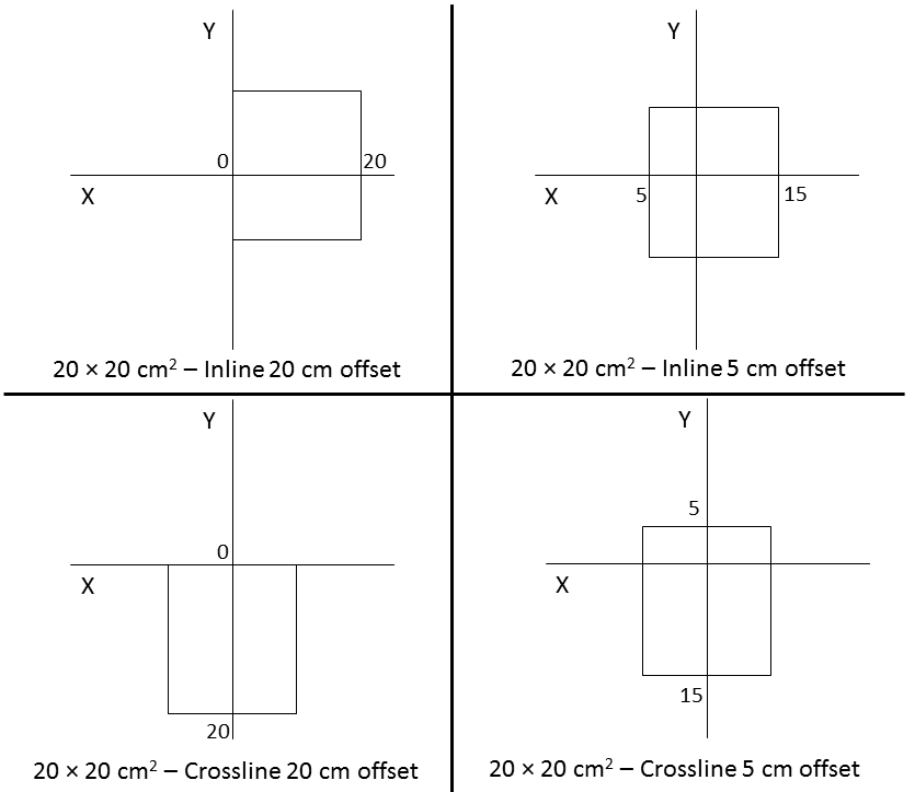

C

Figure 3-14: The different offset fields used for comparison for a A) 10 × 10 cm^2, B)15 × 15 cm^2 and a C) 20 × 20 cm^2 field respectively.

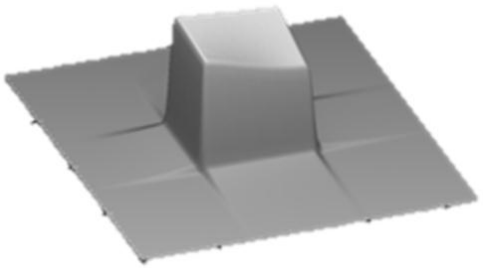

Figure 3-15: An asymmetric field with field size 15; 0 x 5; 15 cm^2.

The source model underestimated the amount of scatter in the off-set fields as seen below in Figure 3-16.

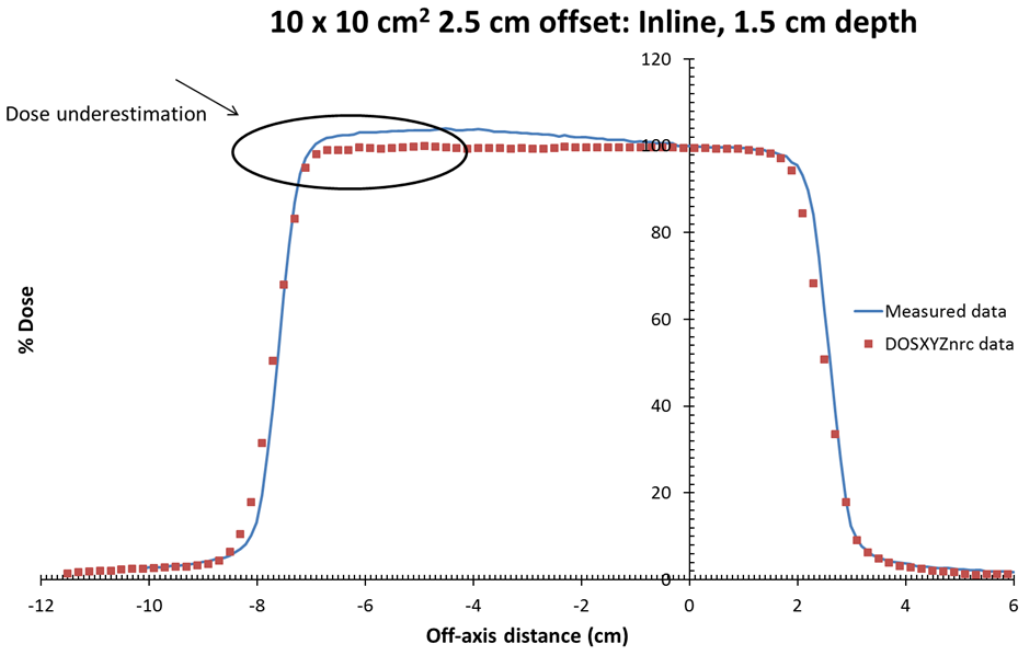

Figure 3-16: The underestimation of dose by the source model simulated with DOSXYZnrc.

This was corrected for by adding an exponential function, (*F*), to adjust the primary fluence. The following equation was used:

$$F = \exp\left(-k_1 \times d_1(x)\right) / k_2 \tag{3-1}$$

Where d_1 is a variable constant. The results will be shown and discussed in the next chapter.

3.5.4 Wedged fields

A wedge is used to alter the local gradient of the dose distribution. A wedge can be modelled in the open field by using Equation 2-24 - 2-26 as described in Chapter 2.

The fluence is modified by an exponential function to model the effect of the wedge as in Figure 3-17.

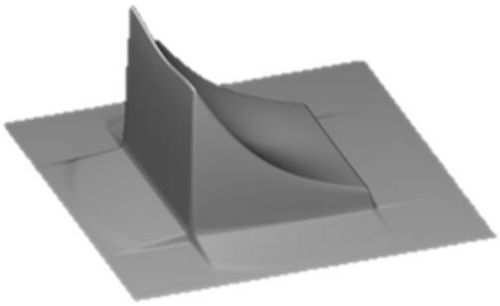

Figure 3-17: The fluence distribution for a 30 × 30 cm^2 field with a wedge inserted.

3.5.5 MLC fields

3.5.5.1 Field set-up and phantom irradiation

MLC configurations can be modelled with different source model parameters. This enables the source model to be used for more complex fields used in conformal radiation. Irregular MLC shapes from Taskgroup 53, as seen in Figure 3-19, were planned on a XiO® 4.62 TPS [1] for a phantom consisting of water. The treatment plan was transferred to the Elekta Synergy linac by using the Mosaiq software. GAFCHROMIC® EBT2 sheets (Lot No. A02011304), with dimensions 20.32 x 25.4 cm^2 were placed between water equivalent material that served as build-up and backscatter as in Figure 3-18.

The SSD was 100 cm and the film was irradiated at depths of 5 and 10 cm respectively. The MU's ranged between 327 and 358 for the different fields.

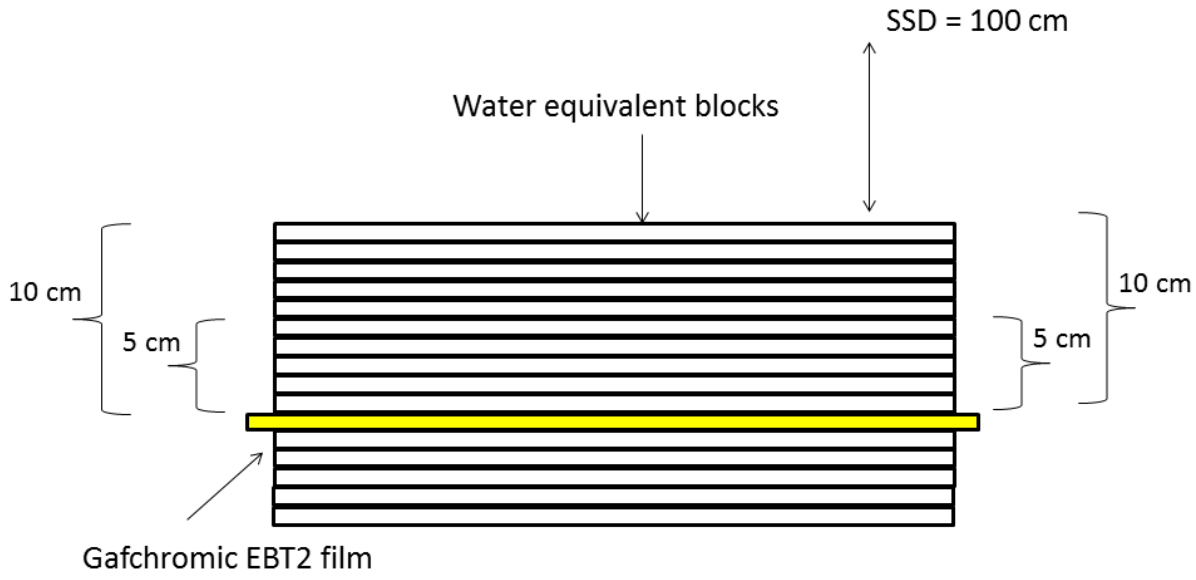

Figure 3-18: The set-up at the linac for the irradiation of the film inside the water equivalent phantom.

3.5.5.2 MC MLC set-up with the source model

An input file with the same MLC positions was generated using the GUI and simulations were performed inside a water phantom in DOSXYZnrc. The simulated doses were compared to those from the film measurements taken at the linac. The voxel sizes of the phantom were 2 mm and enough histories were run to obtain a variance below 1%.

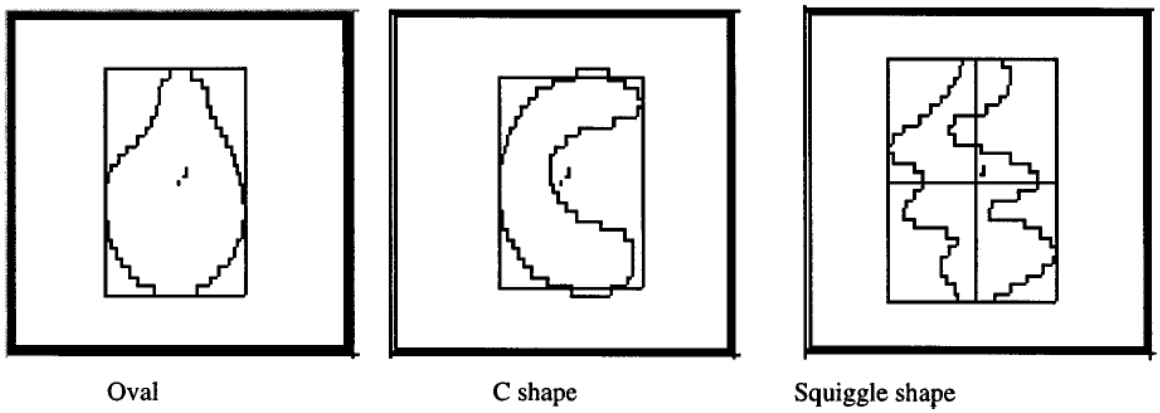

Figure 3-19: The MLC shapes to use for dose comparisons as recommended by AAPM Taskgroup 53.

The MC doses obtained from DOSXYZnrc were converted to absolute dose by using information from the XiO® TPS [1]. The following equation was used for the dose conversion:

$$Dose(cGy) = MU's \times TMR \times OF \tag{3-2}$$

Where the TMR consists of:

$$TMR = F - Factor \times \frac{PDD}{100} \times ISF \tag{3-3}$$

$$F - Factor = \left[\left(\frac{SSD + d_{\max}}{SSD + eff_{depth}} \right) \times \left(100 + \left(\frac{eff_{depth}}{100 + d_{\max}} \right) \right) \right]^2 \times \frac{PDD}{100} \times ISF \tag{3-4}$$

The F-factor represents the Mayneord factor and acts like an inverse square correction on the PDD as the SSD changes. d_{max} is the depth of dose maximum and eff_{depth} is 100 cm minus the SSD. The Percentage depth dose (PDD) and output factor (OF) data for the different fields were obtained from commissioning data.

The film was calibrated by using the procedure discussed in Section 3.4. The isodose lines from the simulations were compared with those of the film measurements.

3.6 Dose verification measurements in a RANDO® phantom

Dose verification was done using film measurements in an Anthropomorphic (RANDO®) Phantom for head-and-neck, soft tissue abdomen and chest treatment examples. The RANDO® Phantom represents a 175 cm (5'9") tall and 73.5 kg (162 lb) male figure as seen in Figure 3-20. The phantom consists of a natural human skeleton inside soft tissue-simulating material that consists of 2.5 cm thick slices in between which film can be inserted.

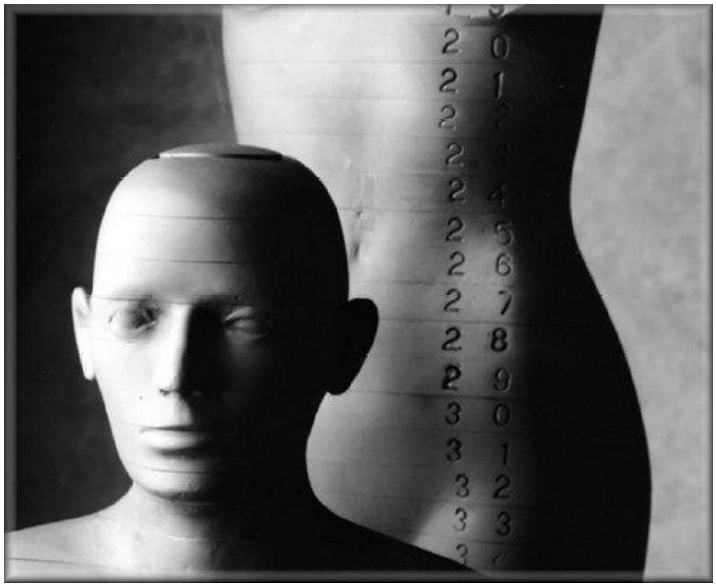

Figure 3-20: The Anthropomorphic (RANDO®) Phantom as seen on the phantom lab website (*http://www.phantomlab.com/products/rando.php*)

The phantom was scanned on a large bore Toshiba Aquillion LB CT scanner with 2 mm slice thickness. Markings were made on the phantom to ensure the position of the phantom on the bed is reproducible. Immobilization devices were used to keep the phantom in the required position on the CT and treatment couch.

3.6.1 Head –and- neck treatment

The phantom set-up for the head-and-neck treatment can be seen in Figure 3-21 below.

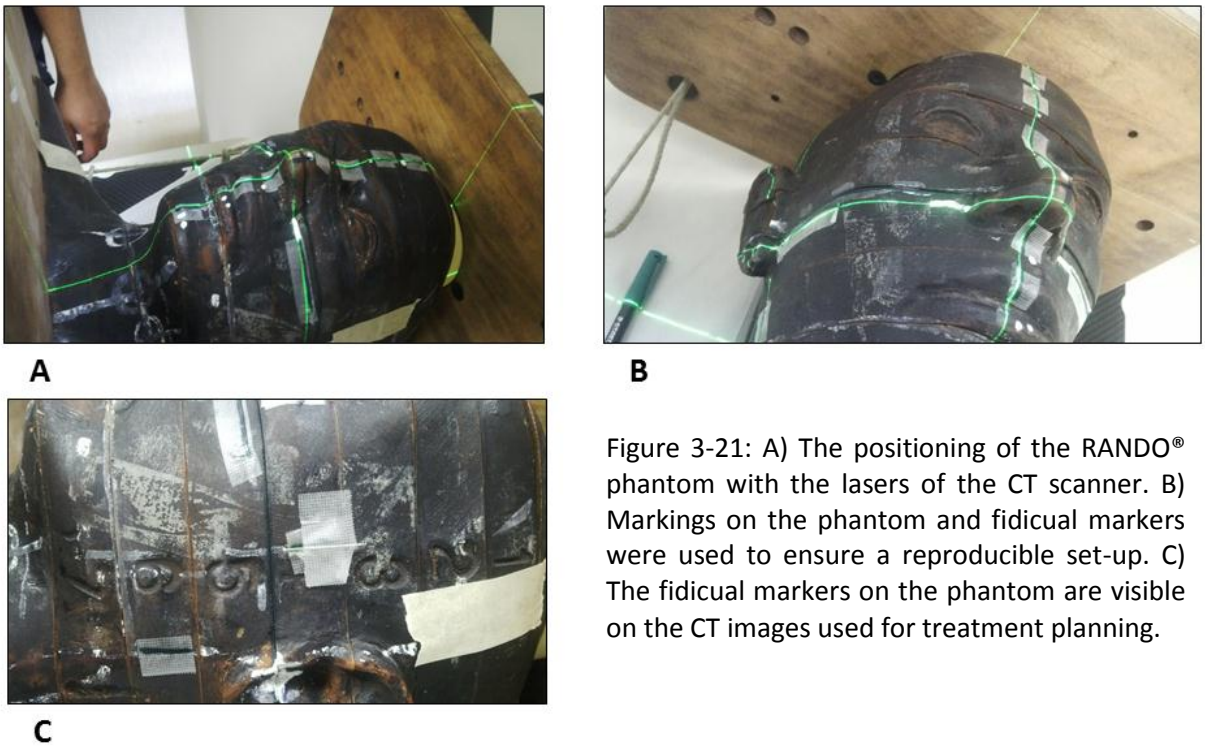

Figure 3-21: A) The positioning of the RANDO® phantom with the lasers of the CT scanner. B) Markings on the phantom and fidicual markers were used to ensure a reproducible set-up. C) The fidicual markers on the phantom are visible on the CT images used for treatment planning.

Treatment consists of two fields each with energy of 6 MV as in Figure 3-22. A 7×7 cm^2 wedged field of 427 MU's with gantry angle of 0° and a collimator angle of 90° and a 5×5 cm^2 field of 256 MU's with a gantry angle of 90° and a collimator angle of 0° resulting in a uniform dose area.

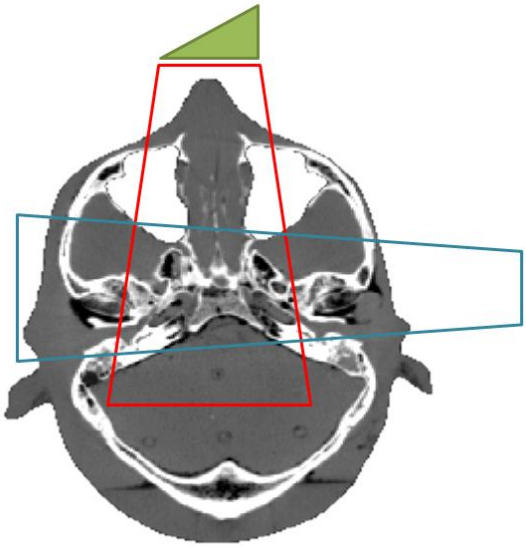

Figure 3-22: The plan set-up for the head-and-neck treatment.

3.6.2 Abdomen treatment

The phantom set-up for the abdomen treatment can be seen in Figure 3-23 below.

A B

Figure 3-23: A) The positioning of the RANDO® phantom with the lateral lasers of the CT scanner. B) Positioning of the phantom with the top laser by means of fidicual markers

The treatment plan consisted of four 5 × 5 cm^2 fields: from a gantry and collimator angle of 0°, gantry angle of 90° and collimator angle of 90° with a wedge, gantry angle of 180° and a collimator angle of 0° and a gantry angle of 270° and a collimator angle of 0°. This is seen in Figure 3-24.

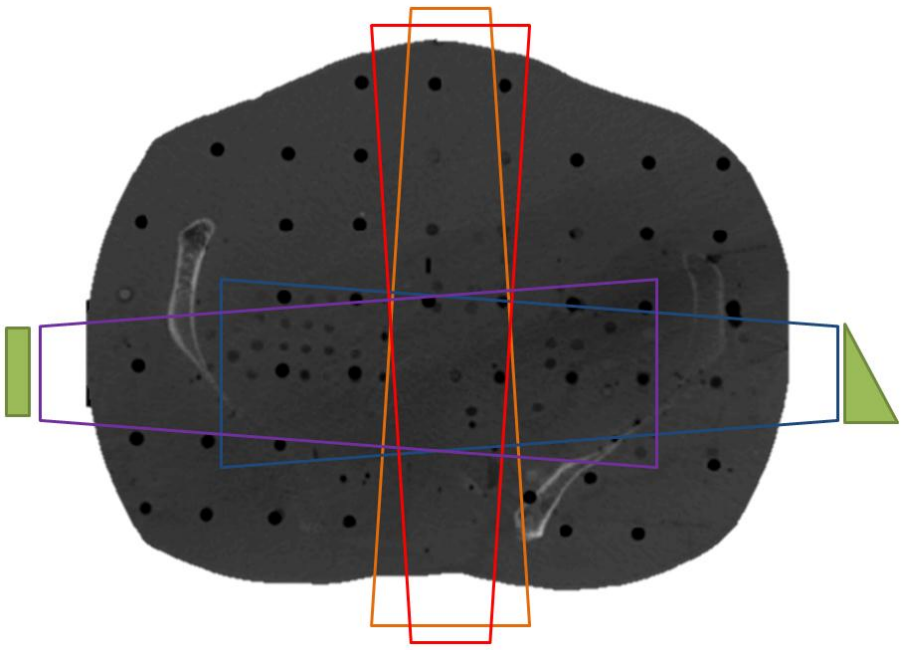

Figure 3-24: The plan set-up for the abdomen treatment.

3.6.3 Chest treatment

The phantom set-up for the chest treatment can be seen in Figure 3-25 below

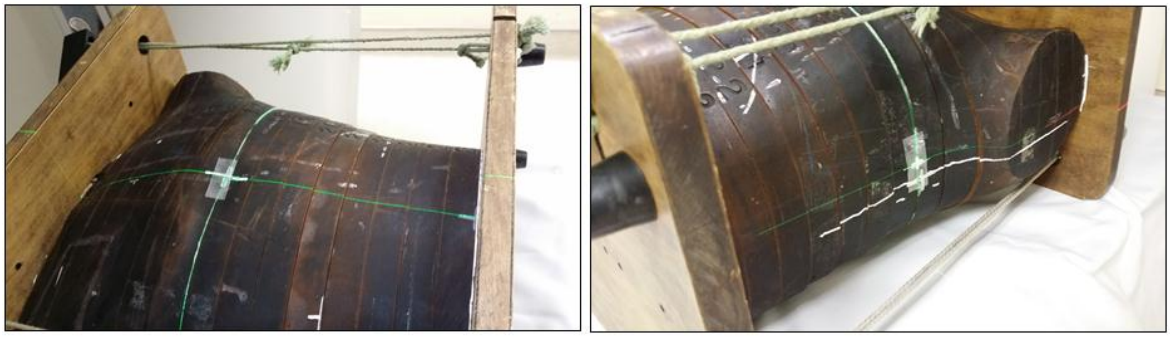

A B

Figure 3-25: A) The positioning of the RANDO® phantom with the lateral lasers of the CT scanner. B) Positioning of the phantom with the top laser by means of fidicual markers

This plan consisted of three fields: A 3 × 3 cm^2 field with a gantry and collimator angle of 0°, a 5 × 3 cm^2 field with a gantry angle of 90° and a collimator angle of 0° and 5 × 3 cm^2 field with a gantry angle of 270° and a collimator angle of 0° as shown in Figure 3-26.

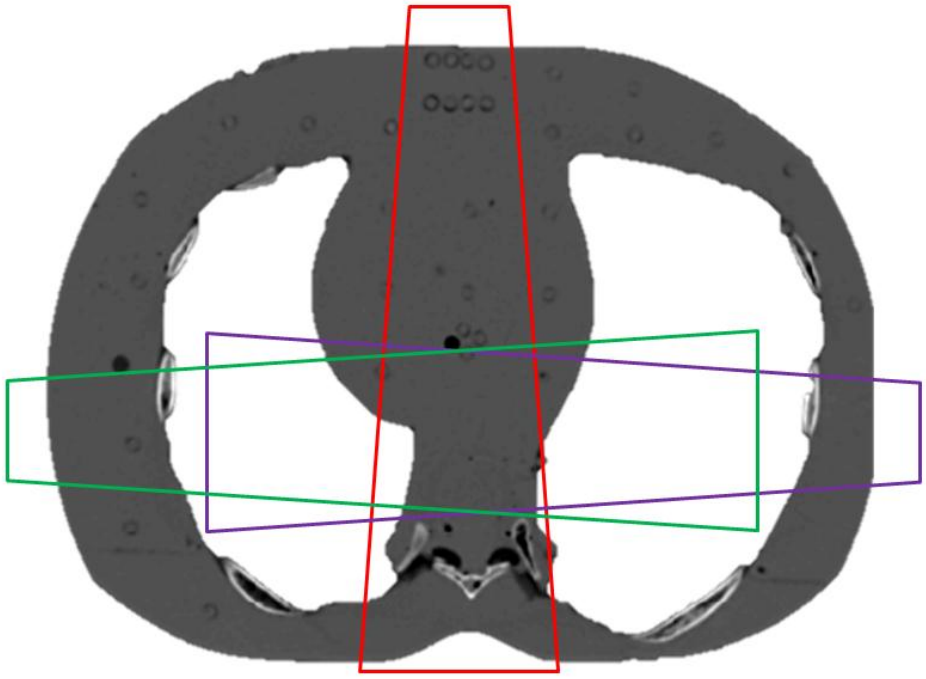

Figure 3-26: The plan set-up for the chest treatment.

All of the fields were planned on a XiO® 4.62 TPS [1] and transferred to the linac for irradiation of the phantom.

The phantom was set-up according to the markings made during the scanning process to ensure the phantom is in the right position. Film was placed inside the phantom at a specific slice and irradiated according to the different treatment plans as seen below in Figure 3-27 A-D. Figure 3-28 and Figure 3-29 show the case for the chest and abdomen treatment measurements respectively.

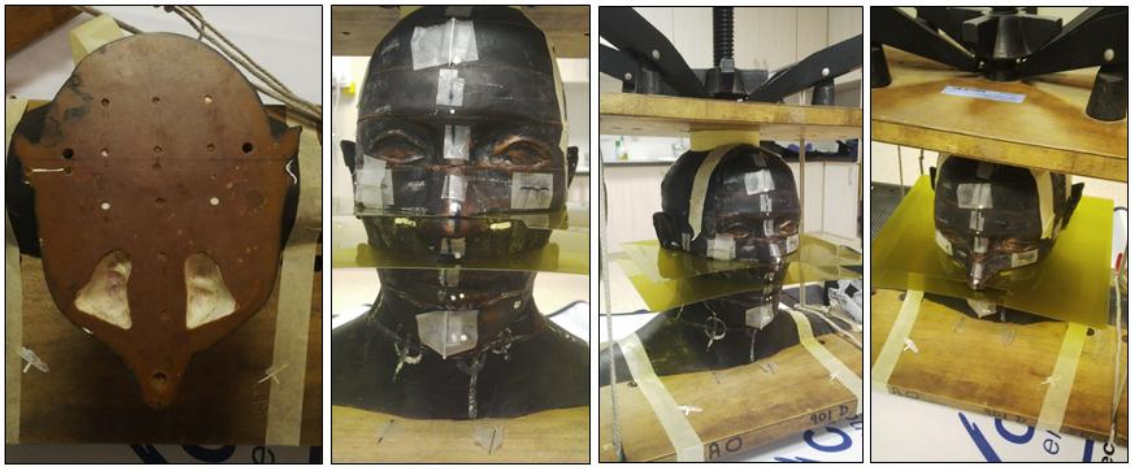

Figure 3-27: A) The inside of the slice where the film was inserted for irradiation. B-D) The RANDO®phantom with the film inserted between the different slices.

Figure 3-28: A) The RANDO® phantom with the film inserted. B) The film after irradiation of the phantom.

A B

Figure 3-29: A) The RANDO® phantom with the film inserted. B) The film after irradiation of the phantom.

The film was calibrated as discussed in Section 3.4. Filmstrips of 2.5 × 20.32 cm^2 were irradiated with a 10 × 10 cm^2 field with different doses at a depth of 5 cm. The doses received by the films were corrected for PDD to calculate the actual dose at 1.5 cm depth. Calibration doses of $D_{max}+5\%$, $D_{max}/2$, $D_{max}/4$ and $D_{max}/8$ were used for all the treatment plans. An example of the film strips are shown below in Figure 3-30.

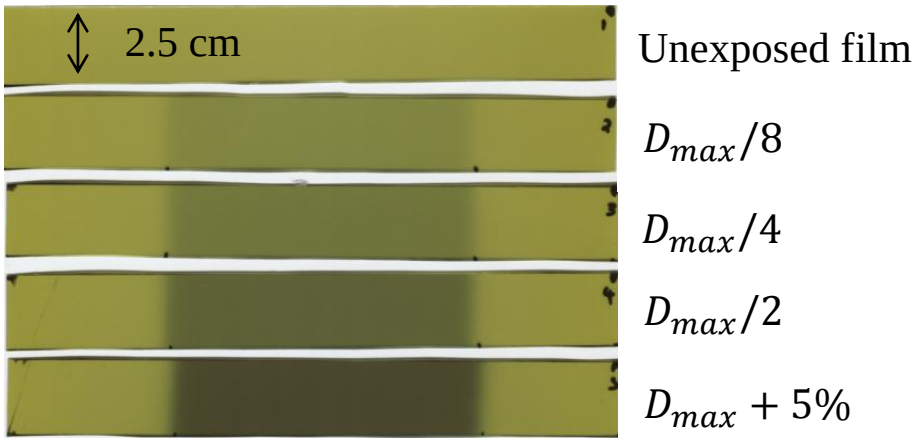

Figure 3-30: Filmstrips used for the calibration. The doses increase for the top to the bottom, starting at the unexposed filmstrip. The discolouration of the film can be seen as the dose increases.

The RANDO® phantom's CT slices were converted to a format used by the *.egsphant file of the CTCREATE code. This *.egsphant file was then used with the DOSXYZnrc code to perform simulations of the treatment plans on the RANDO® phantom's CT data.

The results were analysed using the OmniPro - ImRt software version 1.7.0021 from IBA Dosimetry. The isodose lines obtained from the film were compared to that of the MC simulation by using the GUI.

3.7 Bibliography

1. XiO® - Comprehensive RTP System - Treatment planning Software [Internet]. Elekta AB. [cited 2014 May 5]. Available from: http://www.elekta.com/healthcare-professionals/products/elekta-software/treatment-planning-software/planning-software/xio.html

2. Aldelaijan S, Mohammed H, Tomic N, Liang L-H, DeBlois F, Sarfehnia A, et al. Radiochromic film dosimetry of HDR [sup 192]Ir source radiation fields. Med Phys. 2011;38(11):6074–83.

3. Chair AN-R, Blackwell CR, Coursey BM, Gall KP, Galvin JM, McLaughlin WL, et al. Radiochromic film dosimetry: Recommendations of AAPM Radiation Therapy Committee Task Group 55. Med Phys. 1998;25(11):2093–115.

4. gjjur4356. STATDOSE for 3D dose distributions [Internet]. Docstoc.com. [cited 2014 Feb 3]. Available from: http://www.docstoc.com/docs/74978132/STATDOSE-for-3D-dose-distributions

4. CHAPTER 4: RESULTS AND DISCUSSION

4.1 Primary fluence

The primary fluence consists of the target, primary collimator and the flattening filter. The parameter values for these three components are invariant between the field sizes and are discussed below. All the equations used are discussed in Chapter 2 although some may be repeated below just for clarity.

4.1.1 Target fluence

The following equation was used to model the Gaussian function of the target fluence:

$$\phi_t = P \exp\left(\frac{-x^2}{\sigma^2}\right) \tag{2-10}$$

A default value of 10 was used for P and a least square fit procedure was used to find the optimal value for σ. High σ values resulted in horns on the periphery of the field and low σ values resulted in dose underestimation. The approximate range of the ideal σ value was determined and values ranging from 74 to 84 were used for the least square fit between the measured and simulated data. The lowest value was obtained at a target σ value of 80. For the least squares data, the measured dose was compared to the simulated dose at the same dose points over 90% of the useful field with x as the off-axis distance.

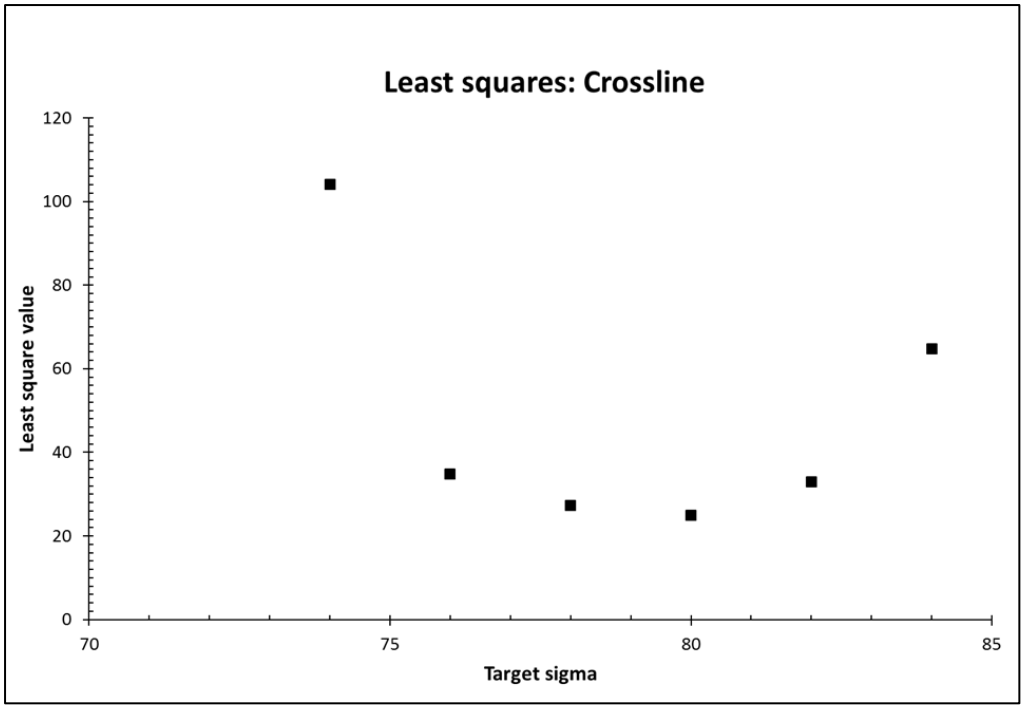

Figure 4-1: The least squares fit in the crossline direction show the lowest value at a target sigma value of 80.

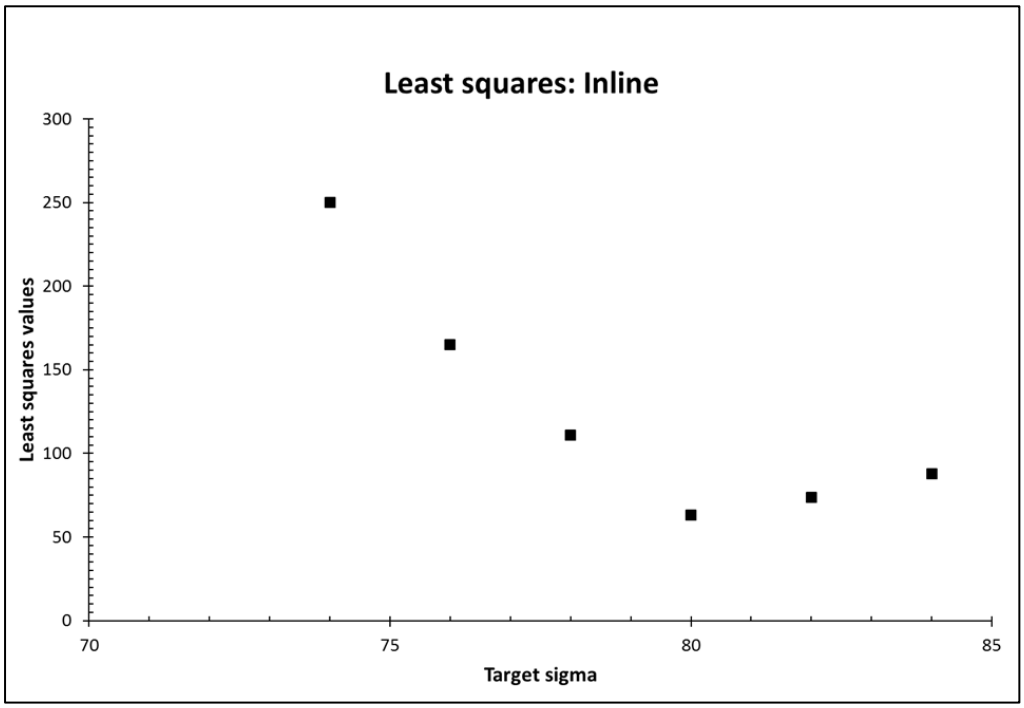

Figure 4-2: The least squares fit in the inline direction show the lowest value at a target sigma value of 80.

4.1.2 Primary collimator

The error function used for the truncation of the primary collimator and the exponential attenuation under the collimator is seen below:

$$\phi_{pc}(r) = \phi_t \, erf(X_3, \sigma) + 1[1 - erf(X_3, \sigma)] Z \exp(-\mu_1 (r - X_3)) \quad (2\text{-}11)$$

The radial distance r is the same as for the target fluence. The value of X_3 is 27.9 as this is approximately the position of the primary collimator in the linear accelerator head below the target. The σ value is 0.94, μ_1, is equal to 0.33 and the value of Z is 4.0. These parameters were found previously by fitting this function manually to a 40 × 40 cm^2 field dose profile extracted from a full Monte Carlo simulation at 1 cm depth.

4.1.3 Flattening filter

The attenuation factor of the flattening filter is given by:

$$ff_{att}(x) = \exp(-\mu_2 . t) \quad (2\text{-}13)$$

As seen above, the flattening filter also has a radial dependency (x). The value of μ_2 is 0.16 obtained from a full Monte Carlo simulation for a 40 × 40 cm^2 field case as above. Parameter t is approximated by a polynomial function as discussed in Chapter 2.

The total fluence is given by Equation 2-15 from Chapter 2 as shown in Figure 4-3.

$$\phi_{pc+ff} = \phi_{pc}(x) . ff_{att}(x) \quad (2\text{-}15)$$

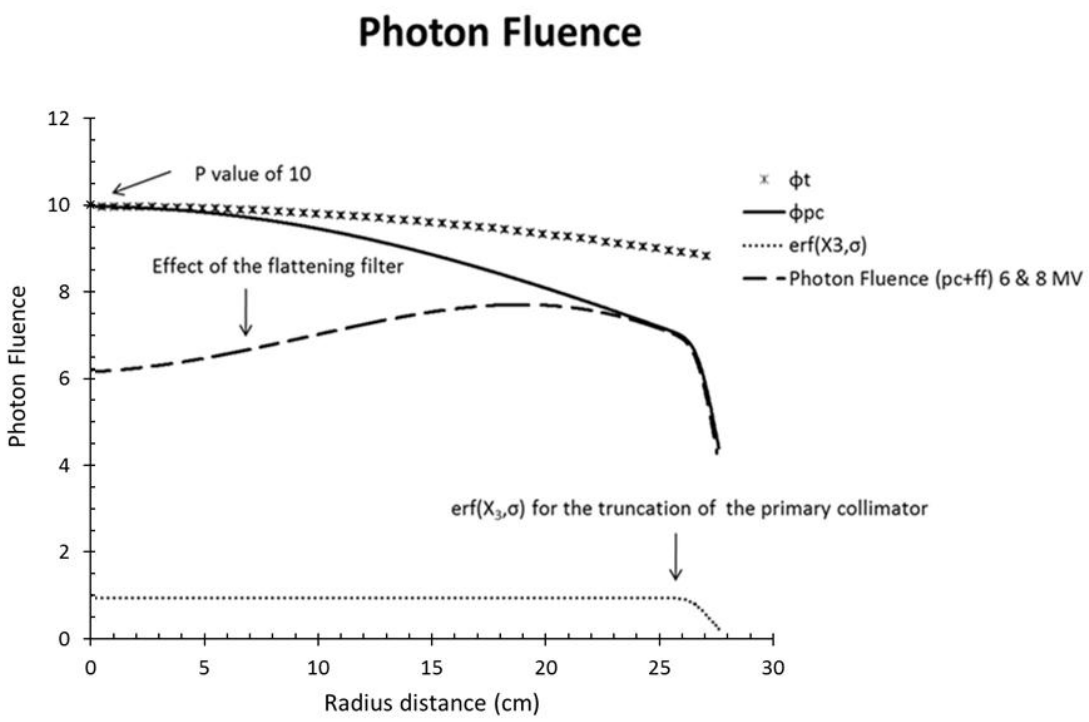

Figure 4-3: The total primary fluence consisting of the target, primary collimator and flattening filter.

The primary fluence together with the field defining jaws were used for the Monte Carlo simulation of percentage depth dose curves (PDD) and profiles for field sizes ranging from 1×1 cm^2 up to 40×40 cm^2. The results for each field size are discussed in the following section.

4.2 Regular fields

The jaws and MLC's define the field size by means of error functions and added transmission as described in Chapter 2.

The same functions were used for the MLC field collimation as applied to each individual leaf:

$$\phi_{mlc_{X_1}} = 1 - erf\left(mlc_{X_1}, \sigma_{xmlc}\right) + T \times \exp\left(-\mu_{out\_xmlc} |x - mlcx1|\right) \tag{2-20}$$

The next section includes the fitting parameter values for the fields and their respective profiles.

4.2.1 1×1 cm^2 – 5×5 cm^2 fields

The following parameters were used for the modulation of the 1×1 cm^2 to 5×5 cm^2 fields.

Table 4-1: Field parameters for field sizes 1×1 cm^2 to 5×5 cm^2. The σ- value for the MLC x and y is 0.5 and 0.3 respectively and the target σ is 80 over all the fields. The maximum electron energy is 6.8 MeV for all field sizes.

Field size	JAWS					
	X			Y		
	Position	σ	T	Position	σ	T
1x1	0.5	0.07	0	0.5	0.4	0
2x2	1	0.07	0.02	1.1	0.4	0.1
3x3	1.4	0.07	0.02	1.5	0.4	0.1
5x5	2.5	0.07	0.06	2.5	0.4	0.2

There is a definitive trend in the parameter values as seen in Figure 4-4 below and they can be interpolated. The target σ is constant between the fields in both the x- and y directions. There is a steady increase in the transmission parameter (T) over increasing field size in both directions. The maximum electron energy (MeV) stays constant.

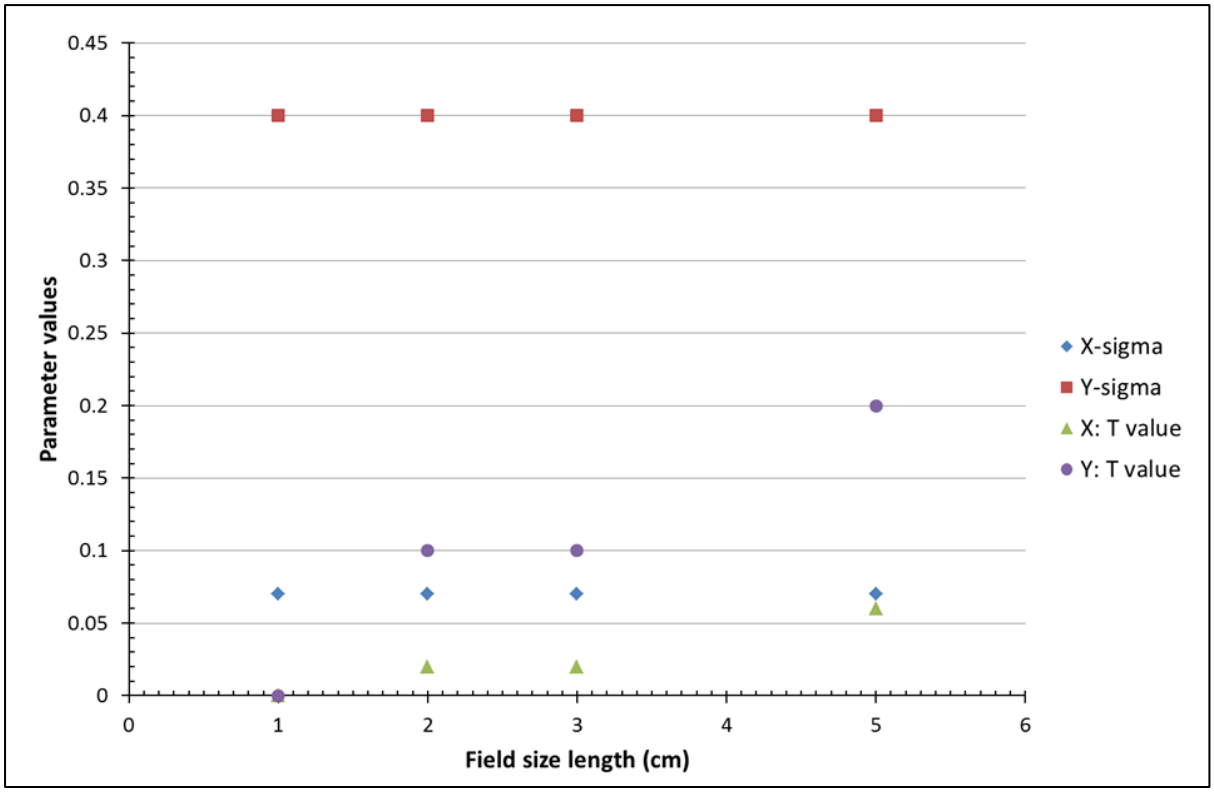

Figure 4-4: Plot of the fitted parameter values for fields from 1 × 1 cm^2 to 5 × 5 cm^2.

The MLC settings for the small fields are shown in Figure 4-5. The open and closed leaves correspond to those on the linac.

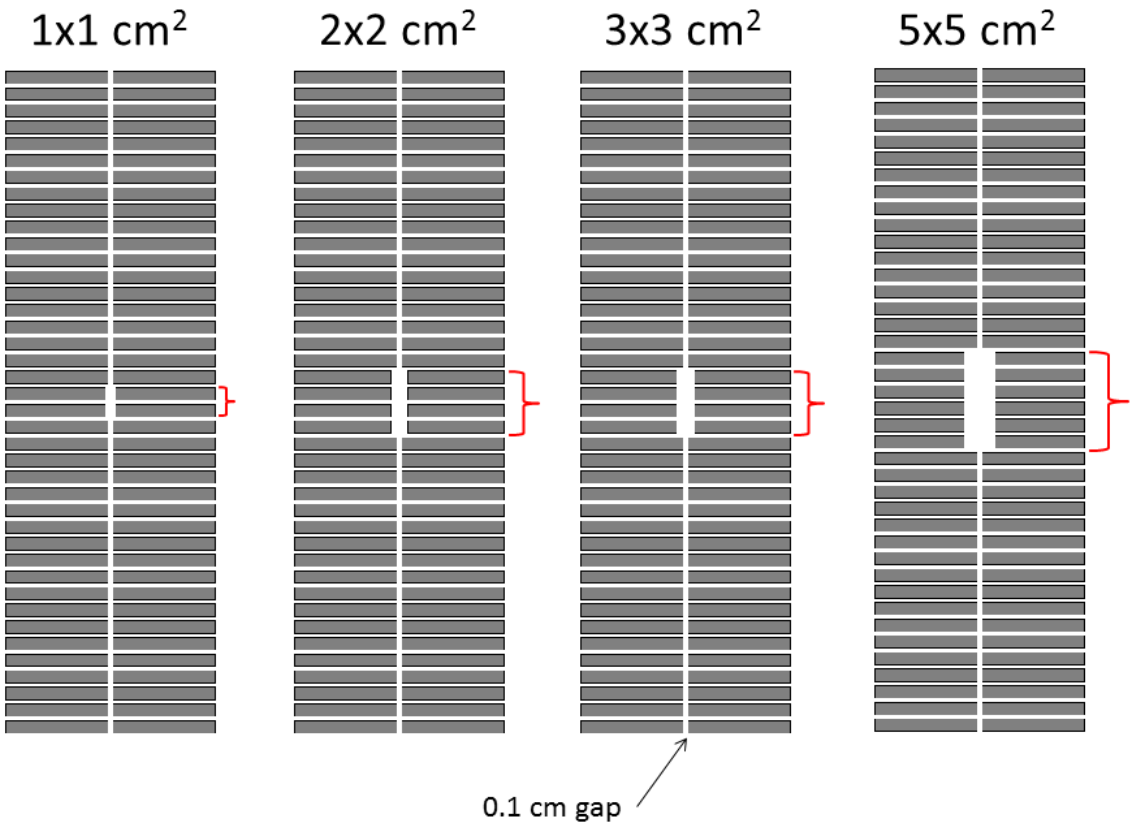

Figure 4-5: The open leaves are indicated with a red bracket and the 'closed' leaves have an interleaf gap of 0.1 cm.

The fluence obtained for the group of fields are shown in Figure 4-6 for the inline and crossline directions.

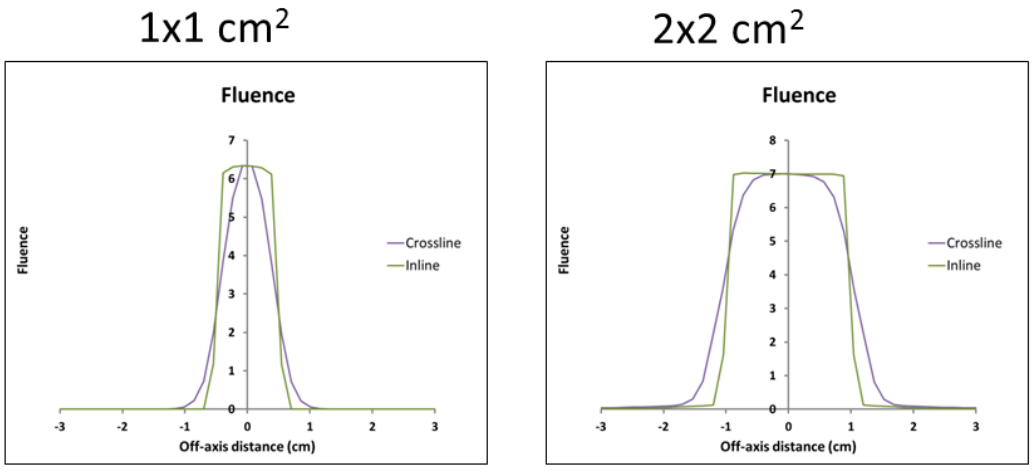

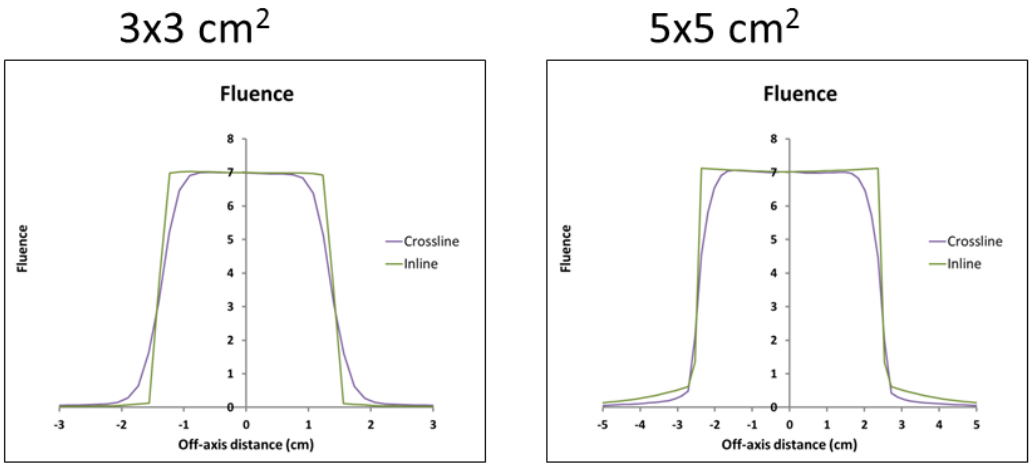

Figure 4-6: The fluence profiles obtained from the GUI for the inline and crossline directions. The crossline profile has a larger σ value and the transmission is different for the two profiles. Note: This is just the calculated source model fluence.

The crossline and inline dose profiles for field sizes 1×1 cm^2 to 5×5 cm^2 for 1.5, 10, 20 and 30 cm depths are shown in the next set of figures. The gamma index values were below 1 for all the field sizes at the different depths. The profiles are normalized to 100% on the CAX and the PDD curves are normalized to different values in order to distinguish between them.

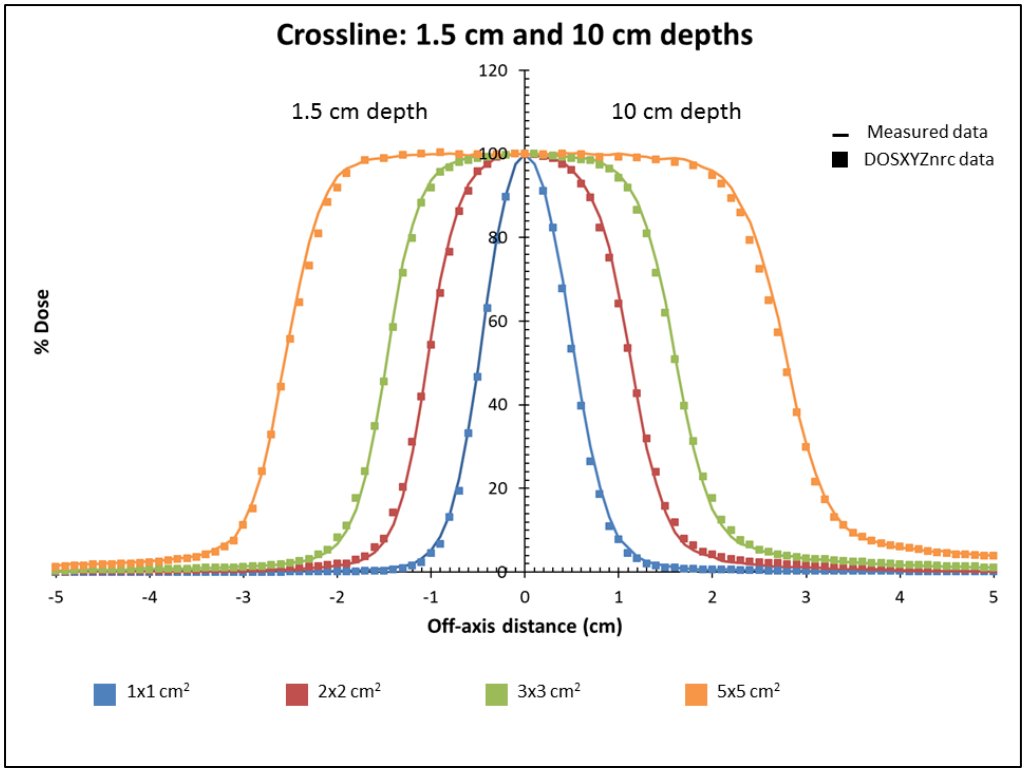

Figure 4-7: Crossline profiles for 1.5 cm and 10 cm depths for the group of small fields. Measured data (-) are compared to DOSXYZnrc data (▪).

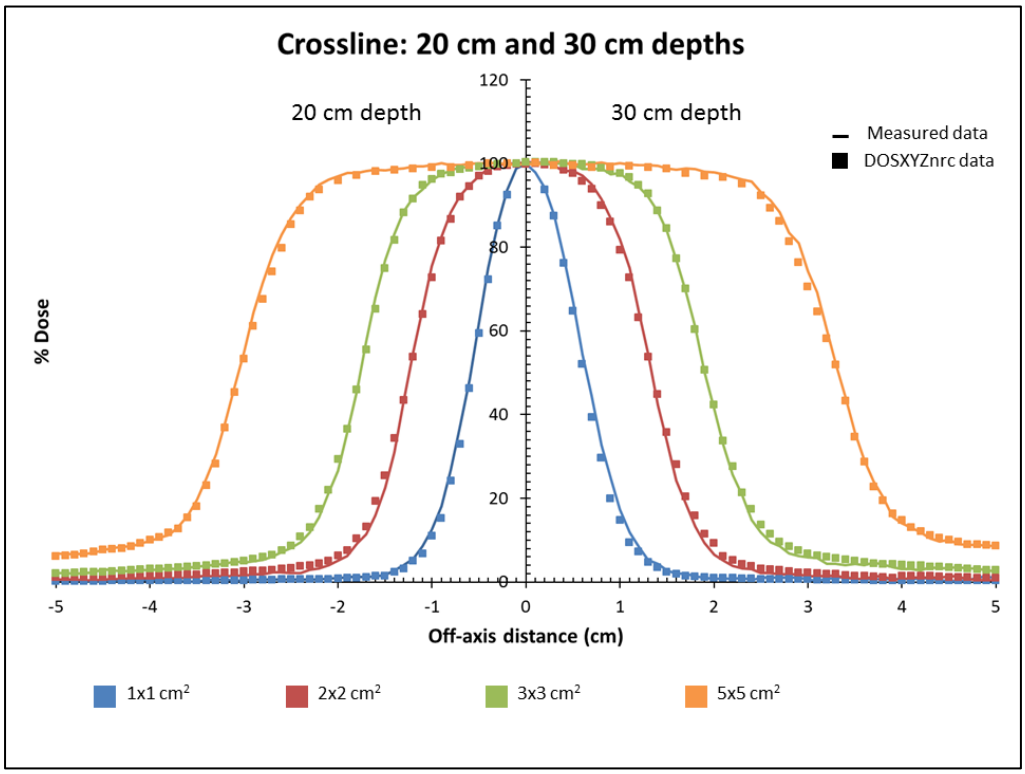

Figure 4-8: Crossline profiles for 20 cm and 30 cm depths for the group of small fields. Measured data (-) are compared to DOSXYZnrc data (▪)

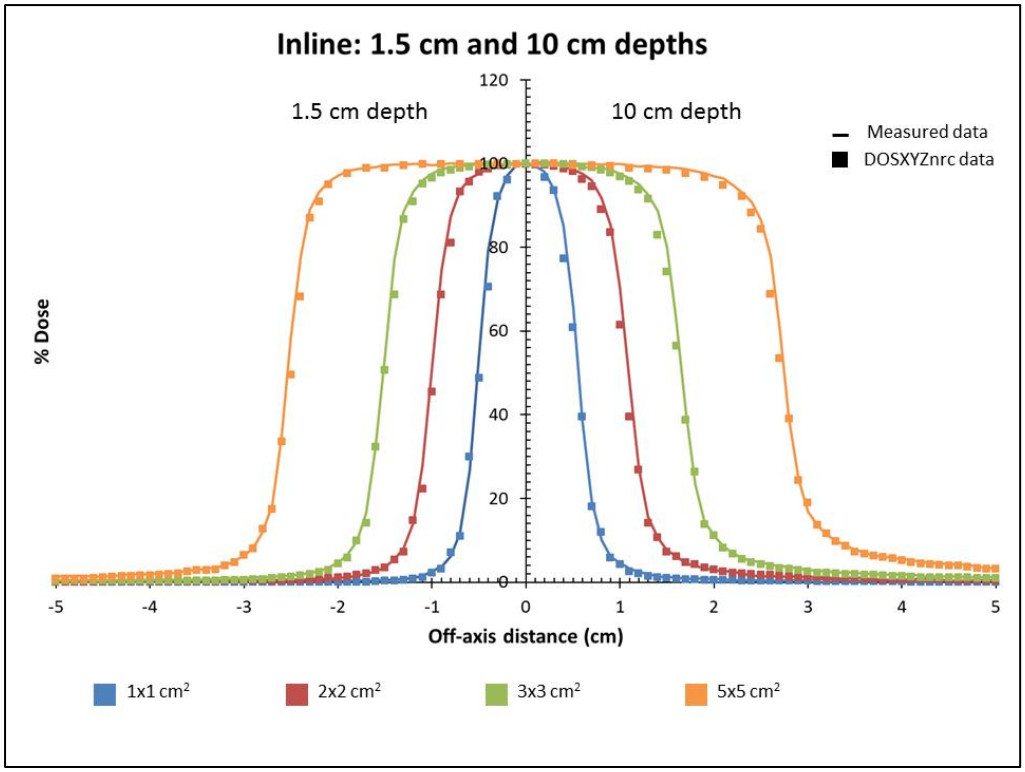

Figure 4-9: Inline profiles for 1.5 cm and 10 cm depths for the group of small fields. Measured data (-) are compared to DOSXYZnrc data (▪).

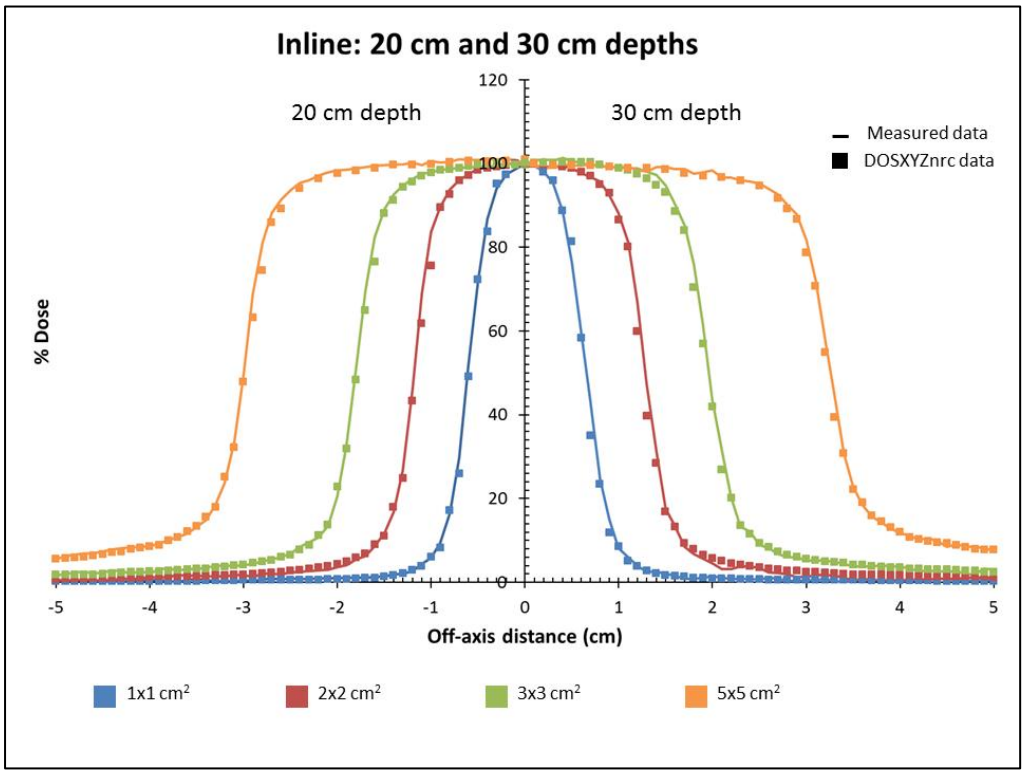

Figure 4-10: Inline profiles for 20 cm and 30 cm depths for the group of small fields. Measured data (-) are compared to DOSXYZnrc data (▪).

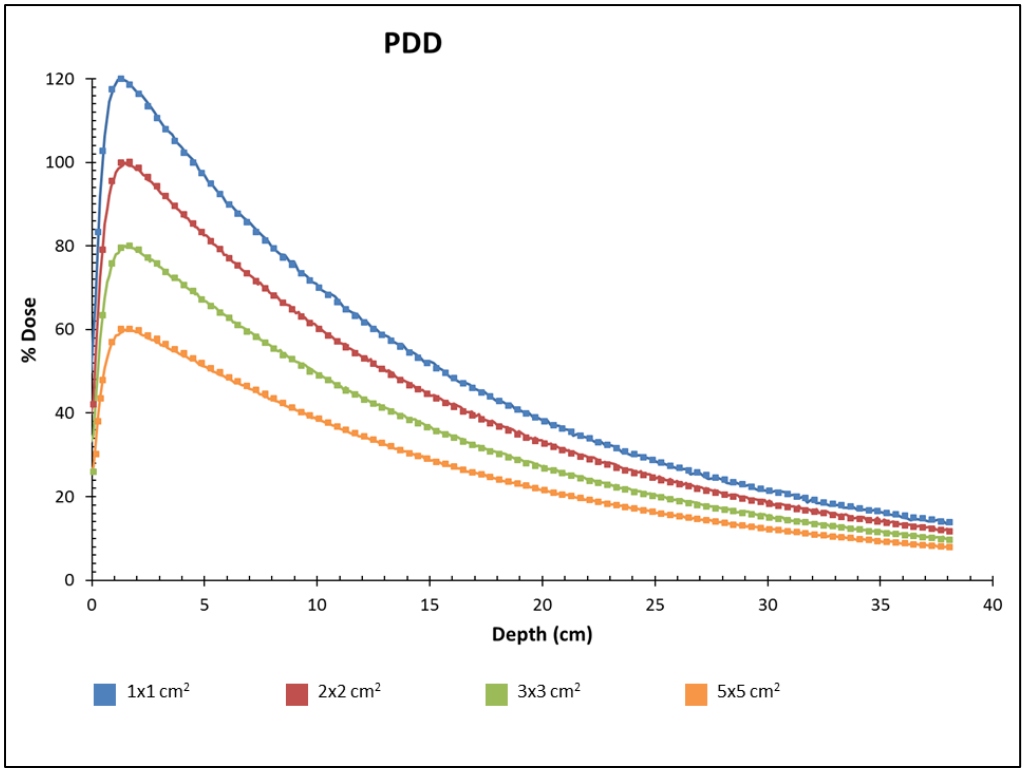

Figure 4-11: Percentage depth dose curves for field sizes 1 × 1 cm^2 to 5 × 5 cm^2

4.2.2 10 × 10 cm^2 – 40 × 40 cm^2 fields

The following parameters were used for the modulation of the 10 × 10 cm^2 to 40 × 40 cm^2 fields.

Table 4-2: Field parameters for field sizes 10 × 10 cm^2 to 40 × 40 cm^2. The σ- value for the MLC x and y is 0.5 and 0.3 respectively and the target σ is 80 over all the fields.

Field size	JAWS										Max photon energy
	X					Y					
	Position	σ	T	mu1	mu2	Position	σ	T	mu1	mu2	
10x10	5.12	0.25	0.06	0.1	0.2	5.22	0.4	0.3	0	0.65	7
15x15	7.3	0.25	0.06	0.1	0.2	7.5	0.4	0.3	0	0.65	6.5
20x20	10	0.25	0.07	0.1	0.2	10.1	0.4	0.4	0.1	0.65	6.3
25x25	12.85	0.25	0.07	0.1	0.2	12.85	0.4	0.4	0.1	0.65	6.3
30x30	14.9	0.25	0.07	0.1	0.2	14.9	0.4	0.4	0.165	0.65	6.3
35x35	17.4	0.25	0.07	0.1	0.2	17.5	0.4	0.4	0.165	0.65	6.3
40x40	20	0.25	0.07	0.165	0.65	20	0.4	0.4	0.165	0.65	6.3

In Table 4-2 a trend is seen as in the case of the smaller fields. The σ values are constant for the x- and y- jaws. There is an increase in the transmission values from the 20 × 20 cm^2 field upwards. The *mu1* and *mu2* values for the x-jaws stay constant up to a 40 × 40 cm^2 field.

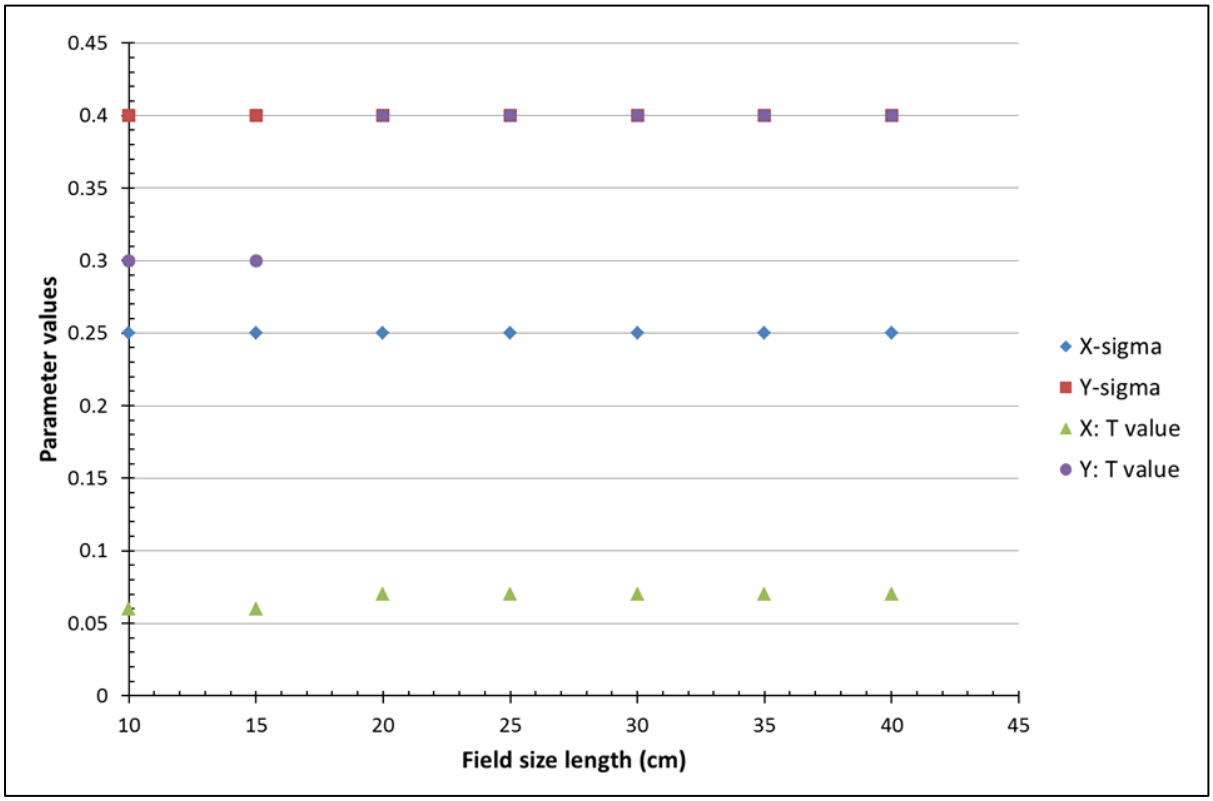

Figure 4-12: Plot of the fitted parameter values for fields from 10 × 10 cm^2 to 40 × 40cm^2

The MLC settings for the larger fields are shown in Figure 4-13. The open and closed leaves correspond to those on the linac.

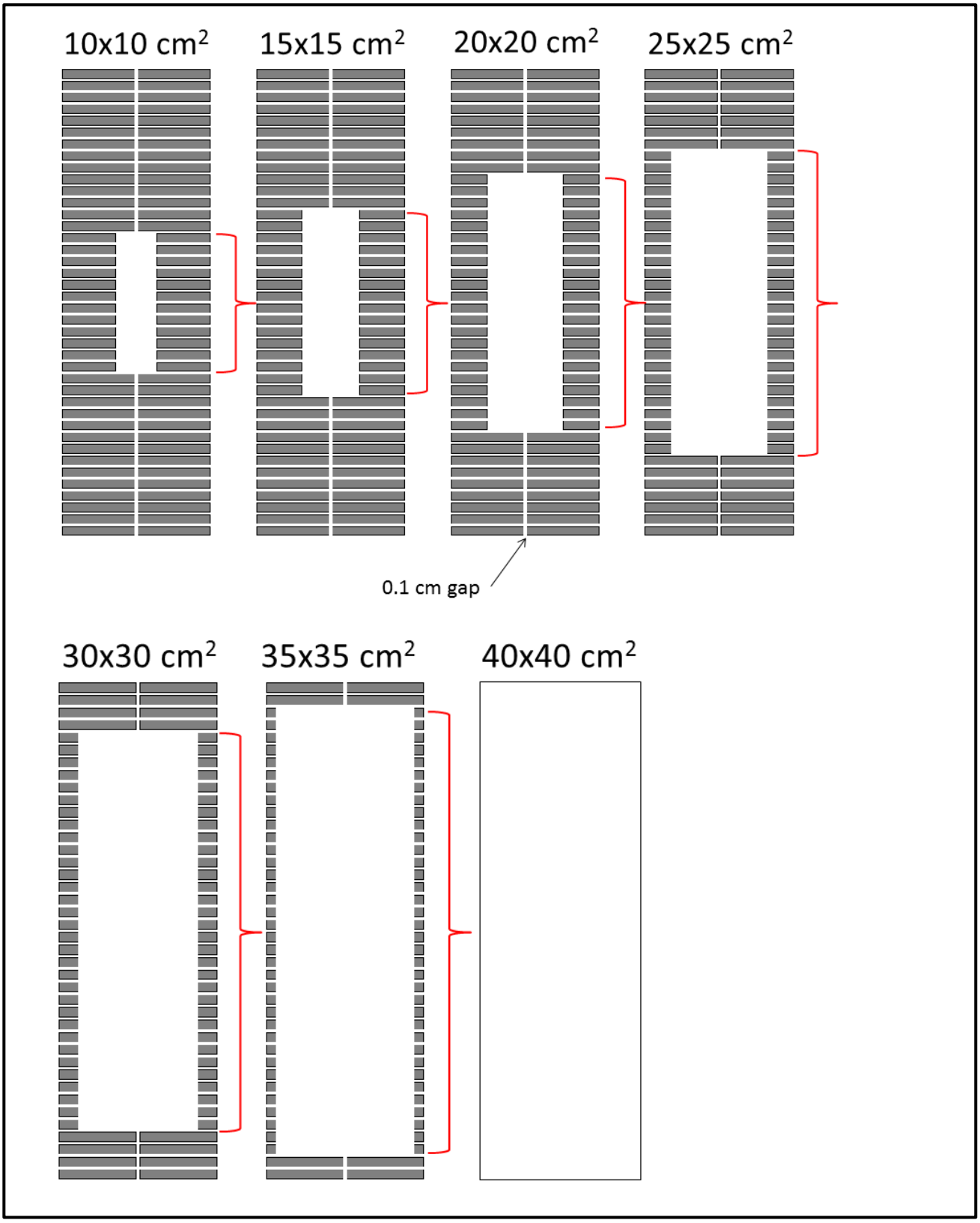

Figure 4-13: The MLC configuration for field sizes 10 x 10 cm^2 to 40 x 40 cm^2.

The fluence obtained for the different fields are shown in Figure 4-14 for the inline and crossline direction.

10x10 cm^2

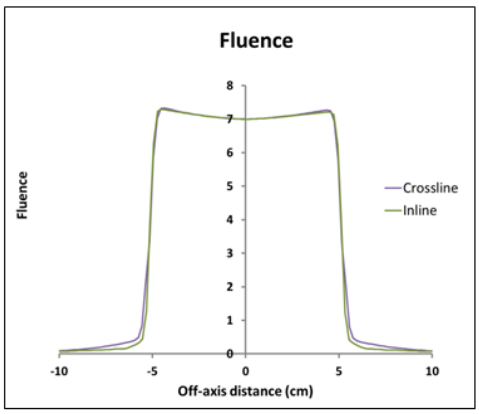

15x15 cm^2

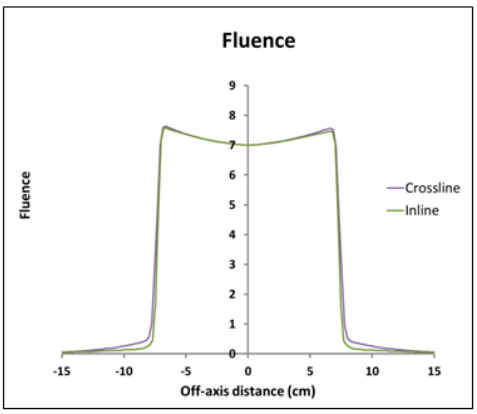

20x20 cm^2

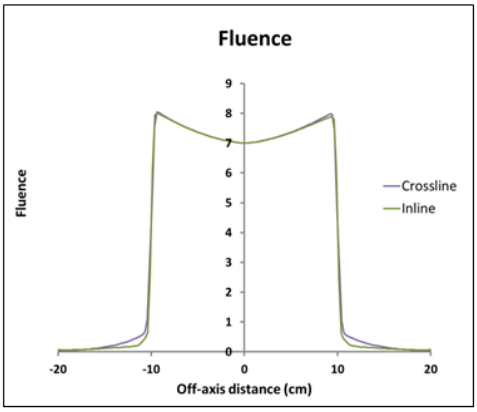

25x25 cm^2

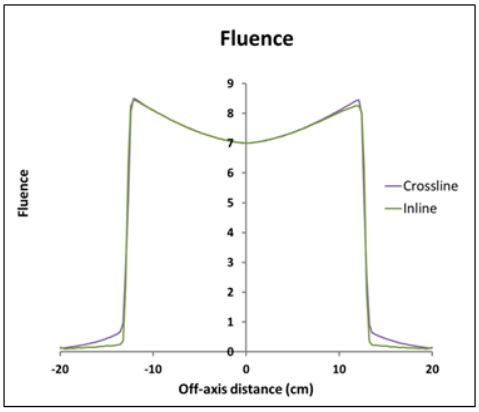

30x30 cm^2

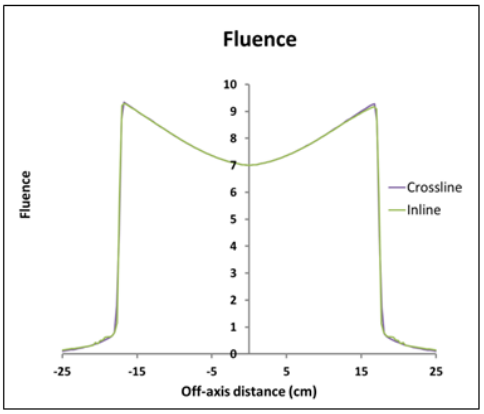

35x35 cm^2

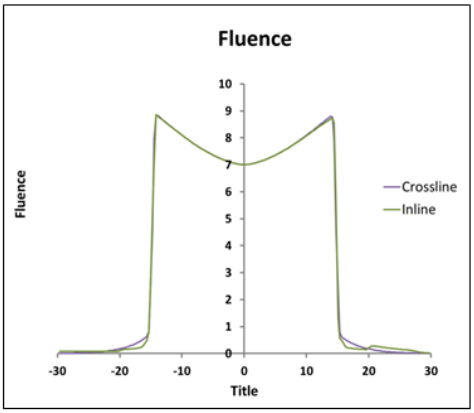

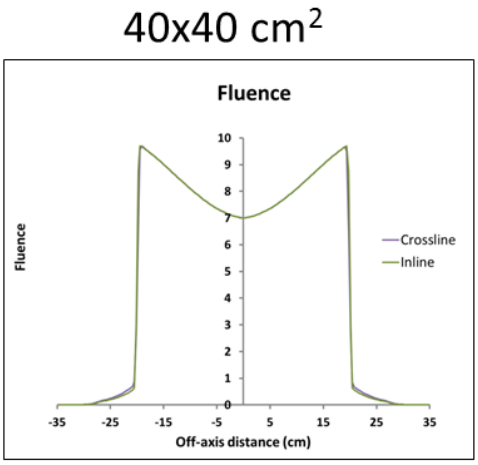

Figure 4-14: The fluence plots for field sizes 10 × 10 cm^2 to 40 × 40 cm^2. Note: This is just the calculated source model fluence.

The crossline and inline profiles for the field sizes 10 × 10 cm^2 to 40 × 40 cm^2 for 1.5, 10, 20 and 30 cm depths are shown in the following figures. The gamma index values were below 1 for all the field sizes at the different depths. All the profiles and PDD curves are normalized to different values in order to distinguish between them.

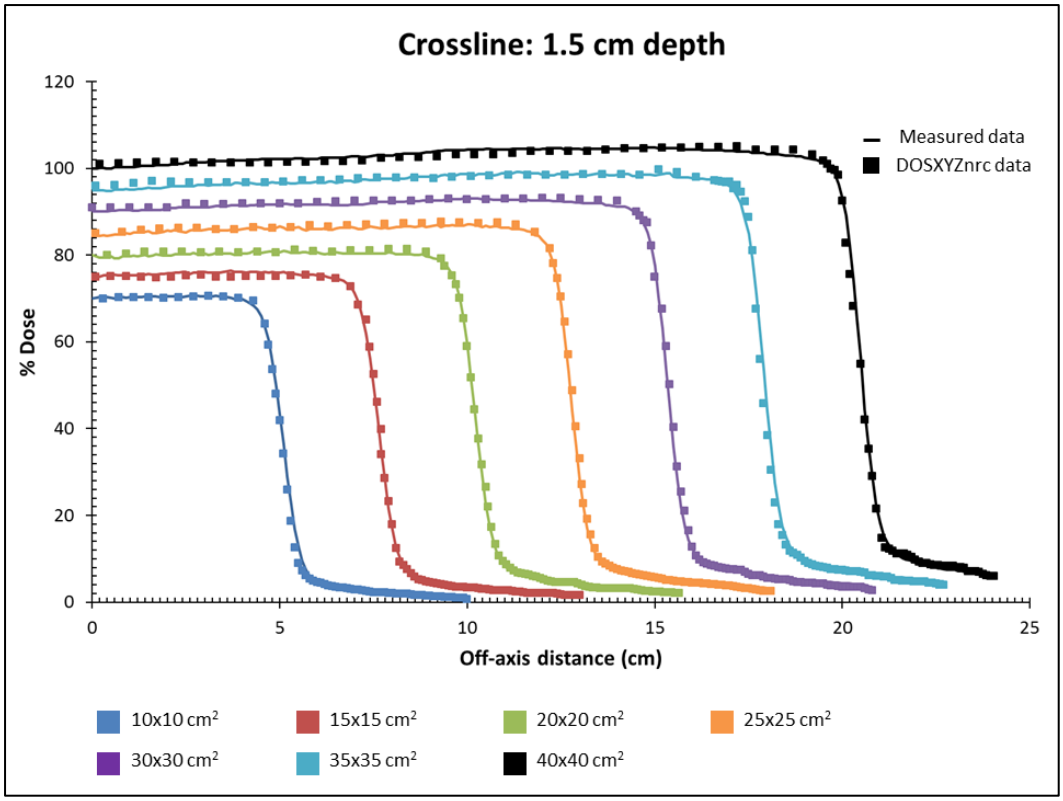

Figure 4-15: Crossline profiles for 1.5 cm depth for the group of larger fields. Measured data (-) are compared to DOSXYZnrc data (▪).

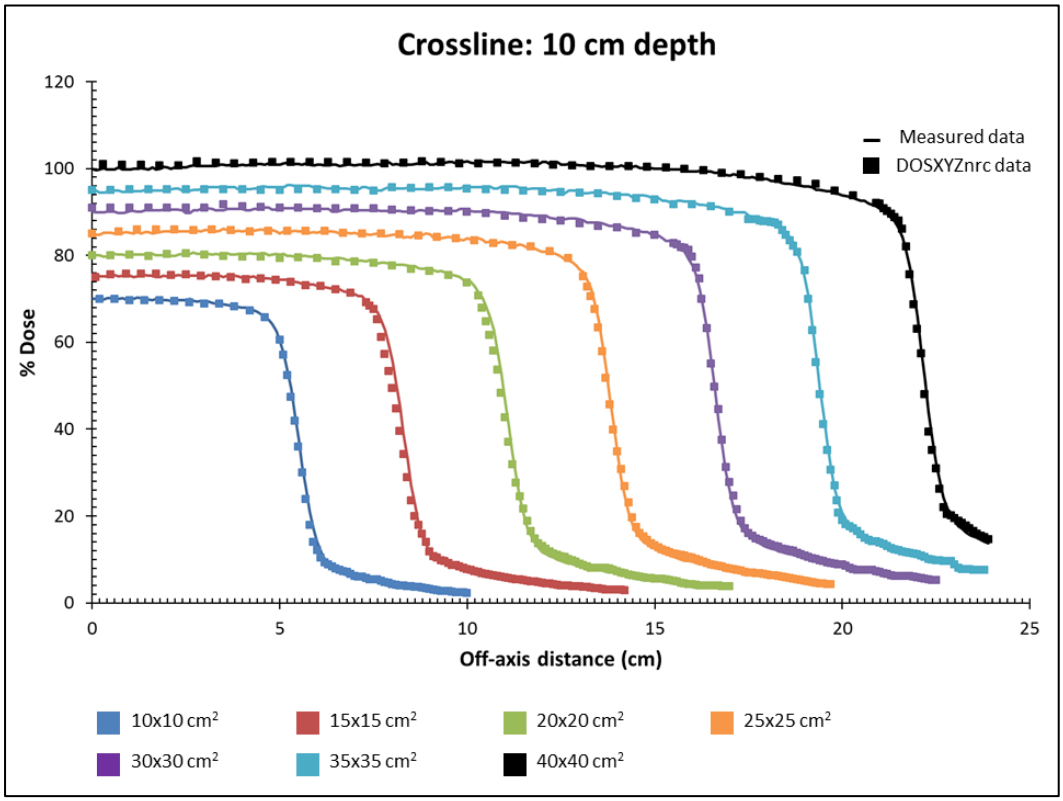

Figure 4-16: Crossline profiles for 10 cm depth for the group of larger fields. Measured data (-) are compared to DOSXYZnrc data (▪).

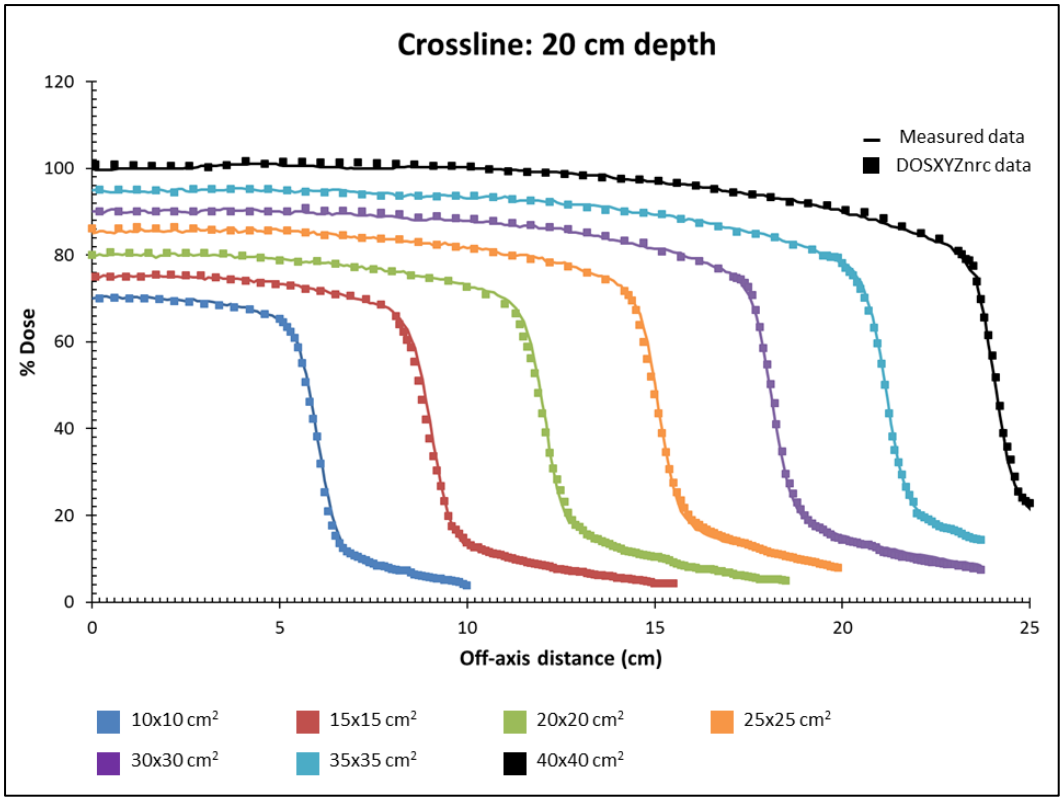

Figure 4-17: Crossline profiles for 20 cm depth for the group of larger fields. Measured data (-) are compared to DOSXYZnrc data (▪).

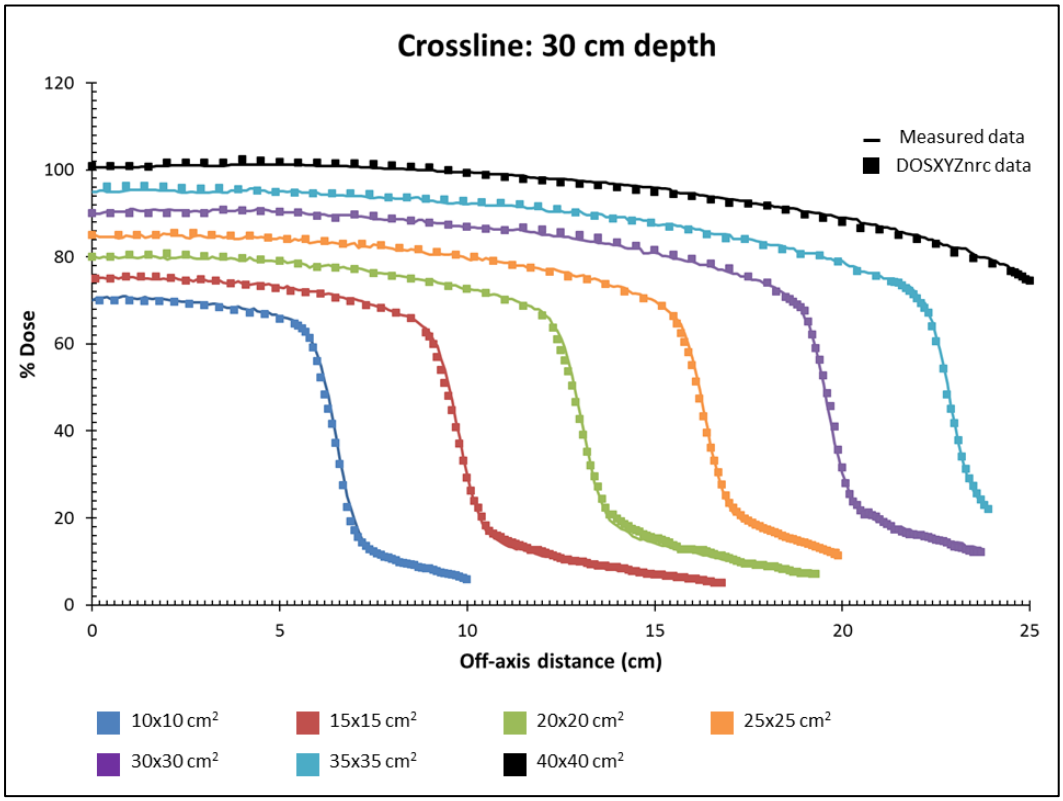

Figure 4-18: Crossline profiles for 30 cm depth for the group of larger fields. Measured data (-) are compared to DOSXYZnrc data (▪).

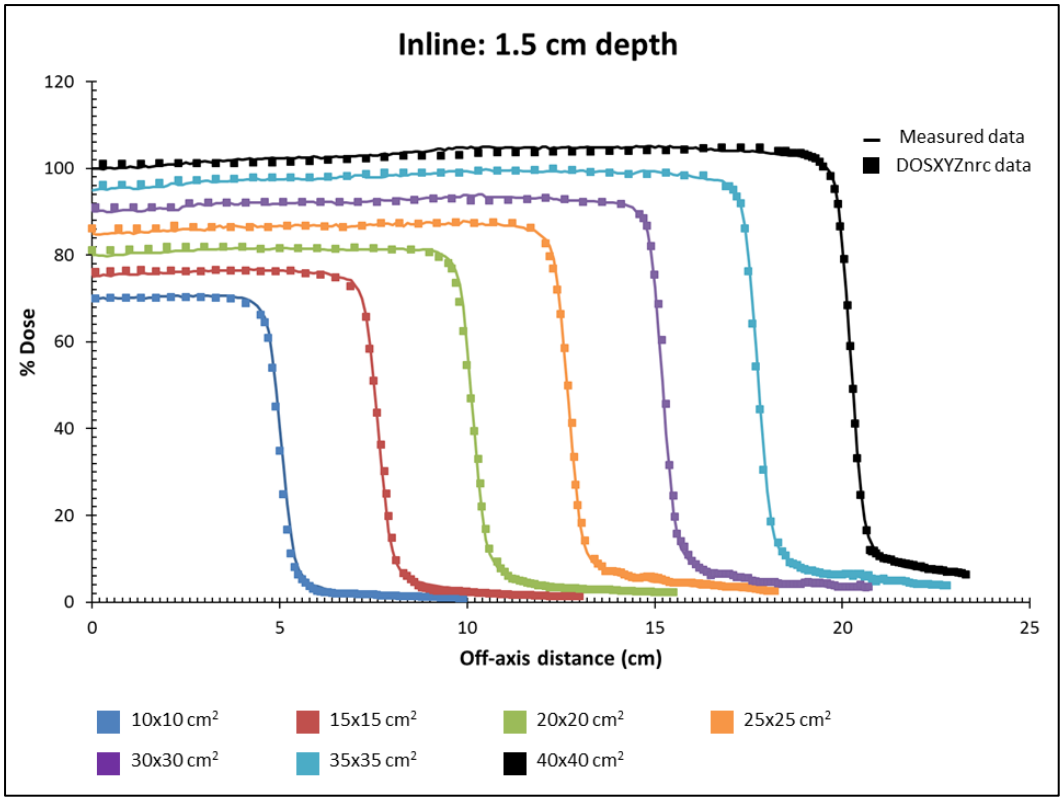

Figure 4-19: Inline profiles for 1.5 cm depth for the group of larger fields. Measured data (-) are compared to DOSXYZnrc data (▪).

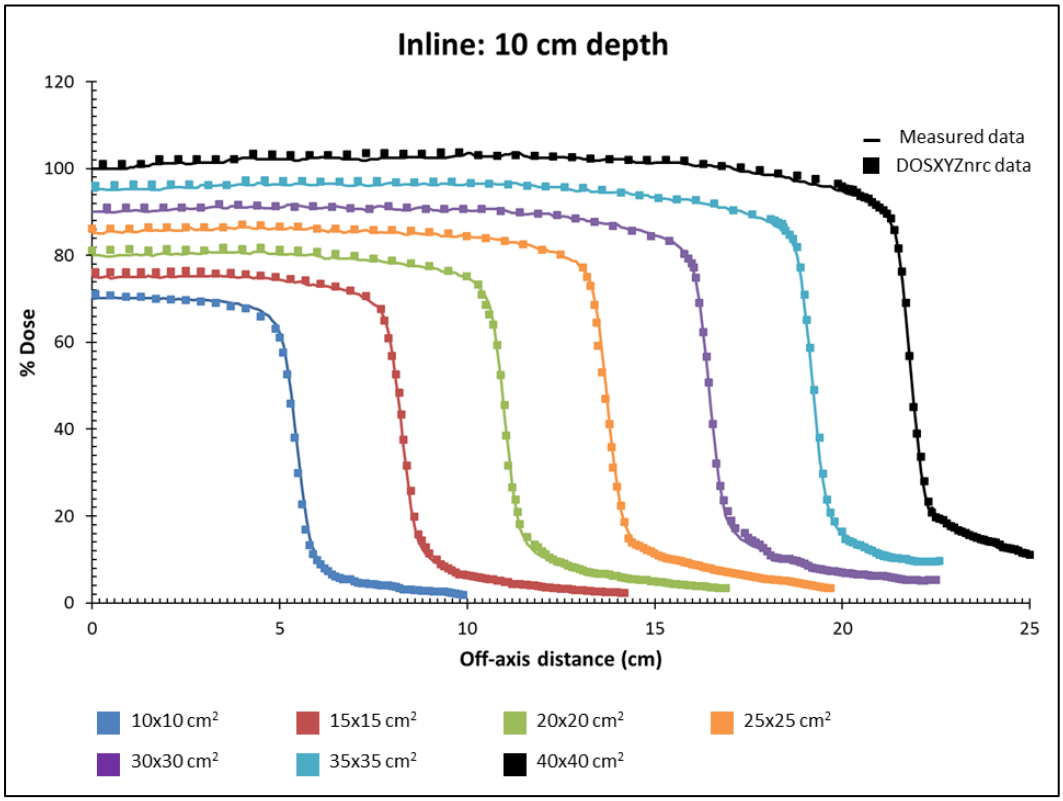

Figure 4-20: Inline profiles for 10 cm depth for the group of larger fields. Measured data (-) are compared to DOSXYZnrc data (▪).

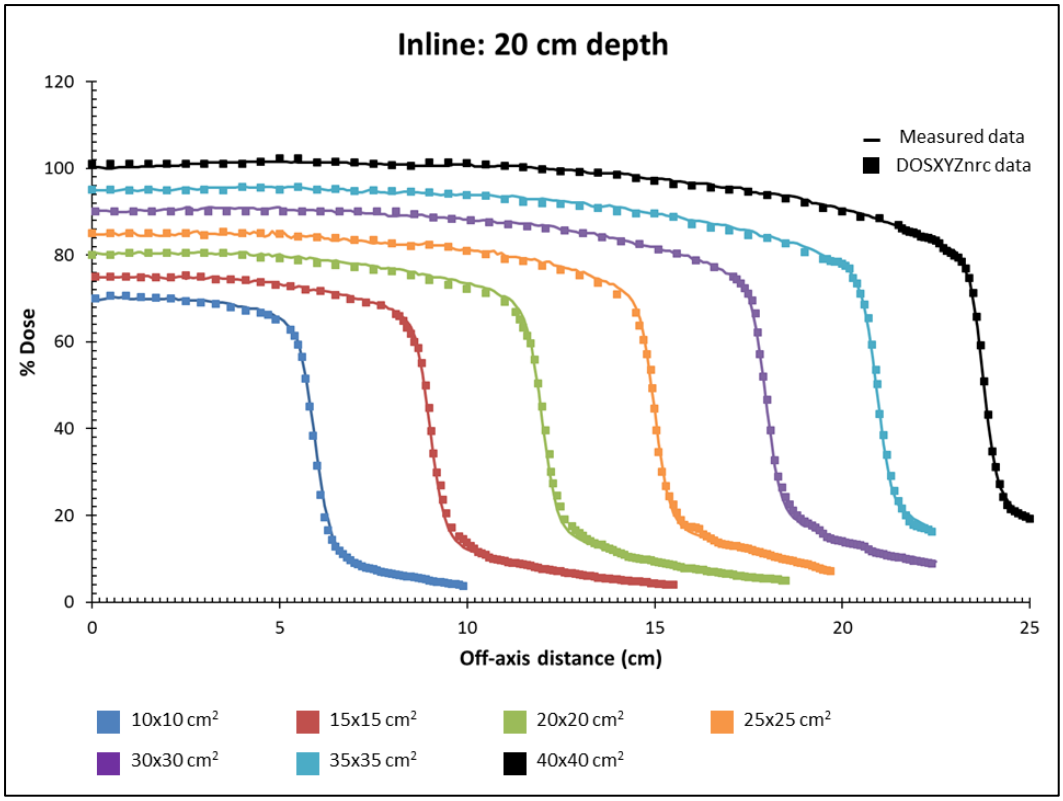

Figure 4-21: Inline profiles for 20 cm depth for the group of larger fields. Measured data (-) are compared to DOSXYZnrc data (▪).

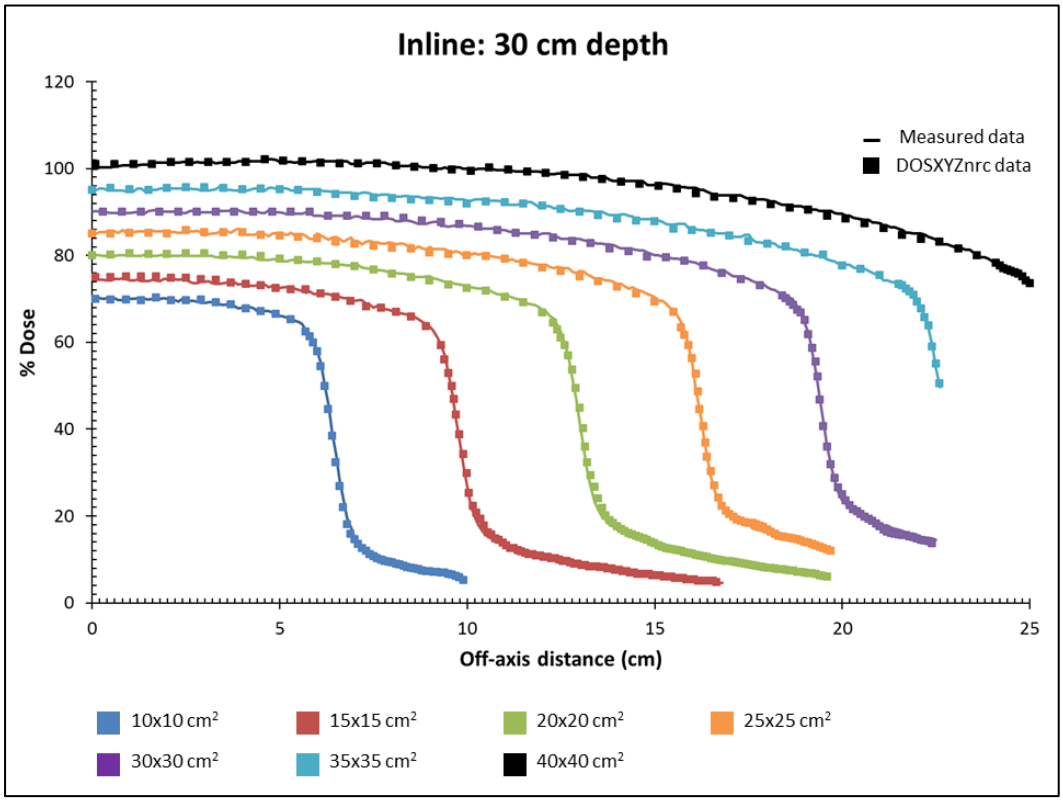

Figure 4-22: Inline profiles for 30 cm depth for the group of larger fields. Measured data (-) are compared to DOSXYZnrc data (▪).

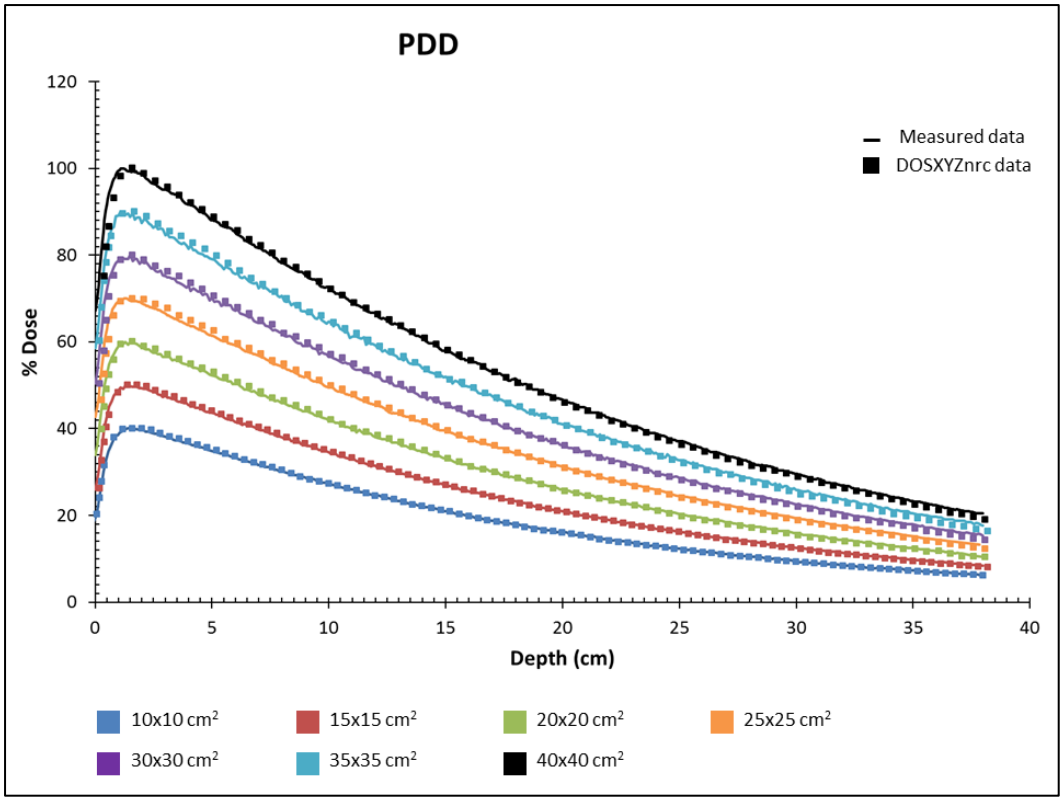

Figure 4-23: Percentage depth dose curves for field sizes 10 × 10 cm^2 to 40 × 40 cm^2.

4.3 Offset fields

The regular field source fitting parameters were used for the simulation of the offset fields e.g. if a field size consists of X_1 = A and X_2 = B then the σ values for an A × A field is used for the X_1 side and that of a B × B field is used for the X_2 side.

As described in Chapter 3 Section 3.5.3, the source model underestimates the scatter present in offset fields. This was corrected for by means of an exponential function as seen in Figure 4-24. The transmission adjustment values are shown in Figure 4-25.

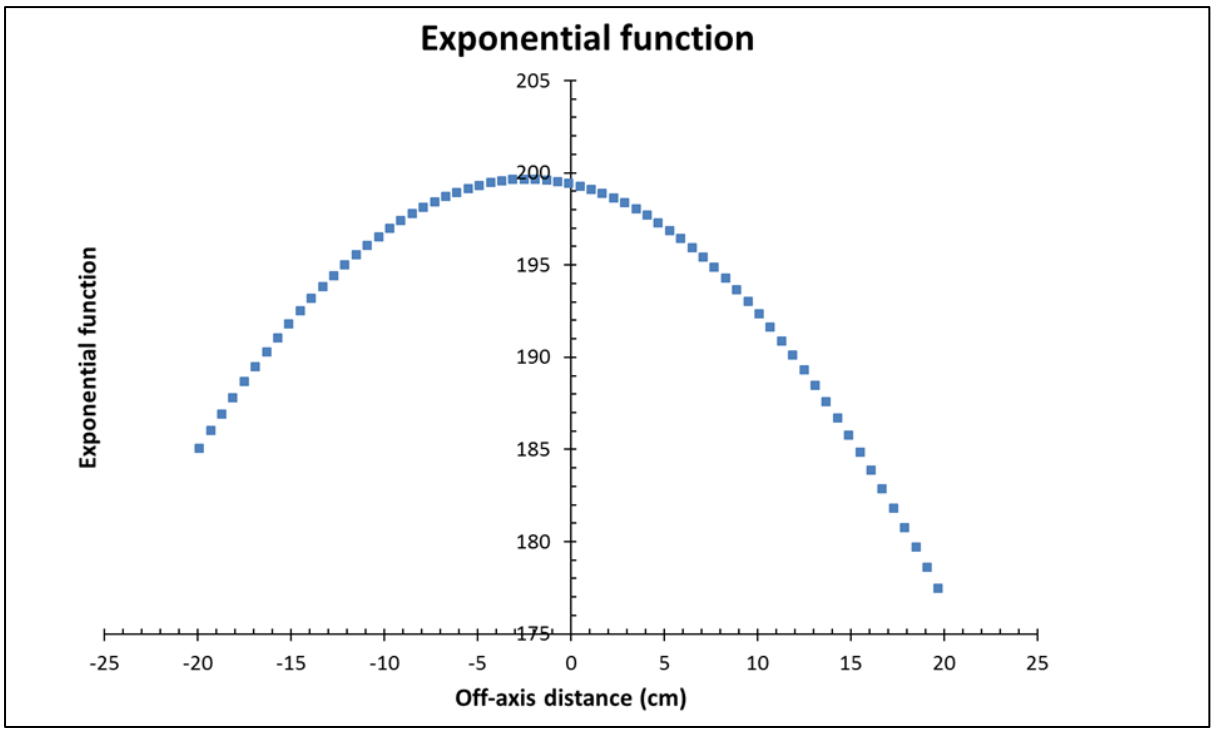

Figure 4-24: The exponential functions used to correct the scatter in the offset fields

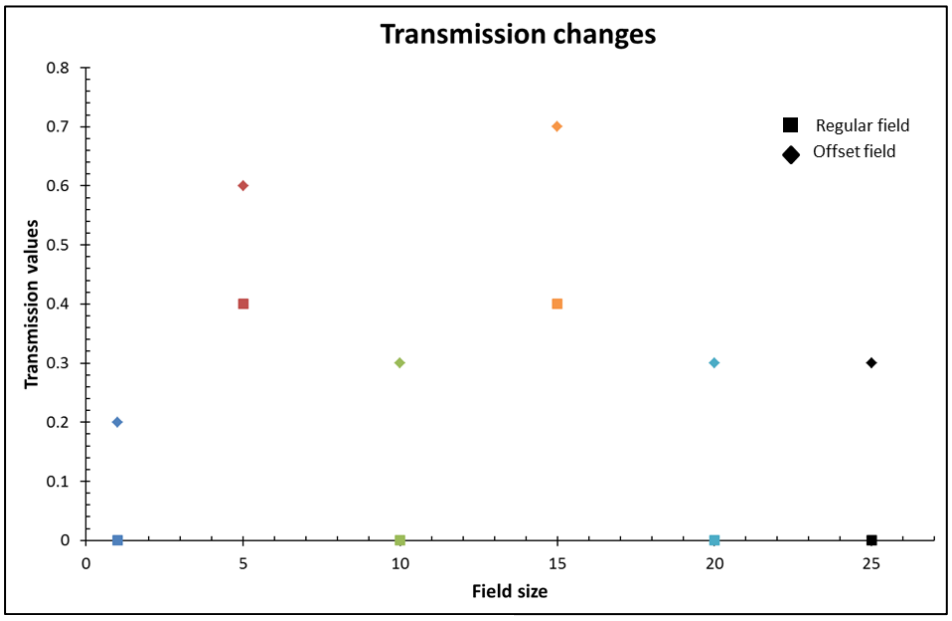

	10x10 cm^2, Inline, 10 cm offset, X1
	10x10 cm^2,Crossline, 10 cm offset, Y2
	15x15 cm^2 ,Inline, 15 cm offset, X1
	15x15 cm^2 ,Crossline, 15 cm offset, Y2
	20x20 cm^2, Inline, 20 cm offset, X1
	20x20 cm^2, Crossline, 20 cm offset, Y2

Figure 4-25: Transmission changes from the regular field fitting parameters to the offset field fitting parameters for each offset field respectively.

The following results are for the 10 × 10 cm^2 field with a 10 cm offset, 15 × 15 cm^2 field with a 15 cm offset and a 20 × 20 cm^2 field with a 20 cm offset in both the inline and crossline directions. The depths are 1.5 , 10 , 20 and 30 cm as shown on the graphs. The red graph indicates the offset in the inline (*x*) direction and the blue graph the offset in the crossline (*y*) direction. The gamma index values were below 1 for all the field sizes at the different depths. Different normalization values are used in order to distinguish between the different fields.

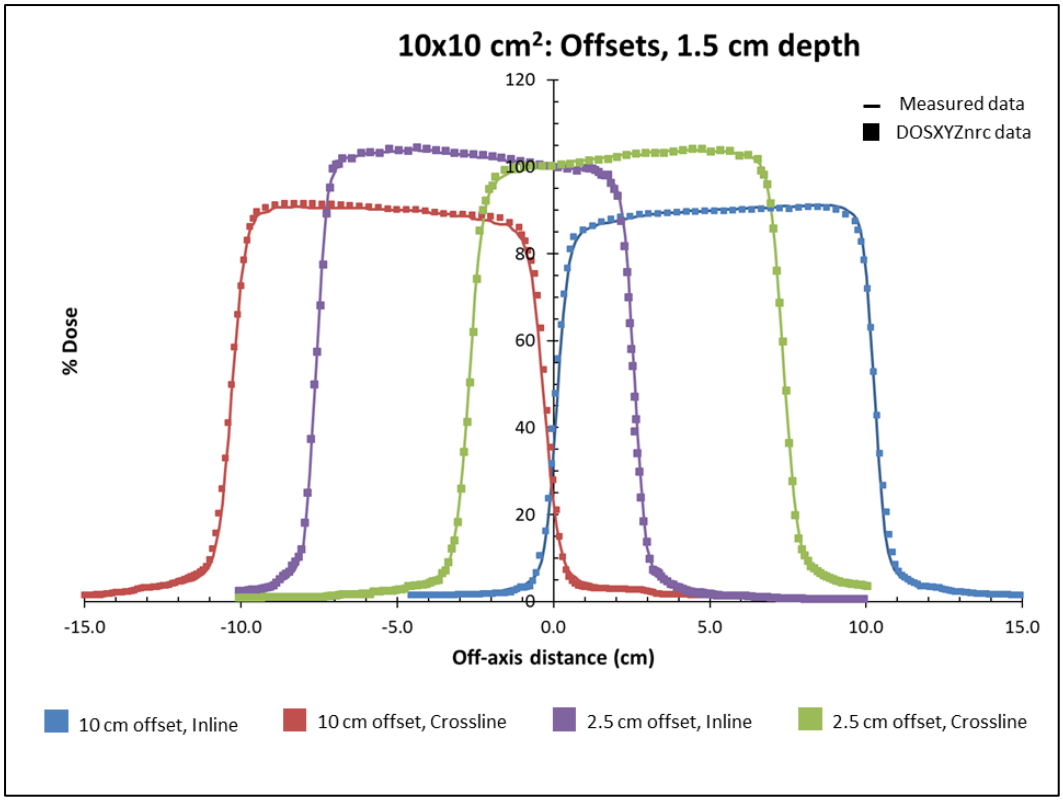

Figure 4-26: 10 × 10 cm^2 field offsets in both directions at 1.5 cm depth.

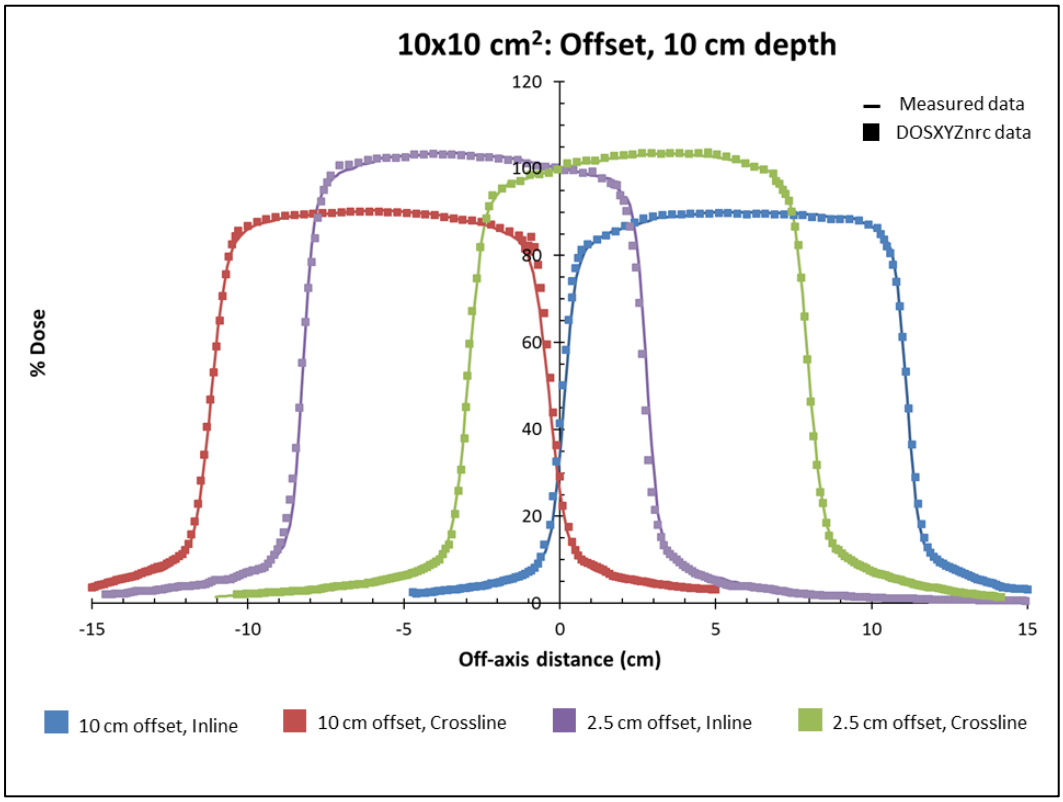

Figure 4-27: 10 × 10 cm^2 field offsets in both directions at 10 cm depth.

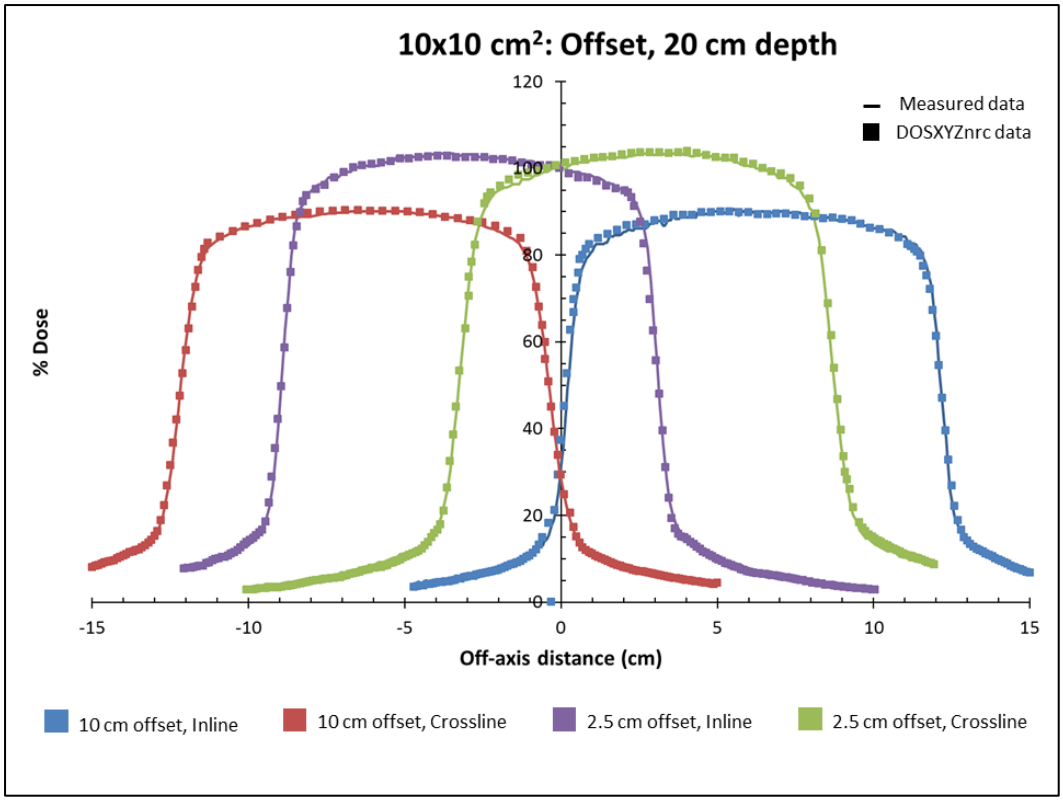

Figure 4-28: 10 × 10 cm^2 field offsets in both directions at 20 cm depth.

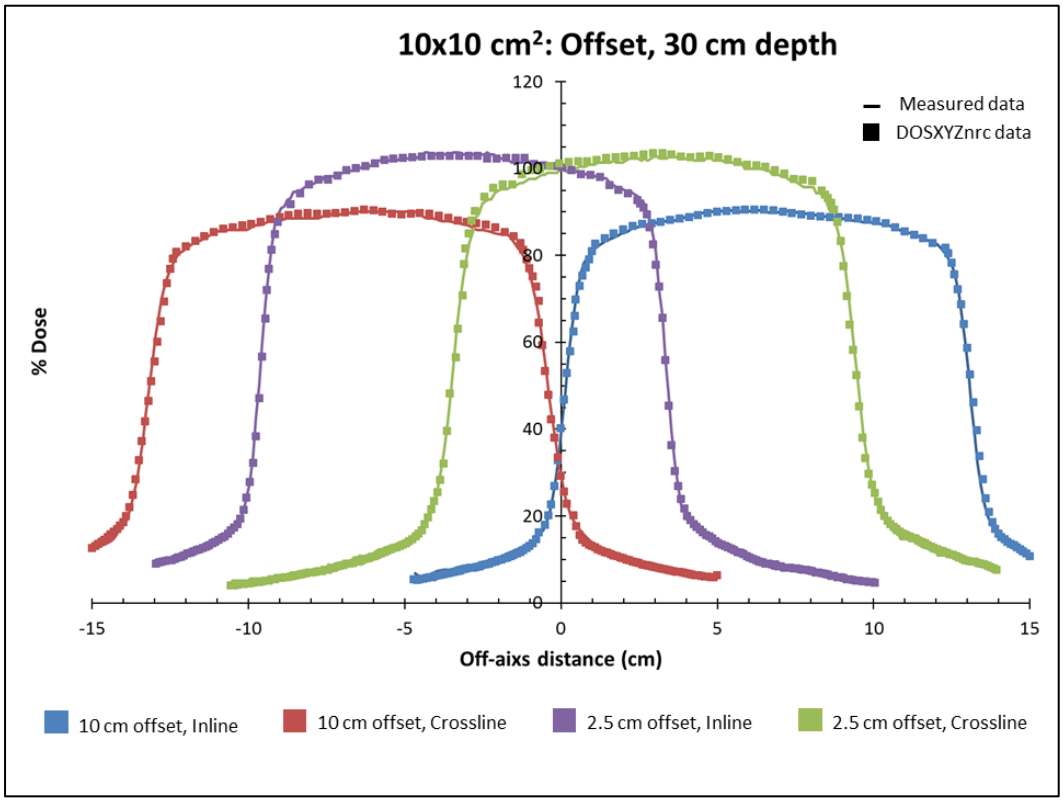

Figure 4-29: 10 × 10 cm^2 field offsets in both directions at 30 cm depth.

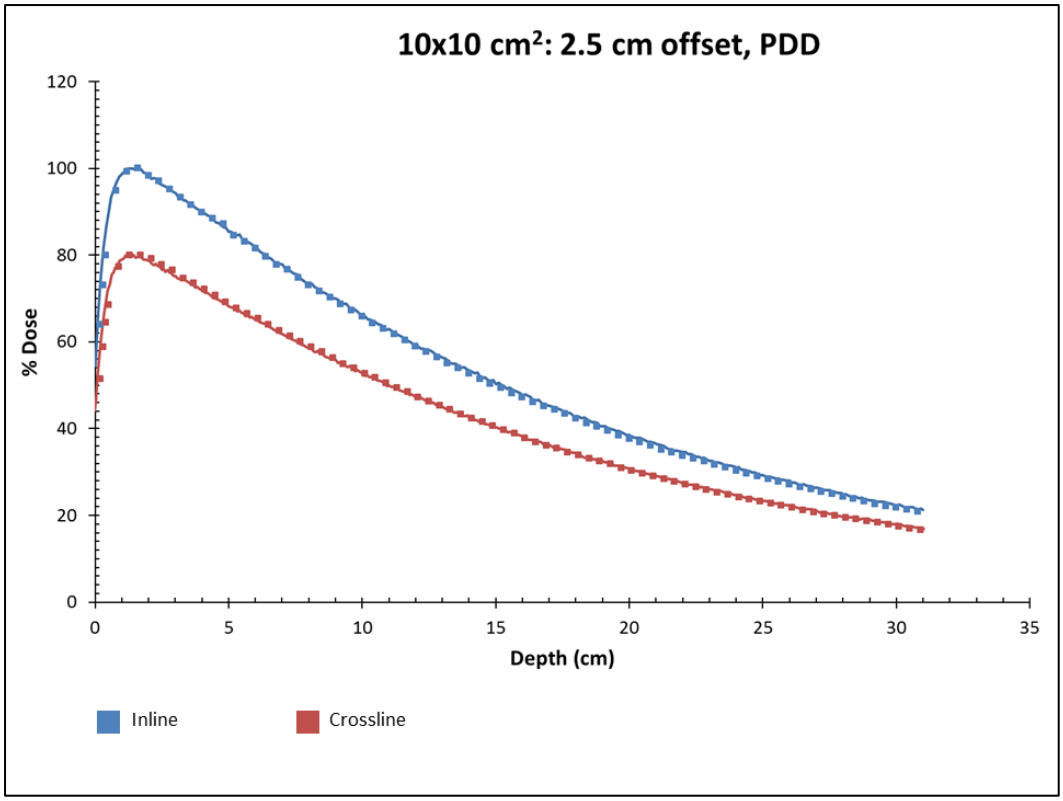

Figure 4-30: Percentage depth dose curves for 10 × 10 cm^2 field with 2.5 cm offsets in both directions.

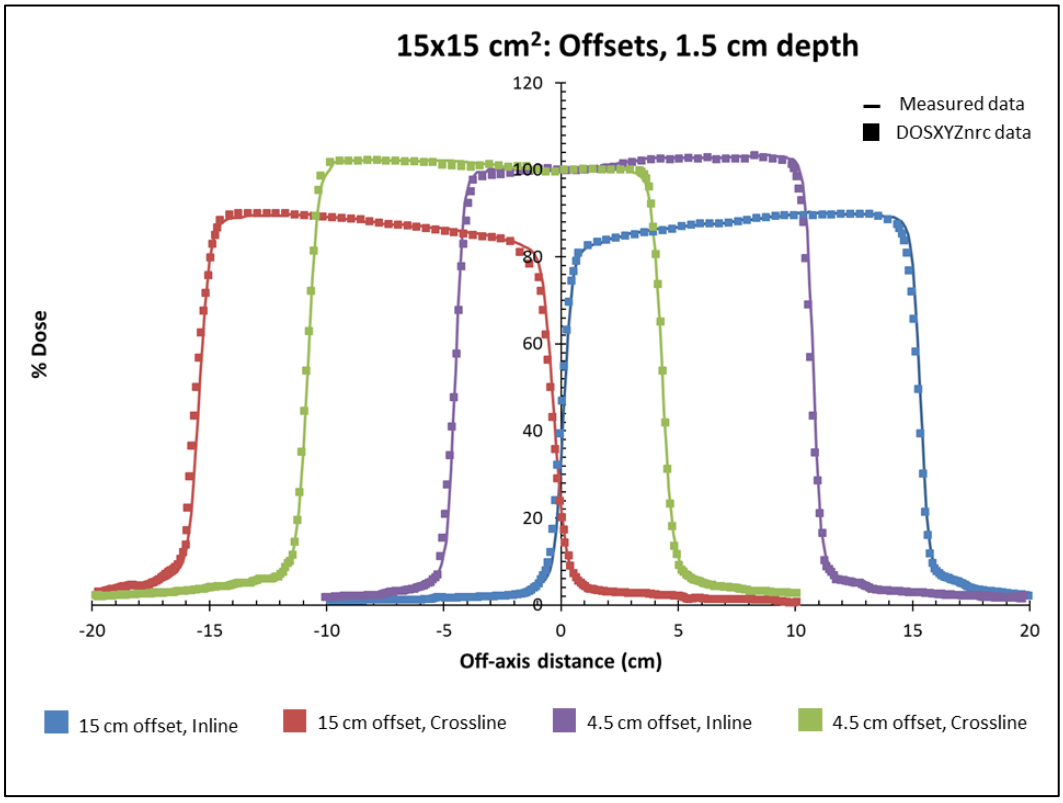

Figure 4-31: 15 × 15 cm^2 field offsets in both directions at 1.5 cm depth.

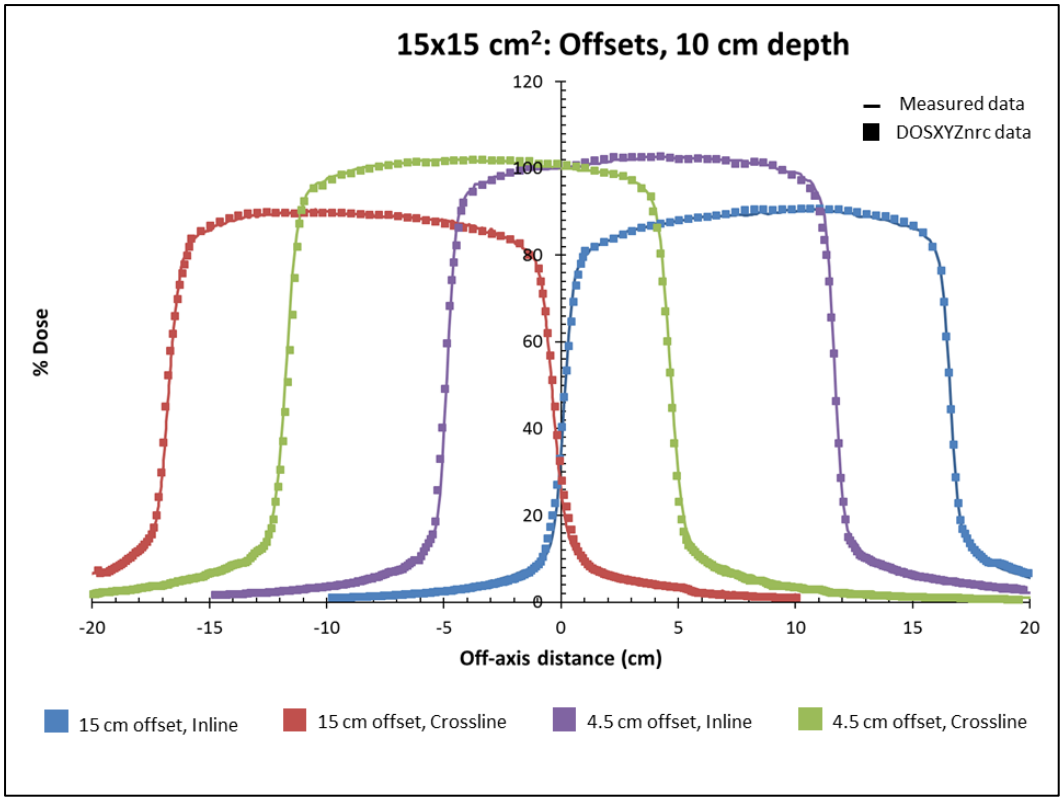

Figure 4-32: 15 × 15 cm^2 field offsets in both directions at 10 cm depth.

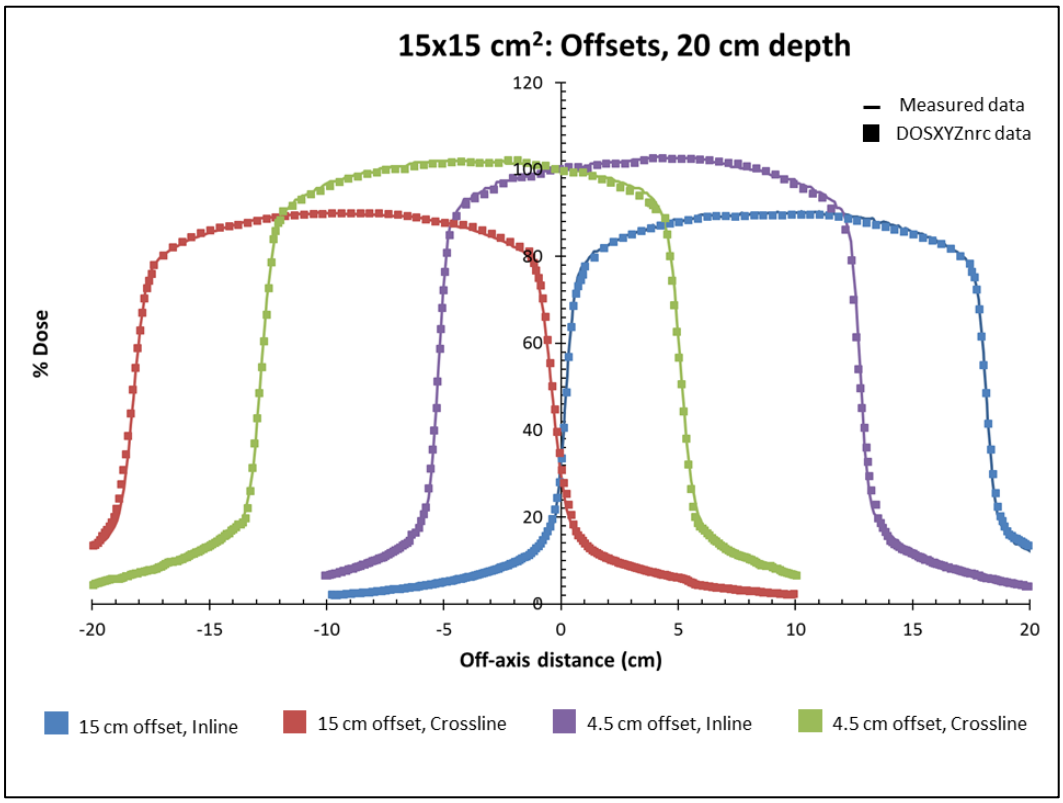

Figure 4-33: 15 × 15 cm^2 field offsets in both directions at 20 cm depth.

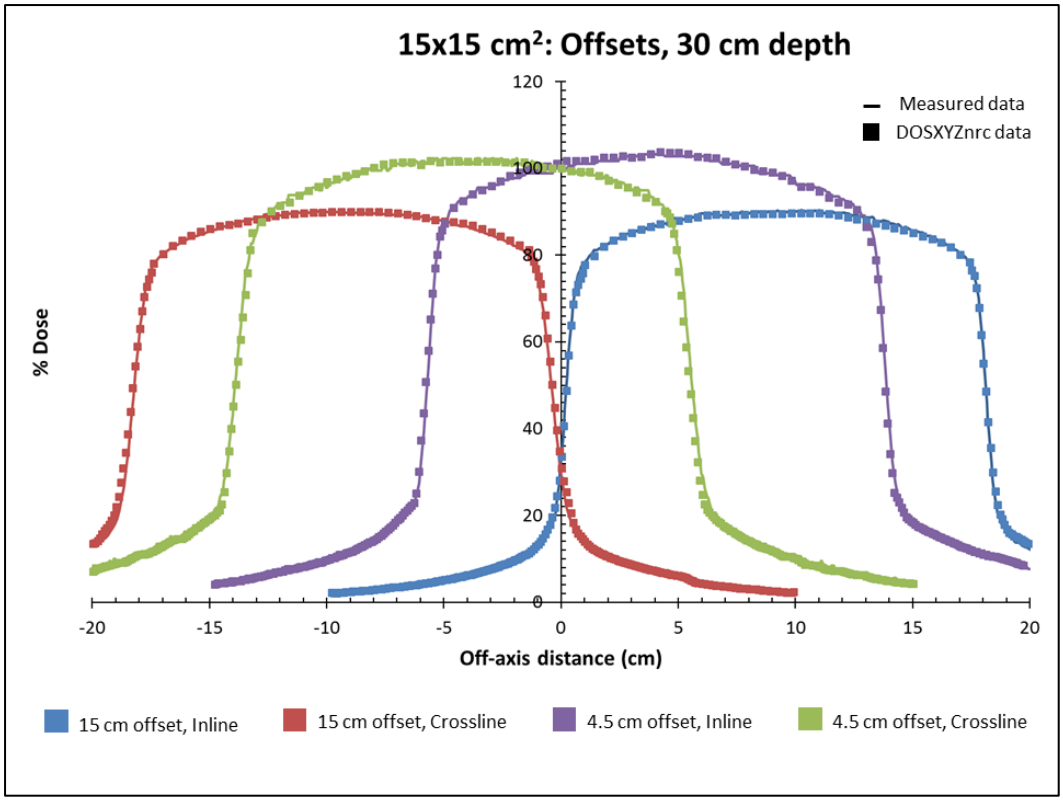

Figure 4-34: 15 × 15 cm^2 field offsets in both directions at 30 cm depth.

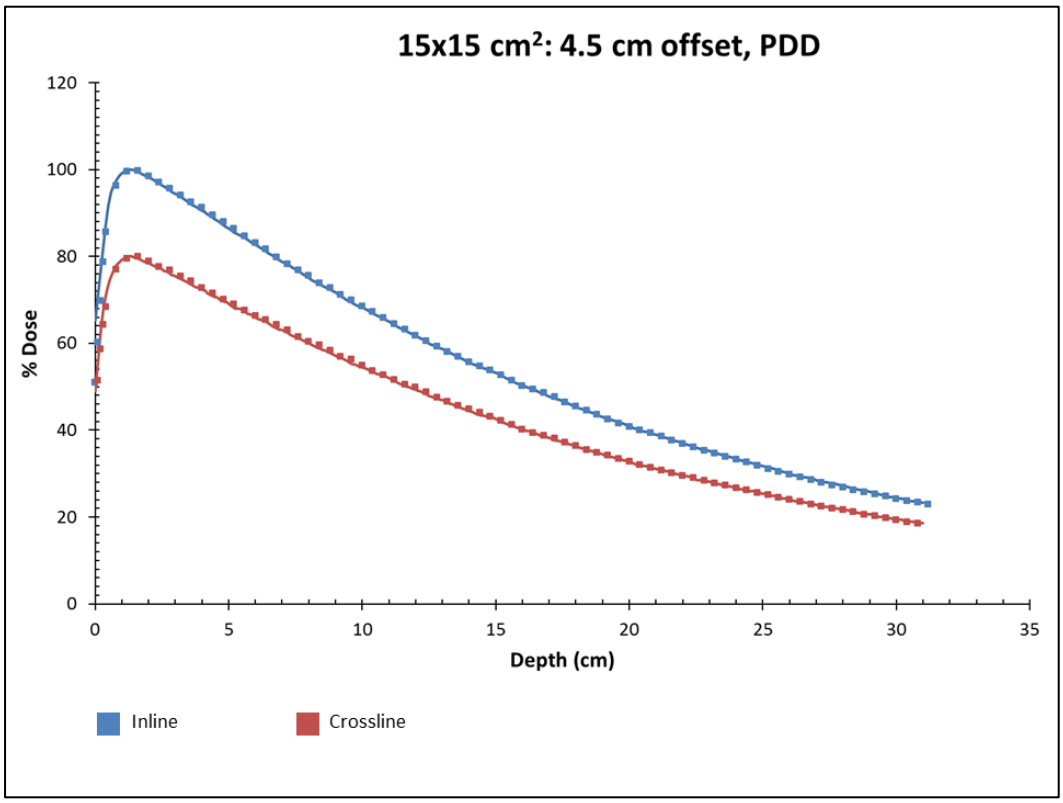

Figure 4-35: Percentage depth dose curves for 15 × 15 cm^2 field with 4.5 cm offsets in both directions.

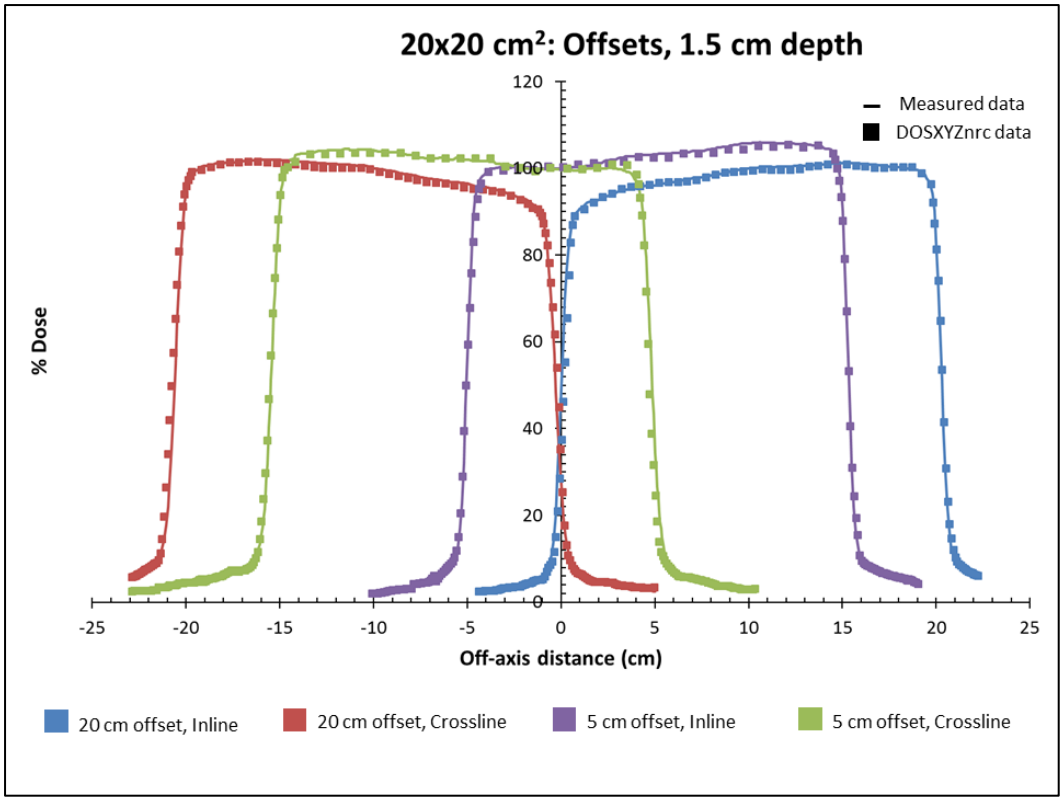

Figure 4-36: 20 × 20 cm^2 field offsets in both directions at 1.5 cm depth.

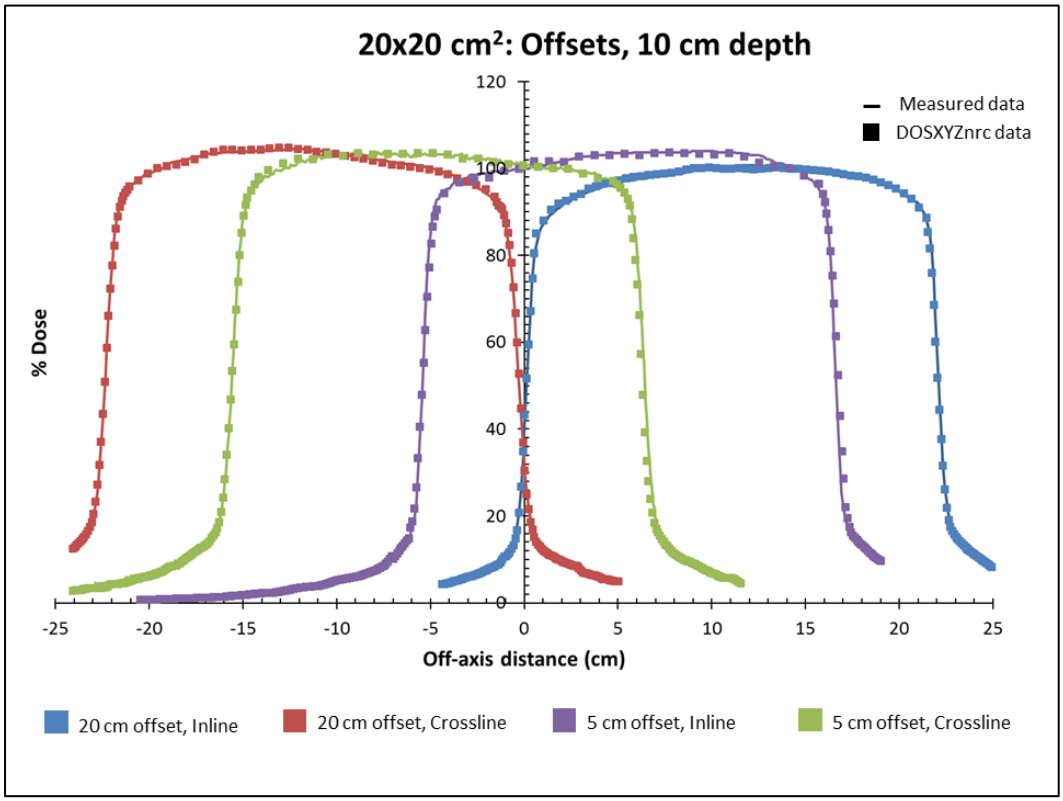

Figure 4-37: 20 × 20 cm^2 field offsets in both directions at 10 cm depth.

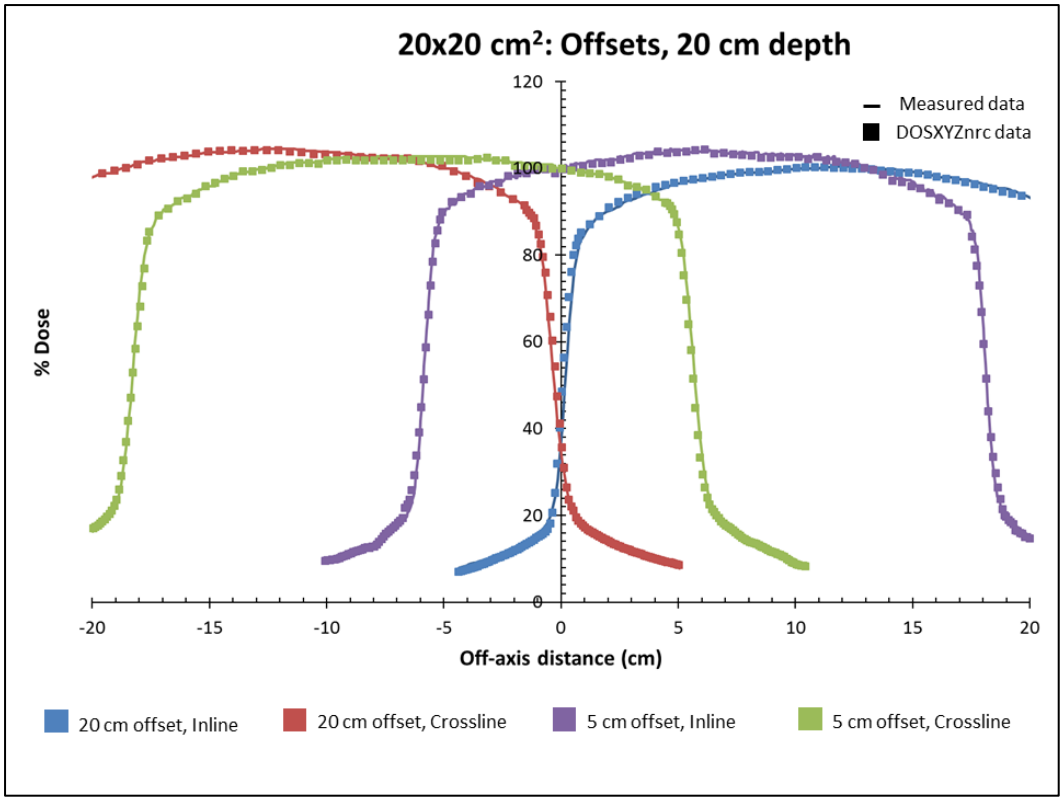

Figure 4-38: 20 × 20 cm^2 field offsets in both directions at 20 cm depth.

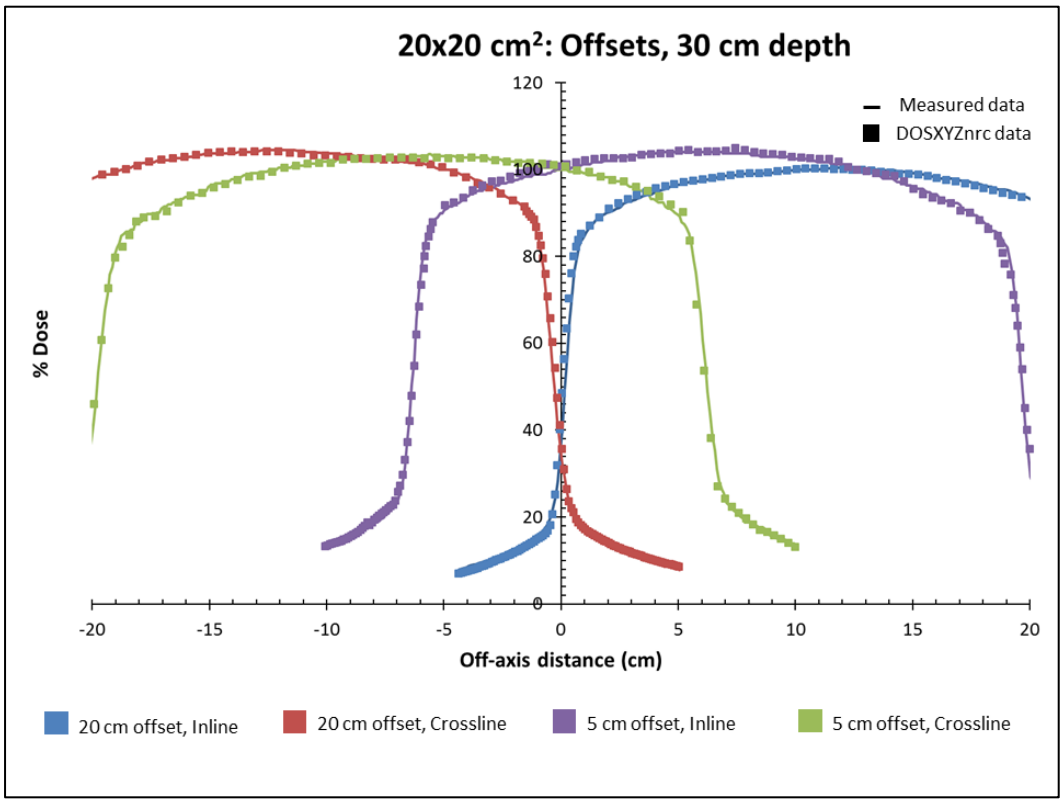

Figure 4-39: 20 × 20 cm^2 field offsets in both directions at 30 cm depth.

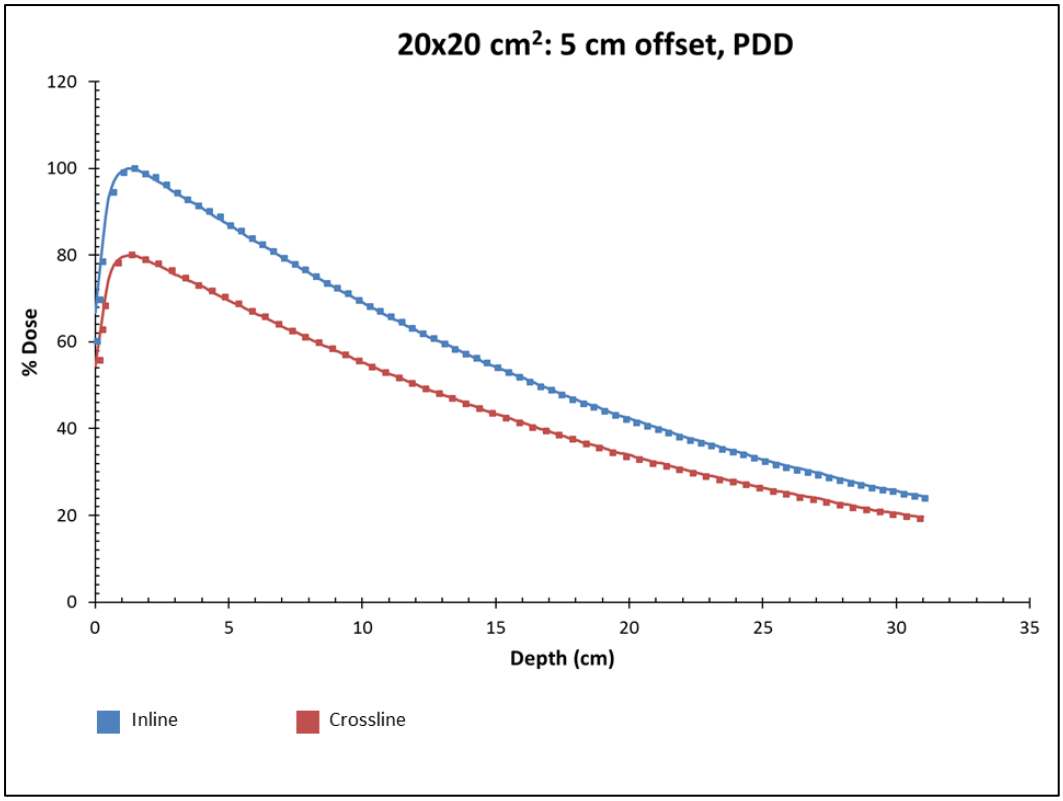

Figure 4-40: Percentage depth dose curves for 20 × 20 cm^2 field with 5 cm offsets in both directions.

4.4 Wedged fields

The exponential function used to attenuate the fluence to emulate the wedge is shown in Figure 4-41.

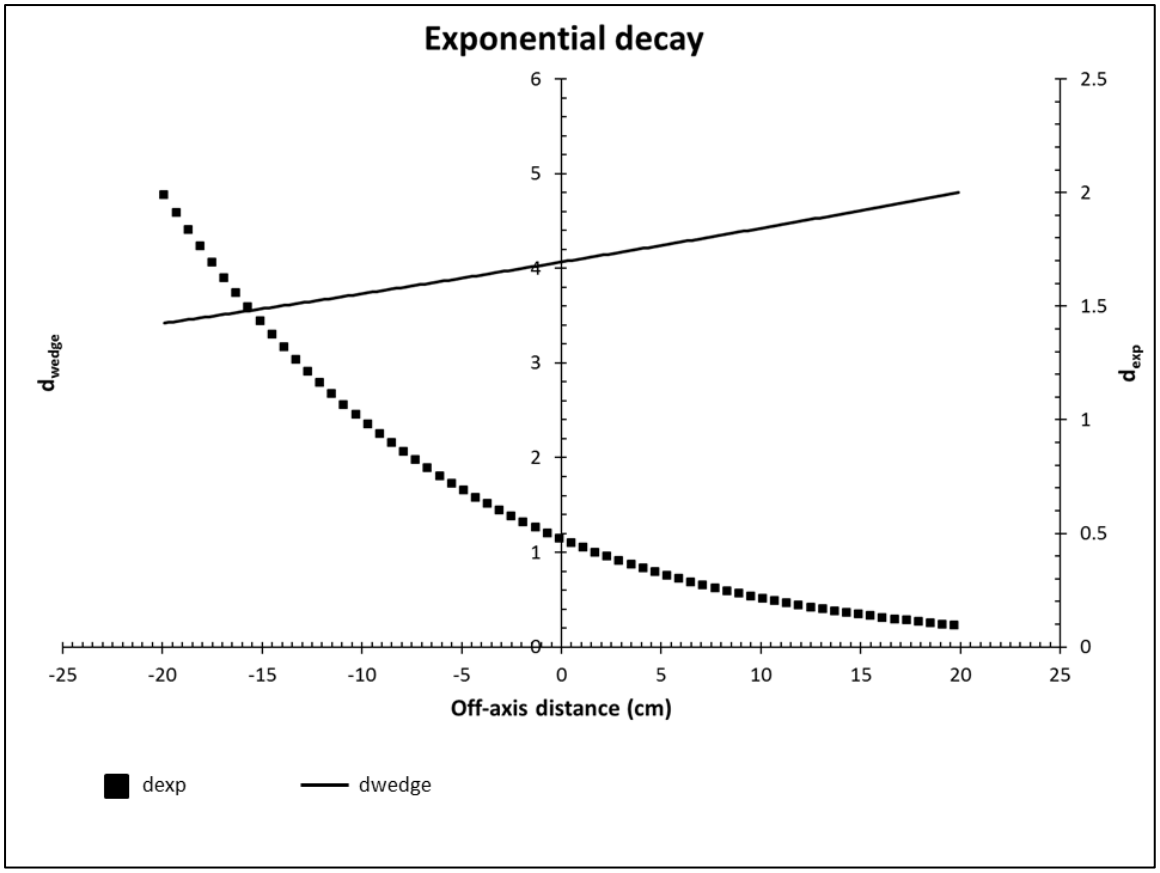

Figure 4-41: The exponential functions used for the wedged fields. D_{wedge} is the thickness of the wedge and d_{exp} is the attenuation of the fluence.

The parameter *C1* has a value of 25 that was found by fitting the exponential function to the measured data. The constants k_1 and k_2 have values of -2.22 and 0.00025268 respectively that was determined previously with full Monte Carlo simulations.

$$d_{wedge} = 5.0 - 0.0401 \times (C1 - x) + 0.00011 \times (C1 - x)^2 \qquad (2\text{-}24)$$

$$d_{\exp}(x) = \exp(-k_1 \times d_{wedge}(x)) / k_2 \qquad (2\text{-}26)$$

The differences in transmission for the regular fields and wedged fields are shown in Figure 4-42 to 4-44. The parameter values for the wedges fields are shown in Table 4-3.

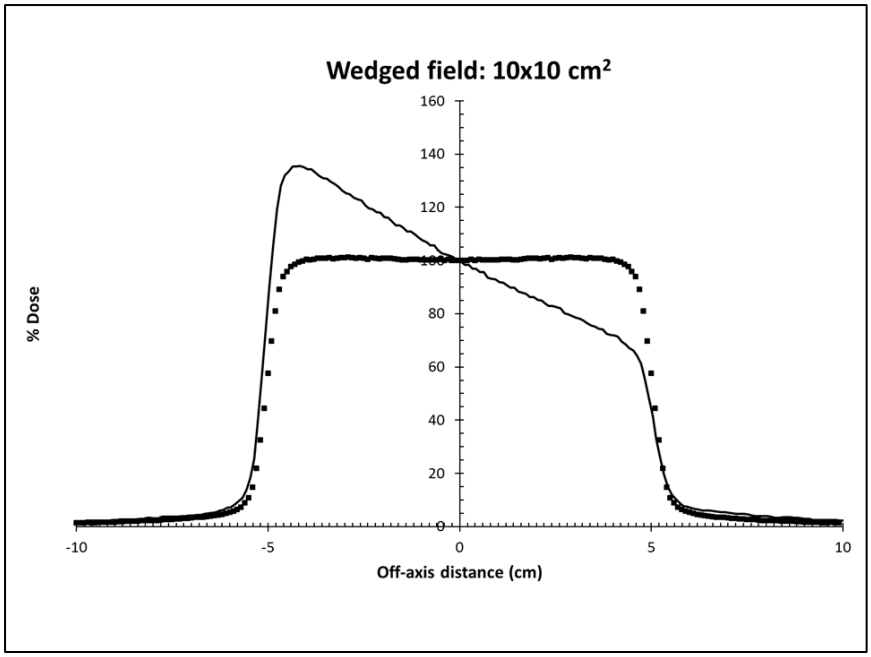

Figure 4-42: Difference in transmission for the regular 10 × 10 cm^2 field (symbols) and the 10 × 10 cm^2 wedged field (solid line) in the inline direction

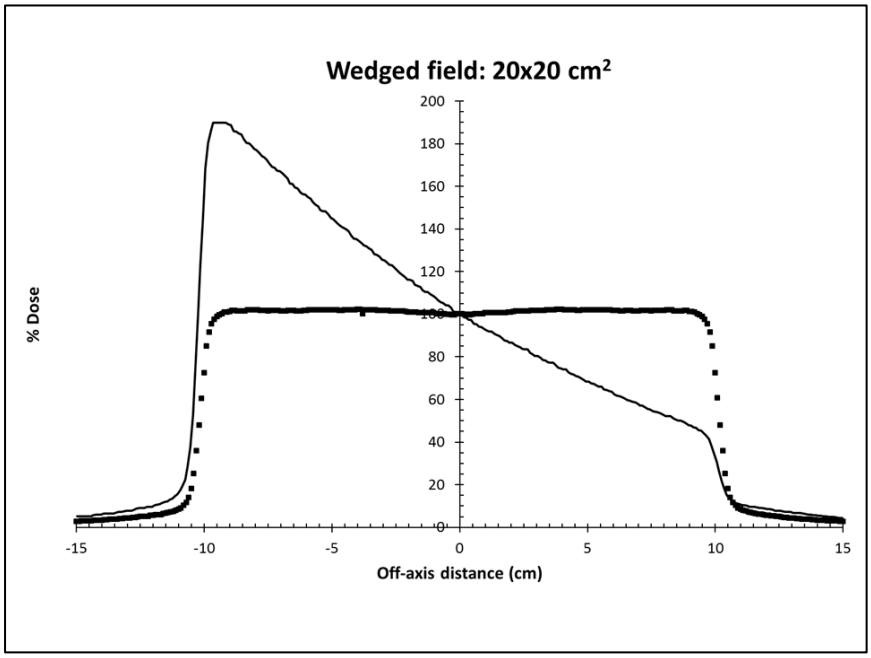

Figure 4-43: : Difference in transmission for the regular 20 × 20 cm^2 field (symbols) and the 20 × 20 cm^2 wedged field (solid line) in the inline direction

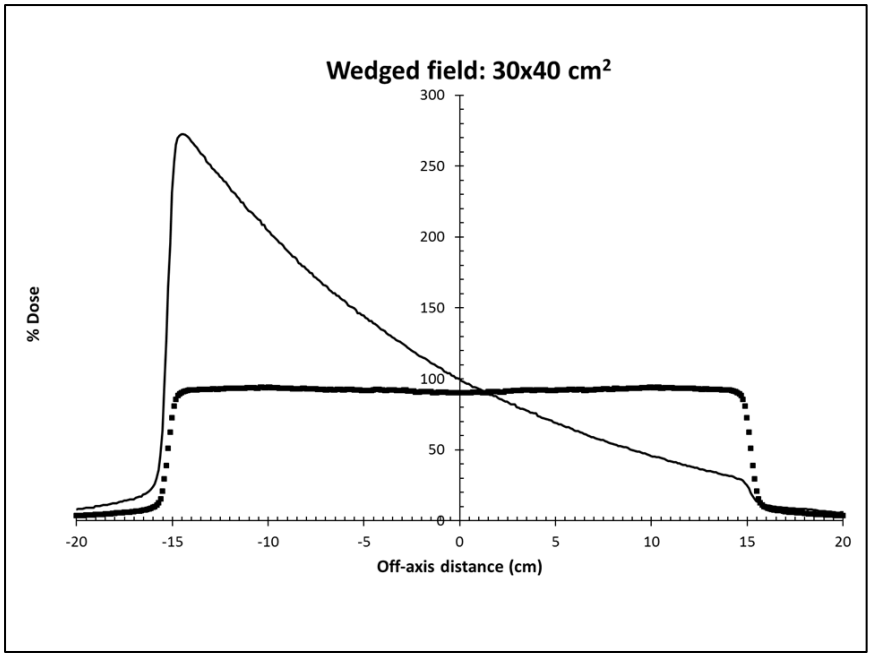

Figure 4-44: : Difference in transmission for the regular 30 × 40 cm^2 field (symbols) and the 30 × 40 cm^2 wedged field (solid line) in the inline direction.

Table 4-3: Parameter values for the wedged fields. The σ value for the MLC x and y is 0.5 and 0.3 over all the fields. The target σ value is 80 for all the wedged fields.

Field size		JAWS					Max photon energy
		X					
		Position	σ	T	mu1	mu2	
10x10	X1	5.12	0.25	0.06	0.1	0.2	7.5
	X2		0.25	0.07	0.1	0.2	
20x20	X1	10	0.25	0.1	0.1	0.2	7.5
	X2		0.25	0.09	0.1	0.2	
30x40	X1	14.9	0.25	0.15	0.1	0.2	7.6
	X2		0.25	0.07	0.1	0.2	

The results for the 10 × 10 cm^2, 20 × 20 cm^2 and 30 × 40 cm^2 wedged fields are shown in Figures 4-45 to 4-48. The gamma index values were below 1 for all the field sizes at the different depths. Different normalization values were used in order to distinguish between the different wedged fields.

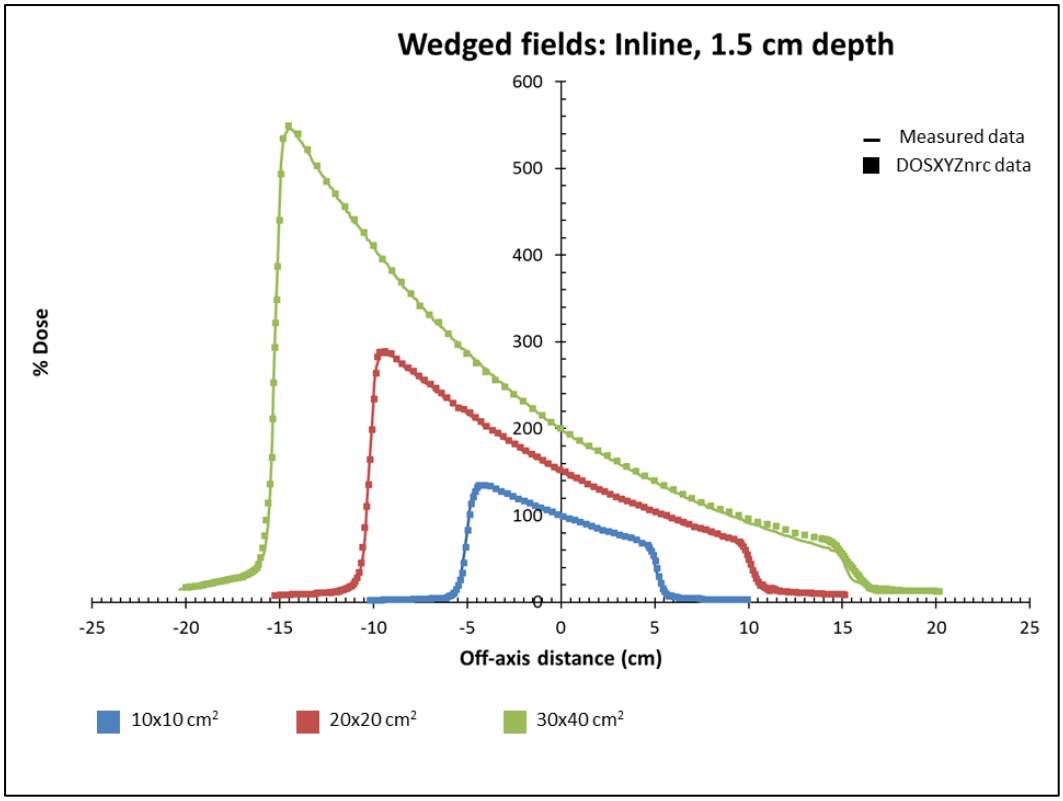

Figure 4-45: Wedged fields in the inline direction at a depth of 1.5 cm.

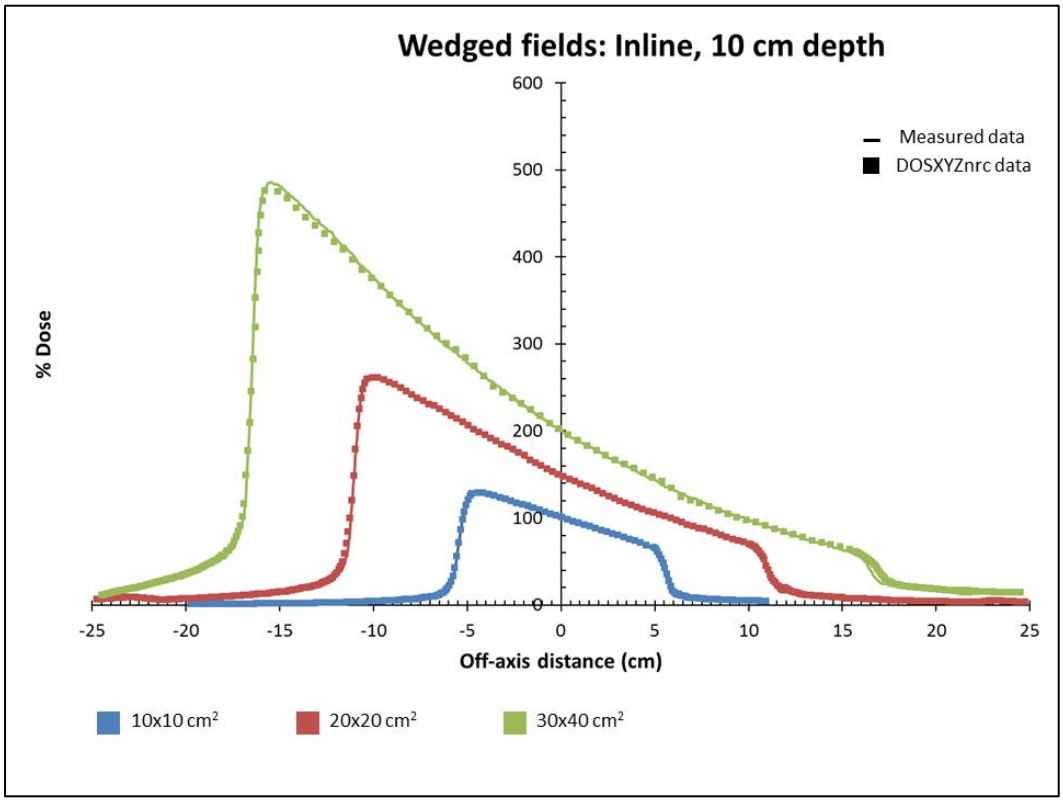

Figure 4-46: Wedged fields in the inline direction at a depth of 10 cm.

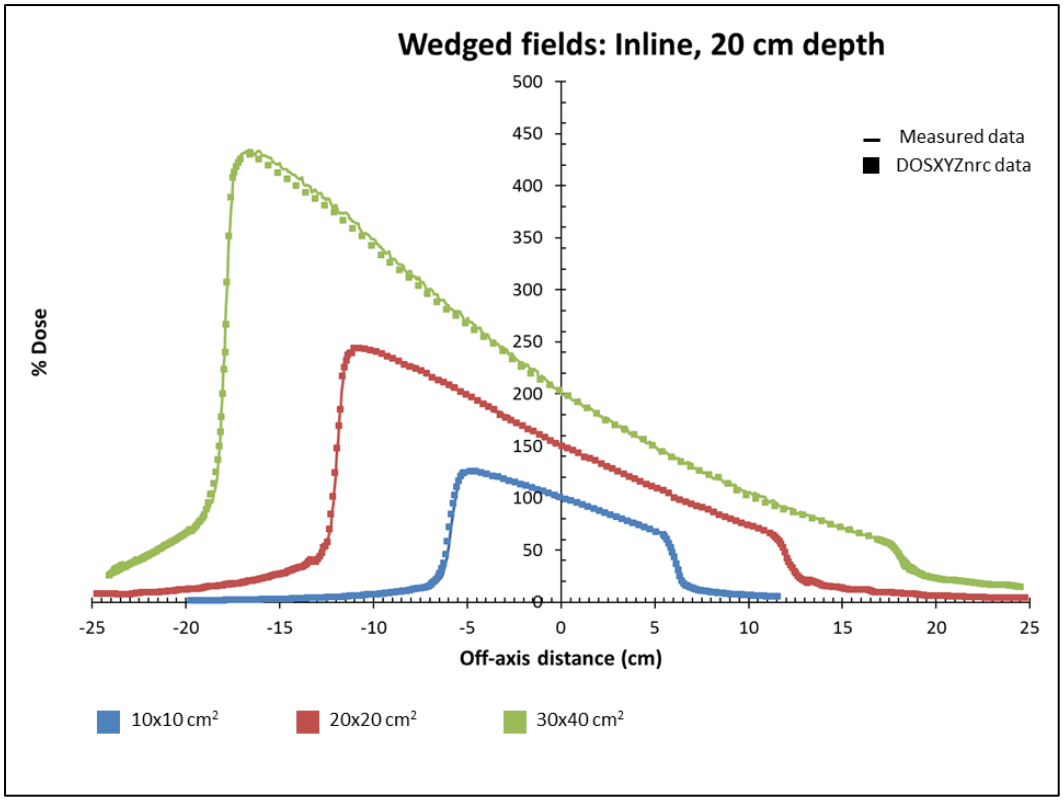

Figure 4-47: Wedged fields in the inline direction at a depth of 20 cm.

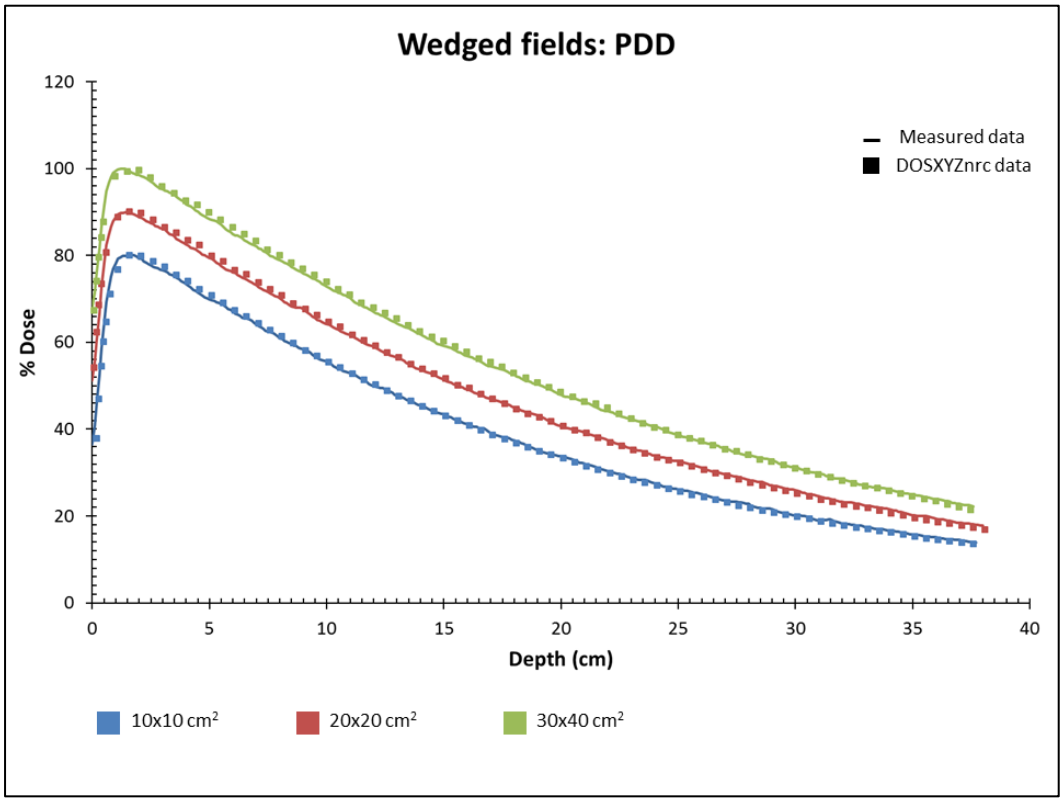

Figure 4-48: Percentage depth dose curves for wedged fields.

4.5 Rectangular fields

Regular field fitting parameters were used to simulate rectangular fields with sizes 5 × 30 cm^2, 30 × 5 cm^2, 10 × 30 cm^2 and 30 × 10 cm^2. There was a difference in the amount of transmission outside the field as a result of the increase in scatter with the changing field size as seen in Figure 4-49 and Figure 4-50. The parameter values for the fields are shown in Table 4-4 and Table 4-5.

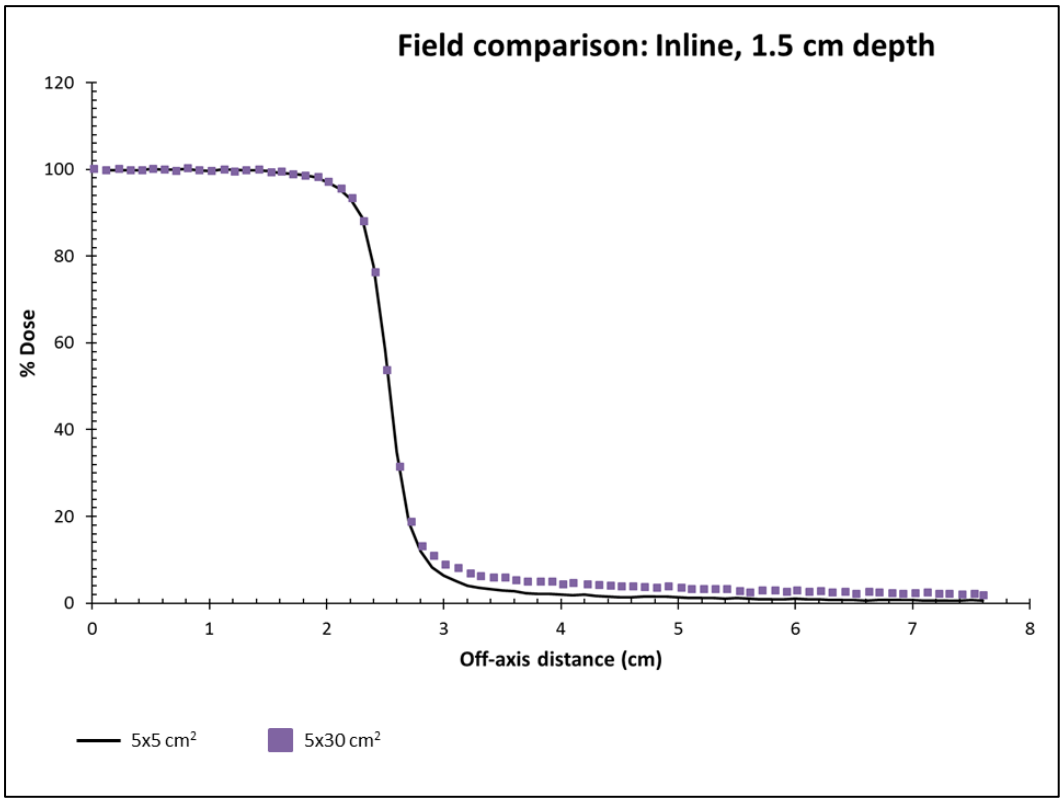

Figure 4-49: The difference in transmission outside the field in the inline direction as a result of the larger total field size.

Table 4-4: Transmission parameter changes for the rectangular field

5x30 cm^2					
Regular fields			Rectangular fields		
Field	X	Y	Field	X	Y
size	T	T	size	T	T
5x5	0.06	0.2	5x30	0.08	0.2
30x30	0.07	0.4			

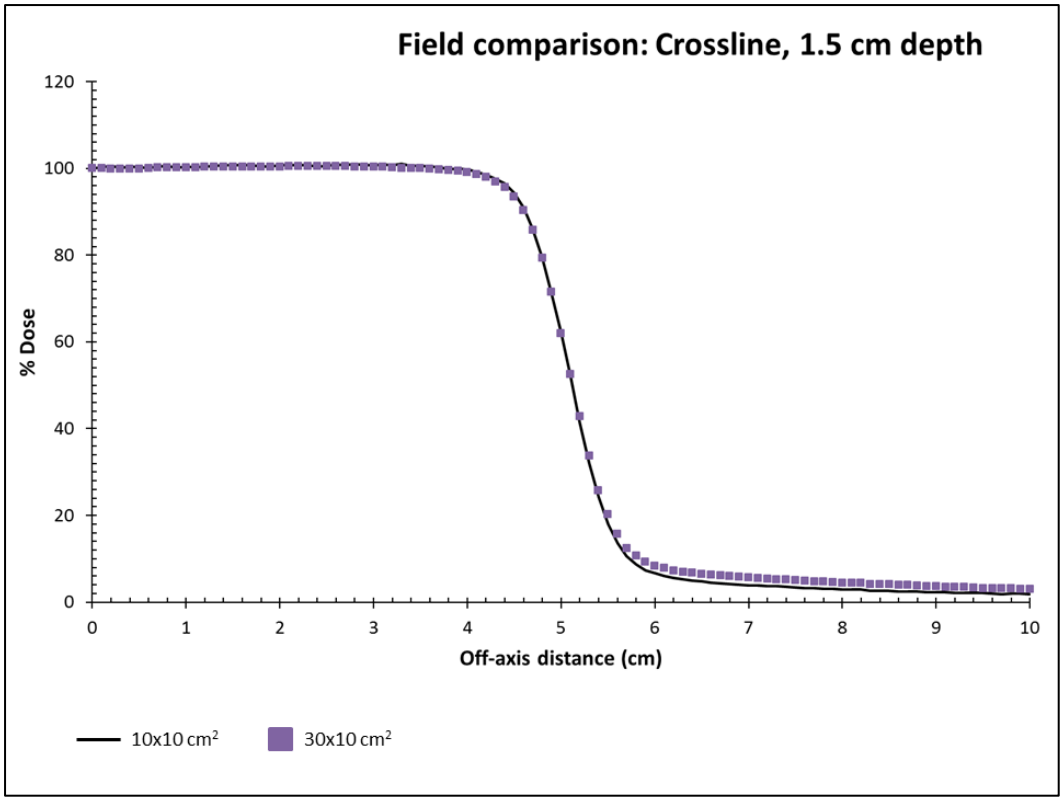

Figure 4-50: The difference in transmission outside the field in the crossline direction as a result of the larger total field size.

The following parameters were used for the rectangular fields in comparison with the regular fields

Table 4-5: Transmission parameter changes for the rectangular field

30x10 cm^2					
Regular fields			Rectangular fields		
Field size	X T	Y T	Field size	X T	Y T
10x10	0.06	0.3	30x10	0.05	0.5
30x30	0.07	0.4			

The results for the rectangular fields are shown in Figure 4-51 to 4-55. The gamma index values were below 1 for all the field sizes at the different depths.

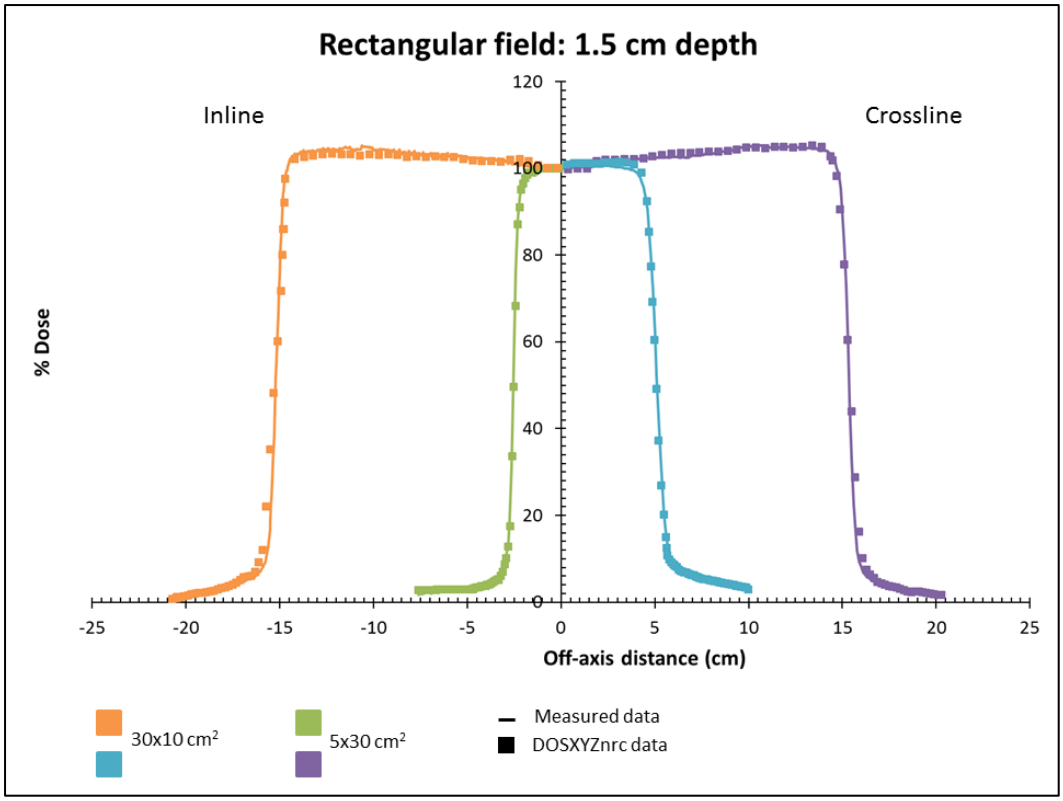

Figure 4-51: Rectangular fields in both directions at a depth of 1.5 cm

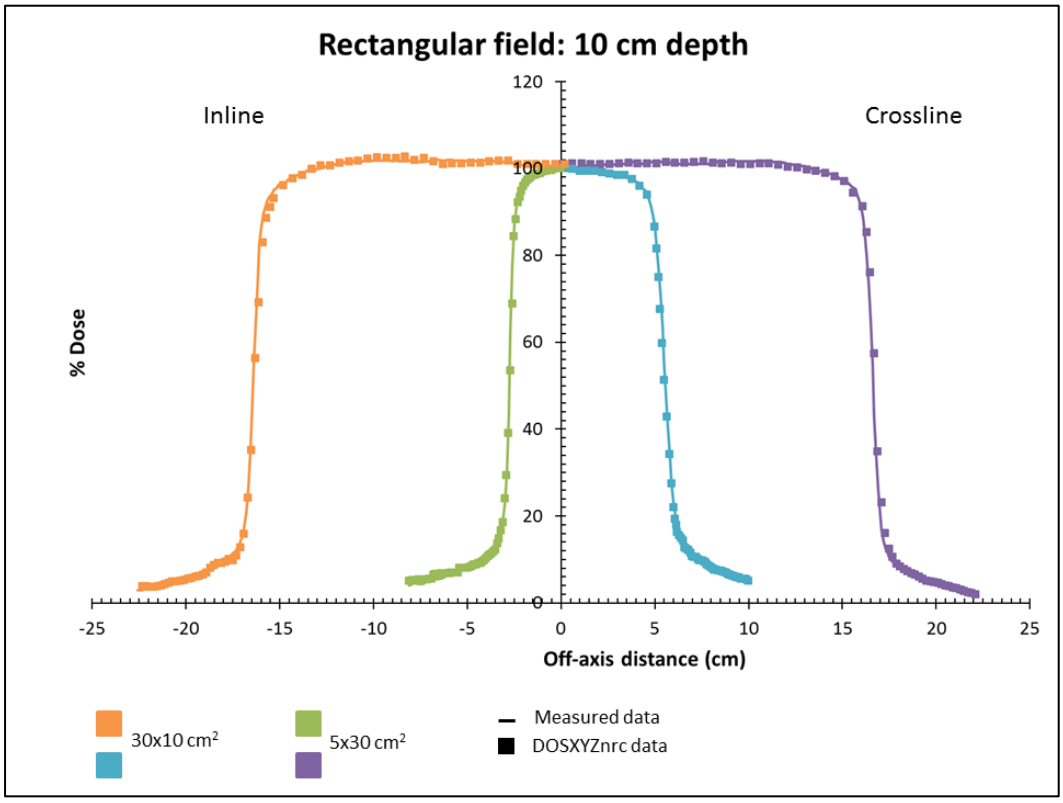

Figure 4-52: Rectangular fields in both directions at a depth of 10 cm

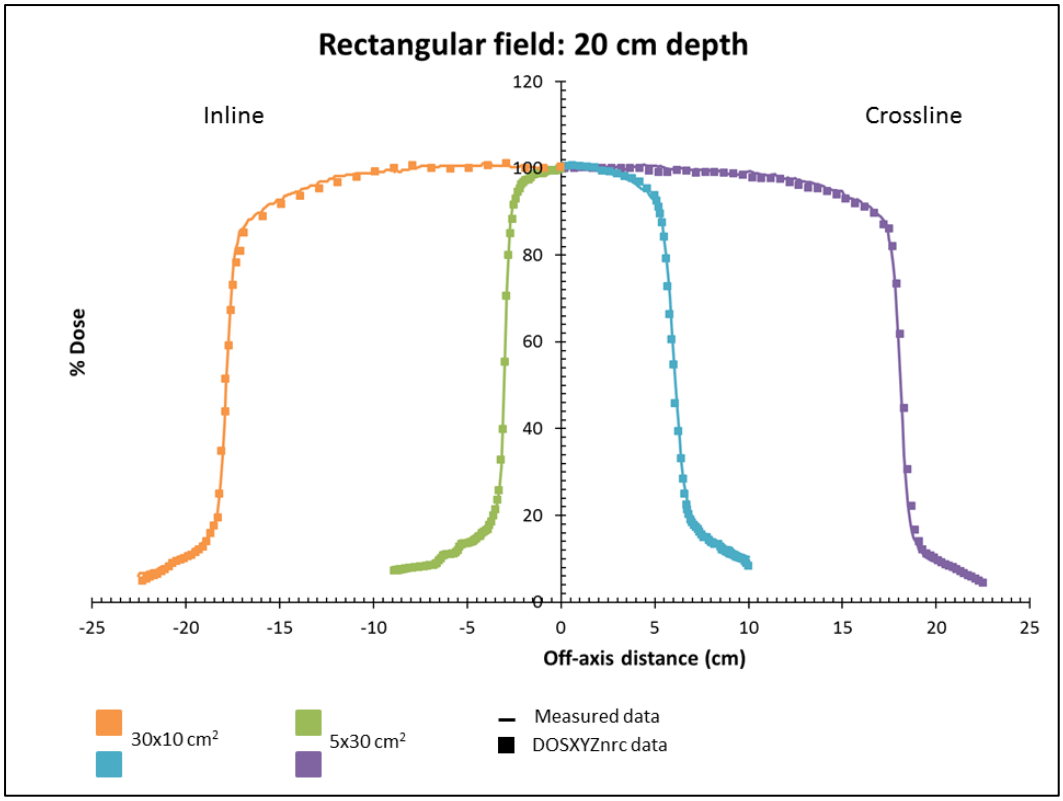

Figure 4-53: Rectangular fields in both directions at a depth of 20 cm

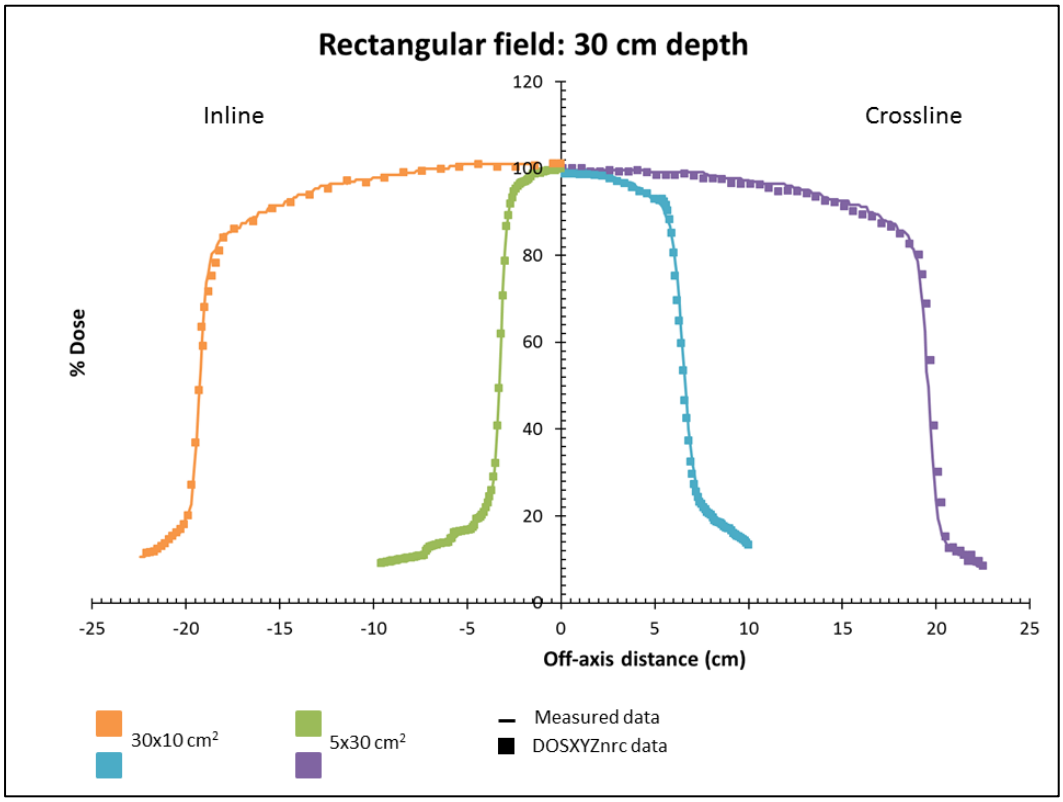

Figure 4-54: Rectangular fields in both directions at a depth of 30 cm

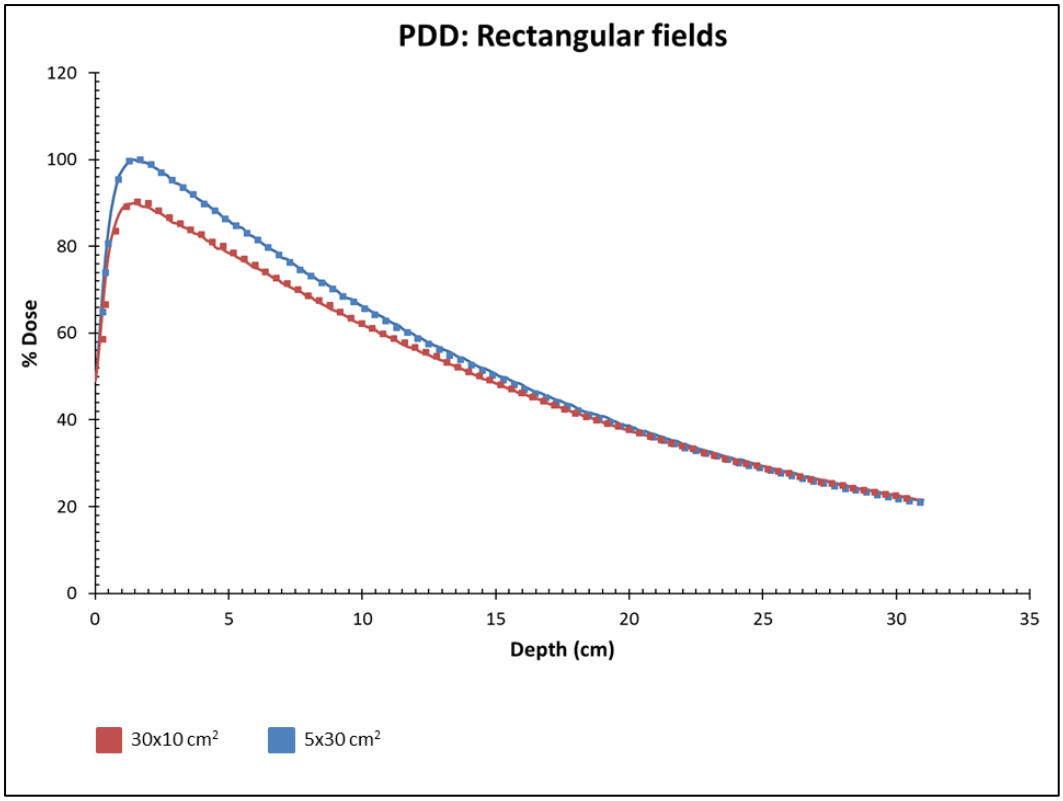

Figure 4-55: Percentage depth dose curves for the rectangular fields.

4.6 Output factors

Machine total output factors were measured on the linac as described in Chapter 3. The same field sizes were simulated with the source model and the dose were obtained. The same parameters were used as with the measurements with a SSD of 100 cm and a depth of 10 cm in water. The voxel size where the dose was acquired was consistent between the different field sizes as this represents the ionization chamber volume when measuring output factors on a linac.

The following dose values were obtained for the different field sizes at the central voxel at a depth of 10 cm:

Table 4-6: Dose values for the different field sizes

Field size	Dose	Histories (Millions)
1x1 cm^2	7.05664E-12	500
2x2 cm^2	1.97438E-12	500
3x3 cm^2	8.58274E-13	500
5x5 cm^2	3.20976E-13	500
10x10 cm^2	7.53977E-14	500
20x20 cm^2	1.63024E-14	500
30x30 cm^2	6.9114E-15	500

It is clear from the above table that the dose decreases as the field size increases. This is not what is expected as the dose is supposed to increase with field size. The problem was investigated by determining if the dose is maybe dependent on the amount of histories. The 1×1 cm^2 field was simulated with different histories and the dose values are seen in Table 4-7.

Table 4-7: The dose values for different amount of histories

Million	Dose
5	7.04817E-12
10	7.05369E-12
20	7.04453E-12
30	7.04385E-12
40	7.03795E-12
50	7.03840E-12
100	7.04358E-12
200	7.04442E-12
300	7.04984E-12

For Table 4-7 it is evident that there is no significant change in the dose between the different amounts of histories. The small changes that do exist are due to the variance of the

dose that is influenced by the amount of histories, $\sigma \propto \frac{1}{\sqrt{N}}$, where N is the number of histories.

It seems that there is some scaling factor between the field sizes that influences the dose in an unexpected manner. This is possibly because a beam characterization model is used and not a full Monte Carlo simulation from the linac head. A method was devised to obtain the correct output factor through a third degree polynomial function. The ratio between the measured output factors and the ones obtained from MC simulations were plotted against the field size in Figure 4-56.

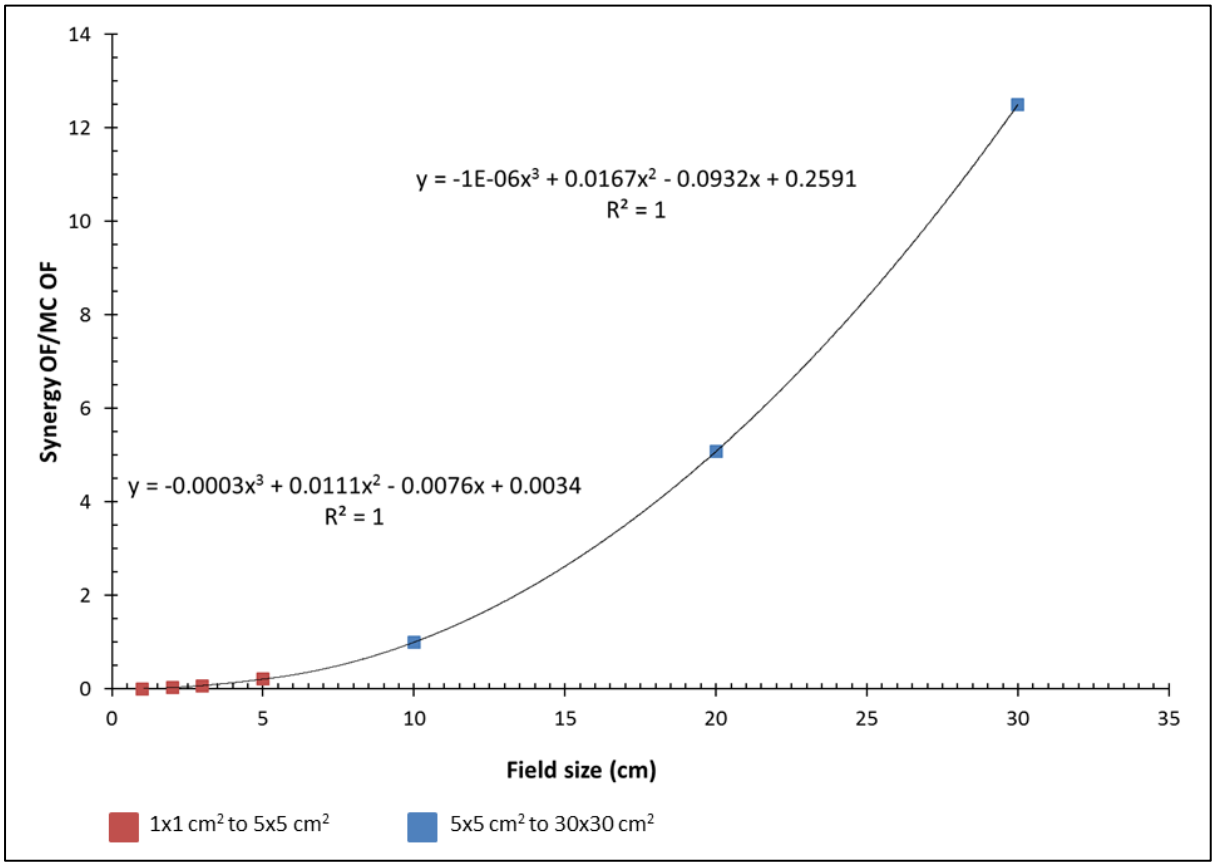

Figure 4-56: A third degree polynomial function fitted to field sizes 1 × 1 cm^2 to 30 × 03 cm^2. The values on the y-axis are the ratios between the measured output factors and the ones obtained from MC simulations.

By using the polynomial function the dose from the simulations could be converted to values corresponding to the correct output factors. Although the correct output factors are

devised the dose in each field still does not represent the true dose that one expects from the simulations. This caused further problems when attempting to use the source model for dose verification as will be discussed later.

The comparison between the measured output factors and the new devised output factors can be seen in Figure 4-57.

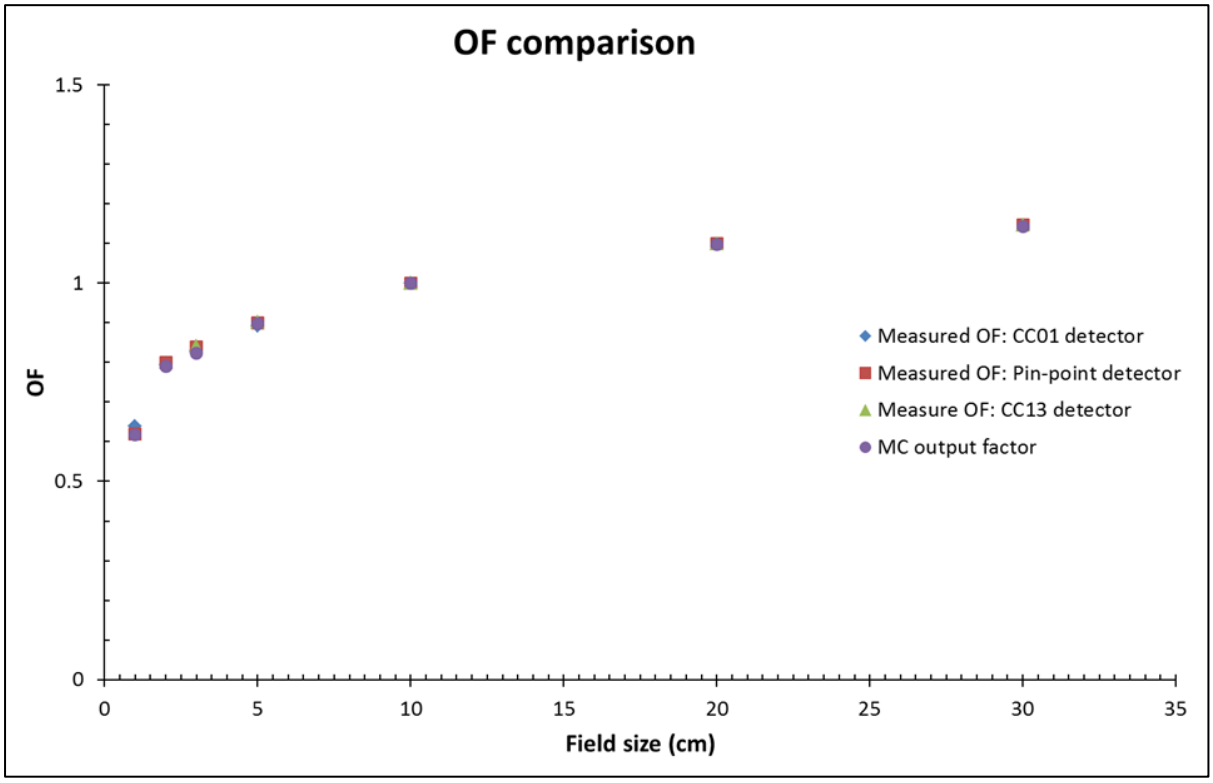

Figure 4-57: Comparison between the measured output factors with three ionization chambers and the ones obtained from Monte Carlo simulations.

Good agreement between the values was obtained after the conversion with the third degree polynomial function.

4.7 Irregular fields

Irregular fields were simulated in a water phantom with 2 mm voxel resolution and enough histories to acquire 1% uncertainty. The dose in the .3ddose files from DOSXYZnrc was converted to the absolute dose using the method explained under Section 3.5.5.2 in

Chapter 3. The reason for this conversion will be discussed later on. The dose was normalized at the isocenter and Equation 3-1 and 3-2 from Chapter 3 were used together with the parameters in Tables 4-8 to 4-10 .

$$Dose(cGy) = MU's \times TMR \times OF \tag{3-2}$$

Where the *TMR* consists of:

$$TMR = F - Factor \times \frac{PDD}{100} \times ISF \tag{3-3}$$

$$F - Factor = \left[\left(\frac{SSD + d_{\max}}{SSD + eff\ depth} \right) \times \left(100 + \left(\frac{eff\ depth}{100 + d_{\max}} \right) \right) \right]^2 \times \frac{PDD}{100} \times ISF \tag{3-4}$$

4.7.1 Oval

Table 4-8: Oval field parameters

MU's (open)	327
MU's (wedge)	0
Wedge Factor	0
MU's (Total)	327
SSD	91.4
Eff depth	8.6
d_{max}	1.5
ISF	1.15869
PDD/100	0.75
F-Factor	0.988
TMR	0.8586
OF	1.05
Dose (cGy)	294.799

4.7.2 C-shape

Table 4-9: Oval field parameters

MU's (open)	338
MU's (wedge)	0
Wedge Factor	0
MU's (Total)	338
SSD	91.4
Eff depth	8.6
d_{max}	1.5
ISF	1.15869
PDD/100	0.744
F-Factor	0.988
TMR	0.85173
OF	1.04
Dose (cGy)	299.399

4.7.3 Squiggle

Table 4-10: Squiggle field parameters

MU's (open)	334
MU's (wedge)	0
Wedge Factor	0
MU's (Total)	334
SSD	91.4
Eff depth	8.6
d_{max}	1.5
ISF	1.15869
PDD/100	0.75
F-Factor	0.988
TMR	0.8586
OF	1.05
Dose (cGy)	301.11

The film pieces were calibrated using the method in Section 3.4 of Chapter 3. One set of calibration films were used for all three the fields. The film strips were irradiated with 38, 75, 150, 300, 390 and 410 MU's at a depth of 5 cm in solid water. The machine output for the particular day was 100 MU = 100.68 cGy. Equation 2-33 and 2-34 of Chapter 2 was used for the calibration of the film pieces. The Solver function in Microsoft Excel 2010 was used to acquire the values for the variables *a*, *b*, and *c*. The following values were obtained:

$a = 0.809434$
$b = -151.555$
$c = -258.766$

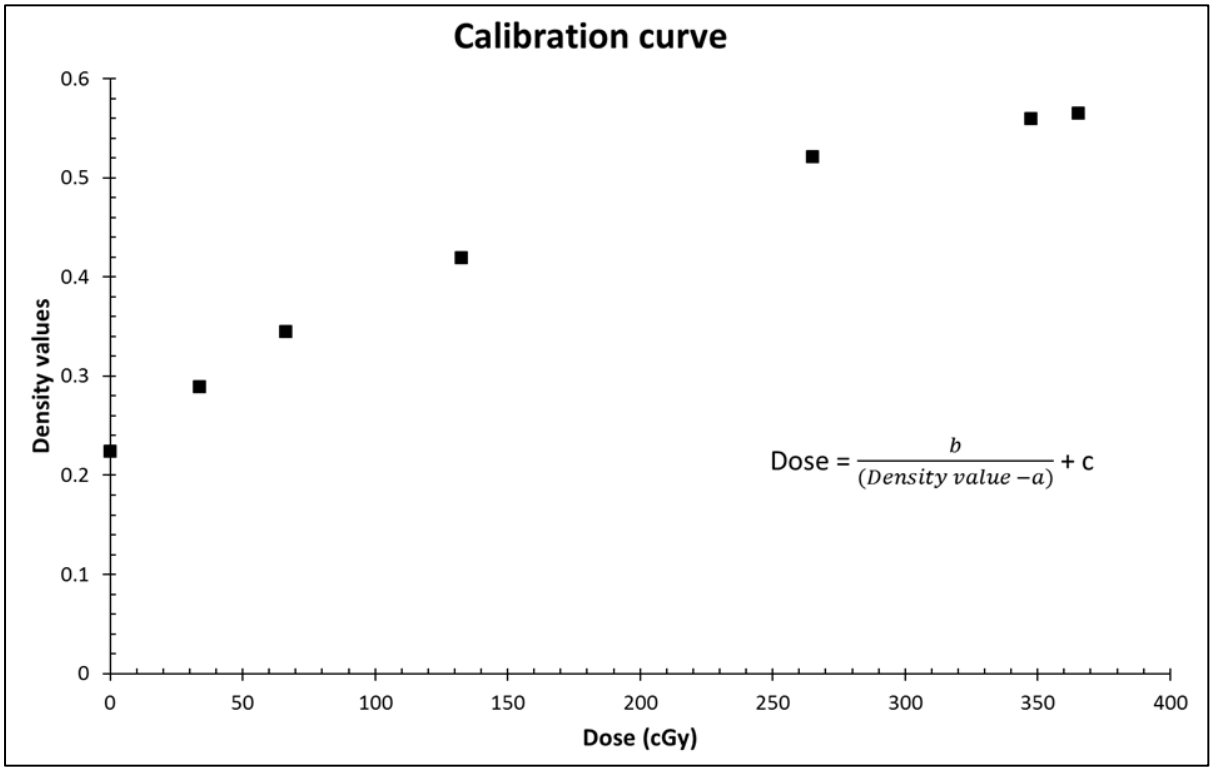

Figure 4-58: Calibration curve for the irregular MLC field shapes

The film and DOSXYZnrc data were normalized to obtain relative dose. The 50% isodose lines of the simulated fields were then compared to those obtained from film to see if the source model can replicate complex field sizes. The results for 5 cm depth and 10 cm depth are shown in Figure 4-59 to 4-61.

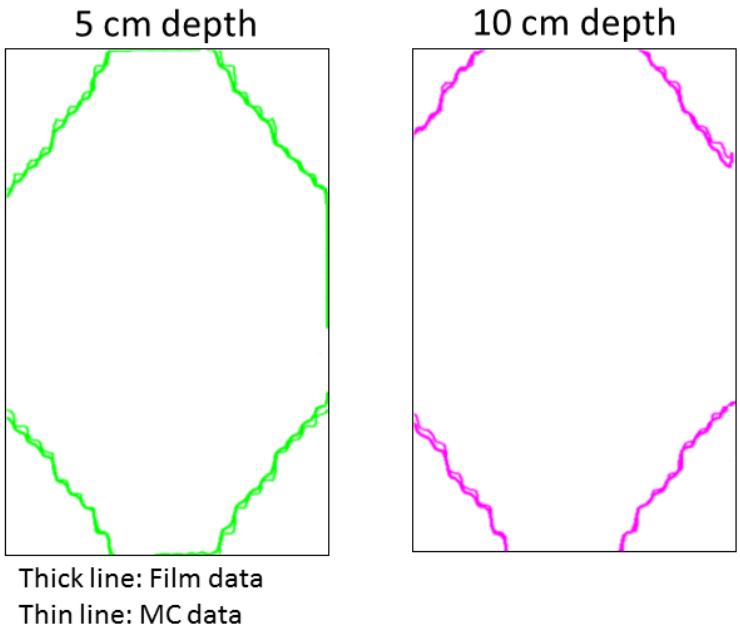

Figure 4-59: Oval field at 5 cm and 10 cm depths. The thick lines represent the film data and the thin lines the MC data.

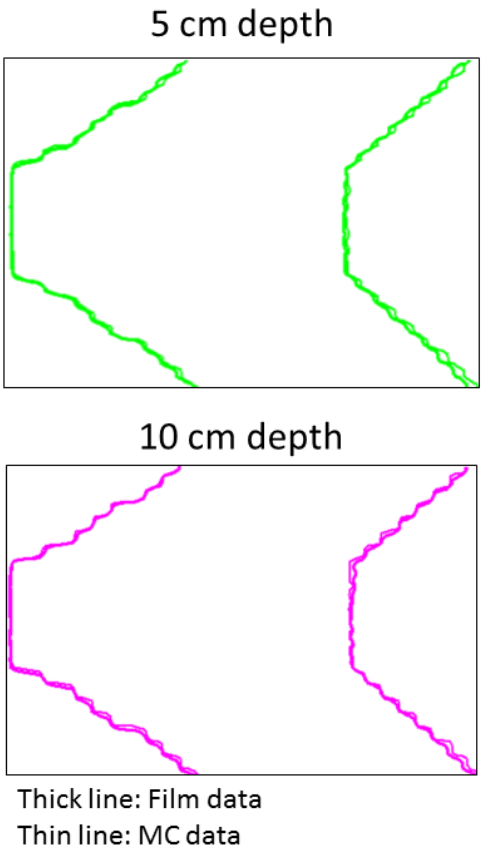

Figure 4-60: C-shape field at 5 cm 10 cm depths. The thick lines represent the film data and the thin lines the MC data.

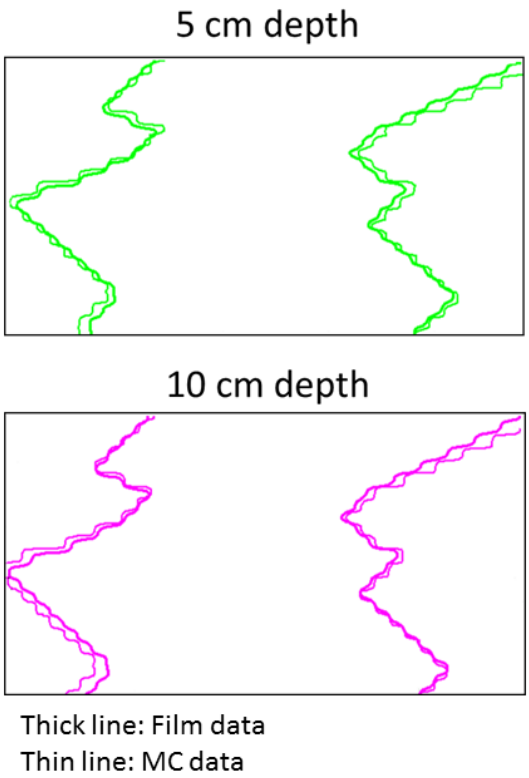

Figure 4-61: Squiggle field at 5 cm and 10 cm depths. The thick lines represent the film data and the thin lines the MC data.

Some discrepancies are seen for the complex squiggle field at 5 cm and 10 cm depths.

4.8 Dose verification

The same method was used for the film calibration and dose conversion as explained in the above Section 4-7. The parameters obtained for the regular fields were used for the simulation of the different treatment sites. The simulation was done with the *.egsphant file acquired for the RANDO® phantom with CTCREATE as described in Chapter 3.

The parameters for each of treatments that were used for the dose conversion are shown below in Tables 4-11-4-13. The same method and equations were used as for the irregular fields in Section 4.7.

4.8.1 Head- and-neck treatment

The simulated and film data were normalized to obtain relative dose. The 100%, 90%, 70%, 50% and 30% isodose lines of the simulated fields were then compared to that obtained from film. The target area is indicated with red in the Figures 4-62 and 4-63 below.

Table 4-11: Head-and-neck treatment parameters for the two fields

	Field 1	Field 2
MU's (open)	0	256
MU's (wedge)	427	0
Wedge Factor	0.257	0
MU's (Total)	109.739	256
SSD	95	94.1
Eff depth	5	5.9
d_{max}	1.5	1.5
ISF	1.07385	1.09417
PDD/100	0.87	0.814
F-Factor	0.99655	0.99489
TMR	0.93103	0.8861
OF	0.97	0.95
Dose (cGy)	99.1057	215.5

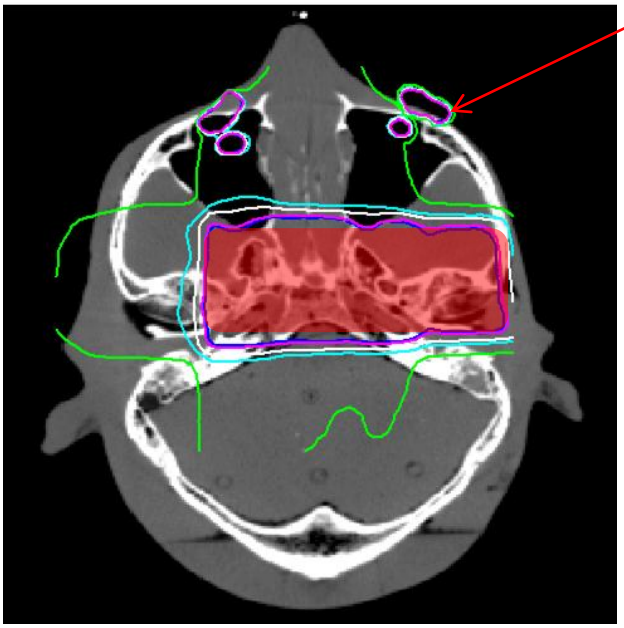

Figure 4-62: Isodose lines obtained from the film. The red arrow indicates where markings were made on the film that resulted in high doses. It can be ignored when doing the comparison between the two sets of data

.

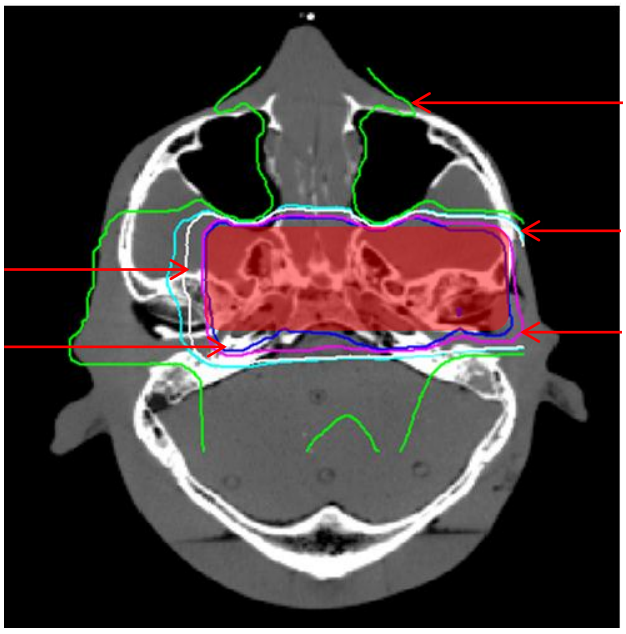

Figure 4-63: Isodose lines obtained from DOSXYZnrc. No dose was scored in the air cavities.

Good correlation was found for the doses inside the bone and tissue regions. No dose was scored in the air cavities or outside the phantom for the MC simulation which lead to some discrepancies for the low doses such as 30% and 50%. The best results were obtained for the 90% isodose lines (magenta) where the differences are insignificant.

Figure 4-64 is an example of dose scored in air during the simulation of the head-and-neck treatment. The highest dose is scored outside the phantom which leads to an unrealistic comparison between the simulated and film data.

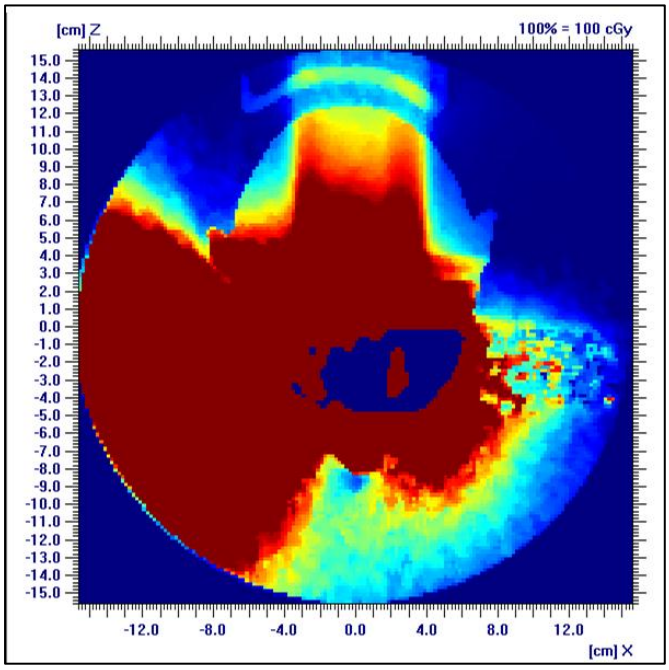

Figure 4-64: The head-and neck treatment simulation with dose scoring in the air regions.

4.8.2 Abdomen treatment

The simulated and film data were normalized to obtain relative dose. The 120%, 100%, 90%, 70%, 50% and 30% value isodose lines of the simulated fields were then compared to those obtained from the film for relative dose comparison.

The following treatment parameters were used for the abdomen treatment.

Table 4-12: Abdomen treatment parameters for the four fields

	Field 1	Field 2	Field 3	Field 4
MU's (open)	179	174	0	0
MU's (wedge)	0	0	805	790
Wedge Factor	0	0	0.263	0.263
MU's (Total)	179	174	211.715	207.77
SSD	89.1	89.9	85.1	85.5
Eff depth	10.9	10.1	14.9	14.5
d_{max}	1.5	1.5	1.5	1.5
ISF	1.21827	1.19704	1.33341	1.32118
PDD/100	0.623	0.648	0.495	0.501
F-Factor	0.97991	0.98296	0.96105	0.9632
TMR	0.74374	0.76246	0.63433	0.63755
OF	0.95	0.95	0.95	0.95
Dose (cGy)	126.472	126.035	127.582	125.841

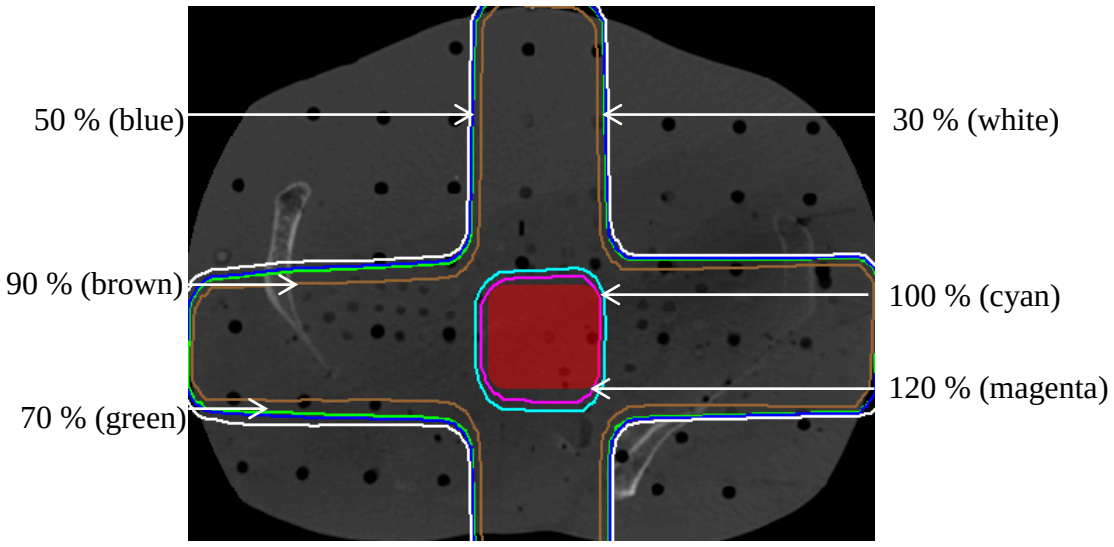

Figure 4-65: Isodose lines obtained from the film.

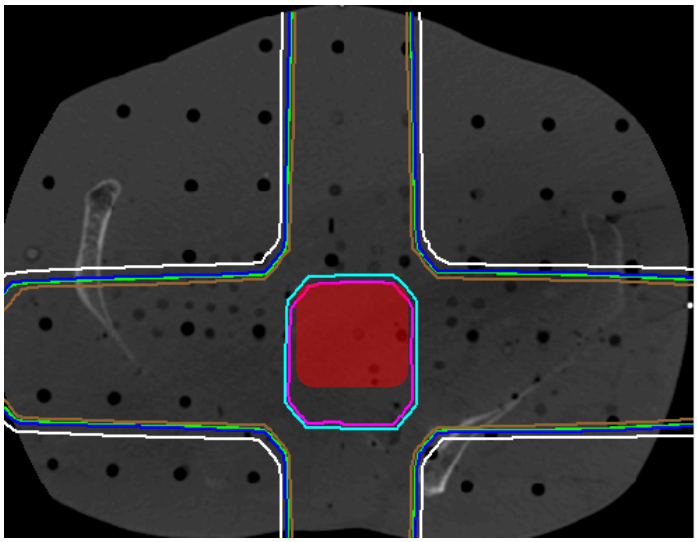

Figure 4-66: Isodose lines obtained from DOSXYZnrc.

This treatment is in an area of soft tissue and no difficulties are expected for the conversion with CTCREATE. Small differences can be seen between the 120% (magenta) and 100% (turquois) isodose lines for the two sets of data. Good coverage of the target area is seen for both cases although a high dose region exists outside the target area for the simulated data. Insignificant differences are seen for the 70%, 50% and 30% isodose lines.

4.8.3 Chest treatment

The simulated and film data were normalized to obtain relative dose. The 120%, 100%, 90%, 70 isodose lines of the simulated fields were then compared to those obtained from the film for a relative dose comparison.

Table 4-13: Chest treatment parameters for the three fields

	Field 1	Field 2	Field 3
MU's (open)	300	253	253
MU's (wedge)	0	0	0
Wedge Factor	0	0	0
MU's (Total)	300	253	253
SSD	88.9	84.7	84.8
Eff depth	11.1	15.3	15.2
d_{max}	1.5	1.5	1.5
ISF	1.22367	1.34582	1.3427
PDD/100	0.544	0.467	0.472
F-Factor	0.97911	0.95883	0.95939
TMR	0.65177	0.60262	0.60802
OF	0.84	0.94	0.94
Dose (cGy)	164.246	143.315	144.598

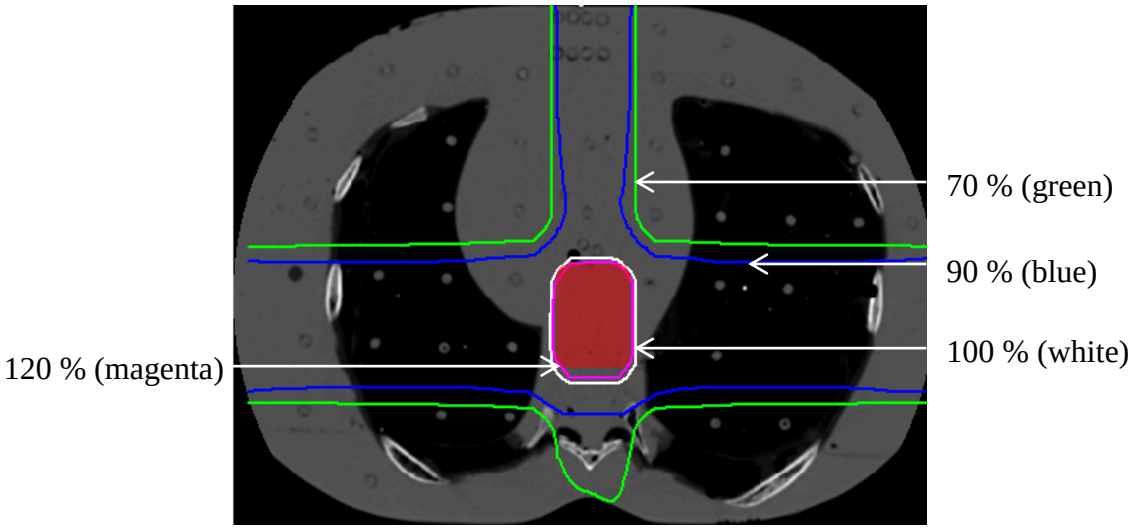

Figure 4-67: Isodose lines obtained from the film

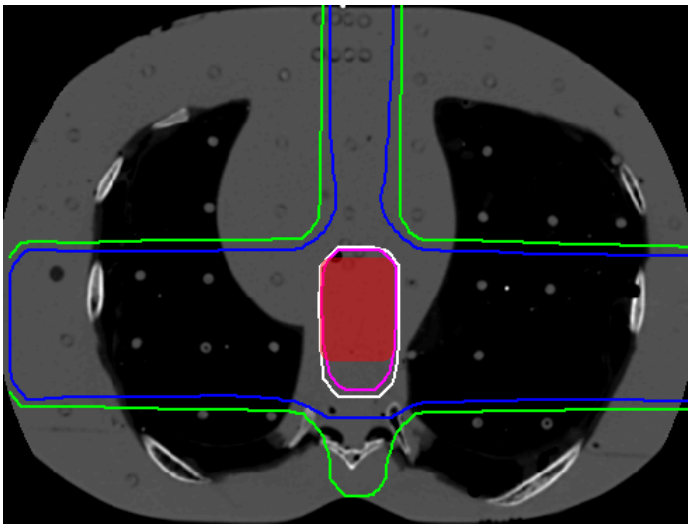

Figure 4-68: Isodose lines obtained from DOSXYZnrc

The high dose region for the simulated data resulted in a slightly elongated shape. MC is known for its accuracy in inhomogeneity regions such as the lung and this discrepancy can be due to the density conversion in CTCREATE. Inaccuracies in the densities of the *.egsphant file used for the simulation can result in dose differences.

4.9 Discussion

The target, primary collimator and flattening filter fluence were accurately modelled and benchmarked against Monte Carlo simulations. The least square fit method was adequate for determining the optimal σ value for the target fluence. The modified Schiff formula accurately modelled the bremsstrahlung energy spectrum originating at the target, as can be seen from PDD dose comparison.

The source model was found to be useful over a wide range of field sizes ranging from a 1×1 cm^2 to a 40×40 cm^2 regular field. The error function is useful to model the slope of the penumbra region. The transmission outside the field could be accurately modelled with an exponential function.

The largest discrepancies were found in the penumbra region as well as outside the field for regular as well as offset fields. The σ values for the error function of the jaws followed a trend between the field sizes. By having random σ values for each field size is not practical or scientific. Interpolation between field sizes would then be impossible for future use. All the gamma index values for the field sizes were below 1, satisfying a gamma criterion of 2 % /2 mm. The regular field sizes showed good agreement between the two sets of data and it can be said that the MC source model is accurate in modelling these fields.

The offset fields exposed the shortcomings of the source model in terms of the amount of sources that are used. Although the single source proved to be accurate for regular fields it is not adequate for offset fields. Most source models consist of multiple sources including an extrafocal source or a source to introduce scatter. An exponential function was used to modify the fluence to replicate the effect of an extra source and introducing scatter. By including an extra source offset fields could be modelled more accurately.

In our approach, regular field parameters were used for offset fields. The gamma index values were below 1 although some discrepancies were found. The fields that were completely offset e.g. 10×10 cm^2 field with a 10 cm offset, showed large discrepancies in the penumbra region on the central axis. This is due to the fact that the 1×1 cm^2 field's σ value was used to simulate the field edge on the central axis. The amount of scatter was not consistent between the regular fields and the offset fields and alterations to the fluence parameters were needed. This was also not necessary for all of the offset fields.

An exponential function was used to replicate the attenuation by the wedge. Different fluence model parameter values were used for the jaws and transmission in comparison with that used for regular fields. The same value was used for the exponential function describing the wedge. The 10×10 cm^2 and the 20×20 cm^2 wedged fields showed better correlation to the measured data than the larger field of 30×40 cm^2. Using a different parameter value for

the exponential function might result in less inconsistency in comparison with the measured data. The exponential function proved to be a valid method to model the wedged field profiles. By finding the correct parameter values this function can be used for various field sizes. The energy spectrum differs from the ones obtained with regular fields as one would expect.

The parameter values for the jaws can be altered independently. This source model can be used to model rectangular fields in both directions adding to the versatility. The transmission parameters were altered for the rectangular fields as a result of the change in the amount of scatter due to the field size. The σ values for the jaws and MLC's stayed constant in the comparison between regular fields as expected. Results showed that source model based dose data is accurate in modelling rectangular fields.

The percentage depth dose (PDD) curves resulted in large discrepancies in the build-up region. Dose measurements with ionization chambers are not accurate in this region due to electron disequilibrium. The discrepancies can therefore be as a result of the water tank acquisitions rather than a shortcoming in the source model. The option still exists to add electron contamination to further improve the results. The PDD curves showed good agreement for all the fields with changes in the maximum energy as the field size changed. The gamma index values were below 1 for all the fields simulated in this study. With the GUI it is easy to adjust the electron energy to obtain a comparable percentage depth dose curve.

The GUI models each MLC leaf independently making it suitable for irregular MLC field modelling. Although the source model is not adequate for absolute dose comparison it can still mimic the field shapes of complex configurations.

The dose verifications resulted in some discrepancies with the major drawback being the inability to compare absolute dose. For the head- and- neck treatment differences were

observed in the air cavities due to the fact that the MC simulations did not score dose in these regions.

The abdomen treatment consisted of a uniform area and the results compared well with one another. Small difference in the 120% and 100 % isodose lines can be seen with no significant differences in the low dose region. Similar results were obtained for the chest treatment. Some of the differences can be due to the fact that the densities were not converted properly with the CTCREATE software. A change in the ramp filter used for these CT slices could correct some of the discrepancies. The method used for the dose conversion from DOSXYZnrc can also result in errors as well as the calibration of the film. This source model cannot be utilized for complex treatment modalities such as IMRT but is suitable for conformal fields.

5. CHAPTER 5: CONCLUSION

In this study we used a GUI-based MC source model refiner code that we developed in-house. The source model can replicate x-ray beams emanating from an Elekta Synergy linear accelerator. The model uses a single point source and collimation scatter is adjusted through fluence profile modelling using error functions. This is done instead of adding more sub sources to the model. If electron contamination is to be included, another point source is introduced at an effective SSD. Agreement with water tank beam data was tested for percentage depth dose curves, square fields, offset fields, rectangular fields and wedge fields and was within 2% / 2 mm. Dose verification was done using film and an anthropomorphic phantom for three different treatment sites.

It is important to accurately model the different beam scattering components of the linear accelerator in order to obtain the same results as those from benchmarking water tank scans. This was made possible by developing a graphical user interface that can be used to tweak the modelling parameters of the source model and to show its effect on the exit fluence. The GUI is user friendly and simplifies setting up the source model. The graphical plots of exit fluence aid the user in adjusting the correct parameters to obtain the required dose accuracy results. The resulting input file is ready to be used with DOSXYZnrc to obtain dose distributions in phantoms. The GUI can be utilized for different linear accelerators and more than one photon energy. It has proved to be a valuable tool for fast setting of beam fluence parameters for the source model.

The least-squares method was a valid technique for determining the correct σ value for the primary target fluence which was set for all fields. The flattening filter model accounted for the attenuation of dose accurately on the CAX for all the field sizes. The primary collimator

parameter values were kept constant between the field sizes, using one set of σ and transmission values.

For regular fields the largest gamma index value was for the 40 × 40 cm^2 field for the crossline profile at 20 cm and 30 cm depths. This means that there is either a 2% dose difference between two data points at the same off-axis distance or that there is a 2 mm distance-to agreement between two data points. Such a large field is rarely used clinically. Interpolation between field parameters is possible to acquire the suitable values for e.g. a 7 × 7 cm^2 field or a 12 × 12 cm^2 field. All of the field sizes as well as their percentage depth dose curves showed good agreement with water tank measurements.

For the offset fields an exponential function had to be included to account for the lack of scatter at the periphery of the field. This showed that a single source is not suitable to model all types of fields and an extra source has to be included. The method used in this study was valid although it is not the most feasible method to use. The same parameters were used as for the regular fields, with additional alterations to the amount of transmission outside the field. This is the result of unequal amounts of scatter from the jaw surfaces because the field is not centred over the CAX.

The exponential function used for the wedged fields accurately models the attenuation of the fluence. The same parameters were used as in the case of the regular fields but there were an increase in the scatter parameter outside the field as a result of the wedge insert. The largest discrepancies were seen for the large 30 × 40 cm^2 wedged field with gamma index values close to 1. An increase in the electron energy is seen for the percentage depth dose curves due to the increase in scatter on the CAX.

The source model was also tested for rectangular fields and showed good agreement with the water tank data. The regular field parameters were used for the different size fields with adjusted transmission parameters.

A big disadvantage is the source's inability to produce realistic output factors. Absolute dose comparisons were not possible for dose verification and relative dose comparisons were done. The dose was converted with treatment planning parameters to obtain the normalized dose of the simulation. For the irregular MLC fields the field shapes were compared between the two sets of data. The good correlation shows that the source model can replicate complex conformal field shapes. For the dose verification good correlation was found between the simulated and film data with differences in in the high dose regions. Dose was not scored in air for the head-and-neck treatment which resulted in differences upon comparison with film data. Differences were found in the high dose regions for the abdomen and chest treatments.

This study have shown that the source model can accurately model open fields of different sizes as well as their associated percentage depth dose curves. The Schiff-based energy spectra produce photons that can replicate PDD data. Irregular field shapes can be reproduced with the source model and relative dose comparisons are possible with film and suitable phantoms.

6. CHAPTER 6: SUMMARY

6.1 Summary

In oncology patients are treated for cancer with various methods such as surgery, chemo therapy and radiation therapy. Accurate radiation treatment planning and dose delivery to the tumour is necessary for the successful outcome of cancer treatment. In order to achieve this goal accurate radiation dose calculation codes must be utilized. EGSnrc based Monte Carlo (MC) codes such as BEAMnrc and DOSXYZnrc have been developed for just this purpose. The problem that arises in using these MC codes is that they lack suitable x-ray beam source models. These models must be accurate in order to replicate the true clinical x-ray beam emanating from the linear accelerator. One such machine for which radiation source data must be derived is currently being used at the Oncology department in Universitas Hospital Annex. It is desirable to model this linear accelerator in order to perform MC based dose calculations for radiation treatment.

The use of MC based dose calculations is certainly not new in the radiation physics environment. Various authors have studied the replication of radiation beam characteristics using source models to simulate the phase-space parameters of particles produced by the linear accelerator. These parameters include the charge, energy, direction, and position of each particle as it crosses a certain reference plane below the linear accelerator. An accurate source model should be able to re-generate particles with the exact set of above-mentioned parameters as would be produced by the real linear accelerator. Sources can be very simple such as a single point from which the particles are radiating with a single invariant energy spectrum. Studies have shown that these beam models can yield accurate beam data over

relatively small field sizes and is not general enough to use over a whole range of clinically useful field sizes.

A graphical user interface (GUI) was developed that can assist in the construction of the source model. The source model can describe energy and fluence distributions for photons and electrons as separate point sources each with their own SSD. The accuracy of the model was validated by comparing simulated profiles with measured data for an Elekta Synergy linear accelerator.

The modified Schiff formula was used to derive the bremsstrahlung spectra emanating from the target. The x-ray fluence Gaussian distribution consisted of the primary fluence from the target, which was modified by the primary collimator, secondary collimators as well as the multileaf collimators. The truncation and beam scatter caused by the face of the collimators were modelled with error functions. Exponential functions were used to model off-axis collimator transmission.

Profiles and percentage depth dose curves were obtained with the source for square field sizes of 1×1 cm^2 up to a 40×40 cm^2. Offset fields for 10×10 cm^2, 15×15 cm^2 and 20×20 cm^2, rectangular fields as well as wedged fields were included. Irregular field shapes were simulated to evaluate the source model's capability of reproducing complex treatment fields. Film dose verification was done in an anthropomorphic Rando® phantom and compared with the MC source model for 6 MV x-ray beams. A criterion of 2% / 2 mm was used to compare MC data and measured data.

This study demonstrated that a diversity of field sizes and percentage depth dose curves can be modelled within 2% / 2 mm. The model can replicate irregular field sizes used for complex treatments. Minor discrepancies were found for the relative dose comparisons between the MC and film data for the anthropomorphic phantom.

Key words: graphical user interface, source model, Monte Carlo, DOSXYZnrc, gamma criteria, dose verification, linear accelerator, Schiff formula, radiation dose calculations, cancer therapy.

6.2 Opsomming

In onkologie word pasiënte behandel vir kanker met verskillende metodes soos chirurgie, chemoterapie en bestralings terapie. Akkurate bestralings beplanning en gelewerde dosis aan die tumor is noodsaaklik vir die suksesvolle uitkoms van die behandeling van kanker. Ten einde hierdie doel te bereik moet akkurate bestralings dosis berekening kodes gebruik word. EGSnrc gebaseerde Monte Carlo (MC) kodes soos BEAMnrc en DOSXYZnrc is ontwikkel vir hierdie doel. Die probleem wat ontstaan in die gebruik van hierdie MC kodes, is hulle gebrek aan geskikte x-straal bron modelle. Hierdie modelle moet akkuraat wees om die ware kliniese x-strale vanuit die lineêre versneller te herhaal. Een so 'n masjien waarvoor bestralings bron data afgelei moet word, word tans gebruik by die Onkologie-afdeling in Universitas Annex Hospitaal. Dit is wenslik om hierdie lineêre versneller te modelleer om MC gebaseerde dosis berekeninge uit te voer vir bestraling.

Die gebruik van MC gebaseerde dosis berekeninge is beslis nie nuut in die mediese fisika gebied nie. Verskeie outeurs het die herhaling van bestralings eienskappe met behulp van bron-modelle met fase-ruimte parameters van deeltjies wat deur die lineêre versneller beweeg gebestudeer. Hierdie parameters sluit in die lading, energie, rigting, en die posisie van elke deeltjie by 'n sekere verwysings vlak onder die lineêre versneller. 'N akkurate bron model moet in staat wees om deeltjies te her-skep met die presiese stel van bogenoemde parameters soos geproduseer sal word deur die werklike lineêre versneller. Bronne kan baie eenvoudig wees soos 'n enkele puntbron van waar die deeltjies uitstraal met 'n enkele onafhanklike energie spektrum. Studies het getoon dat hierdie bundel modelle akkurate bundel data kan

oplewer oor relatief klein veld groottes en is nie algemeen genoeg om te gebruik oor 'n hele reeks van klinies bruikbare veld groottes nie.

'N grafiese gebruikerskoppelvlak is ontwikkel wat kan help met die bou van die bron model. Die bron model kan energie en vloed distribusies vir fotone en elektrone beskryf as afsonderlike punt bronne, elk met hul eie FVA. Die akkuraatheid van die model is bevestig deur gesimuleerde profiele te vergelyk met gemete data vir 'n Elekta Synergy lineêre versneller.

Die gemodifiseerde Schiff formule is gebruik om die bremsstrahlung spektrum afkomstig van die teiken, af te lei. Die x-straal vloed Gaussiese verspreiding bestaan uit die primêre vloed van die teiken, wat aangepas is by die primêre kollimator, sekondêre kollimators sowel as die multispleet kollimatore. Die vernouiing en bundel verstrooiing wat veroorsaak word deur die oppervlakte van die kollimators is gemodelleer met erfunksies. Eksponensiële funksies is gebruik om asimmetriese kollimator verstrooiing the modelleer .

Profiele en persentasie diepte dosis kurwes is verkry met die bron vir vierkantige groottes van 1 x 1 cm^2 tot 'n 40 × 40 cm^2. Asimmetriese velde van 10 × 10 cm^2, 15 × 15 cm^2 en 20 × 20 cm^2, reghoekige velde asook wig velde was ingesluit. Onreëlmatige veld groottes is gesimuleer om die bron model se vermoë van die kopiëring van komplekse behandeling velde te evalueer. Film dosis verifikasie is in 'n antropomorfiese Rando® fantoom gedoen en is vergelyking met die MC bron model vir 6 MV x-straal bundel. 'N maatstaf van 2% / 2 mm is gebruik om die MC data en gemete data te vergelyk.

Hierdie studie het getoon dat 'n verskeidenheid van veld groottes en persentasie diepte dosis kurwes binne 2% / 2 mm gemodelleer kan word. Die model kan onreëlmatige veld groottes herhaal wat gebruik word vir komplekse behandelings. Geringe verskille is gevind vir die relatiewe dosis vergelykings tussen die MC en film data vir die antropomorfiese fantoom.

Acknowledgements

This research project was funded by the South African Medical Research Council (MRC) with funds from National Treasury under its Economic Competitiveness and Support Package.

"Trust in the LORD with all your heart and lean not on your own understanding" – Prov 3:5

There are not enough words to express my appreciation and gratitude towards my study leader Dr. F.C.P du Plessis for his devotion and support throughout this study. His endless knowledge and passion is a true inspiration.

I would like to thank my colleagues and Head of Department, Prof. W.I.D Rae, for their support and valuable advice.

The Department of Oncology for the use of their equipment and approving this study.

My wonderful husband for his unconditional love, support and words of encouragement.

My unborn daughter for reminding her mommy that she has to finish ☺

To all my family and friends for your endless encouragement and support.

Thank you to one and all who, directly or indirectly, have lent their helping in this venture.